Application of Predictive Modelling to the Lower Cretaceous Sedimentary Sequences of the Central Scotian Basin

By
Christopher Sangster

A Thesis Submitted to
Saint Mary's University, Halifax, Nova Scotia
in Partial Fulfillment of the Requirements for
the Degree of Masters of Science in Applied Science.

September, 2019 Halifax, Nova Scotia

Approved:	Dr. Georgia Pe-Piper Supervisor
Approved:	Dr. Francky Saint-Ange Beicip-Franlab
Approved:	Dr. David J.W. Piper Geological Survey of Canada
Approved:	Dr. Nicolas Hawie Beicip-Franlab
Approved:	Dr. Andrew MacRae Professor

Date: September 3rd 2019

Application of Predictive Modelling to the Lower Cretaceous Sedimentary Sequences of the Central Scotian Basin

by Christopher Sangster

Abstract

Forward stratigraphic modelling of the central Scotian Basin is used to evaluate proposed provenance pathways in the Early Cretaceous and exploration risk. Modelling results confirm proposed pathways, supporting the diversion of the Sable and Banquereau rivers during the formation of the Naskapi Member, as well as likely episodic diversions during the Albian. Stratigraphic modelling techniques and petrographic studies predict the distribution of potential reservoir intervals and the influence of diagenesis on detrital minerals. Sand is dominantly trapped on the shelf in all units, with preferential accumulation in salt minibasins along the slope and shallow basin, and bypass to the deep basin. Simulation of feldspar grains and the presence of faulting and high permeability lithofacies suggest a zone of low risk to exploration on the shelf of the western and central Scotian Basin, and one of moderate risk in the eastern Scotian Basin.

September 3rd 2019

Table of contents

List of figures

List of tables

Appendices

Acknowledgements

This project is the result of a collaboration between Beicip-Franlab and Saint Mary's University, and would not have been possible without the funding provided by the Nova Scotia Offshore Energy Research Association to GPP, NSERC through a Discovery Grant to GPP, Beicip-Franlab, and Saint Mary's University.

I would like to thank Alcide Thebault and the support team at Beicip-Franlab for their help with the OpenFlow suite. I would also like to thank the CNSOPB, particularly Mark Deptuck and Kris Kendell, Adam MacDonald at the NS Department of Energy, and Andrew MacRae for their additional technical advice. I would also like to thank Dr Xiang Yang for his help with SEM analysis and the CNSOPB for providing the samples analyzed as part of this study.

Finally, I would like to thank all of my supervisors and committee members, my fellow graduate student in the office, and my family for all their help and support over these last few years. This work would not have been possible without the

List of abbreviations and acronyms

BSE – Back scattered electron (image)

CNSOPB – Canada-Nova Scotia offshore petroleum board

CRS – Common risk segment (map)

EDS – Energy dispersive spectroscopy

IFP – Institut français du pétrole (French institute of petroleum)

MFS – Maximum flooding surface

NIH – National institutes of health

OETR – Offshore energy technical research association

OERA – Offshore energy research association

RSM – Response surface mapping

RT – Rotary table

SEM – Scanning electron microscope

SS – Structural style (after Albertz et al., 2010)

TD – Total depth

Mineral abbreviations after Whitney and Evans (2010).

Chapter 1: Introduction

The offshore of Nova Scotia has been the site of several producing oil and gas fields and continues to be an area of active oil and gas exploration (OETR, 2011). There is particular interest in the Lower Cretaceous sandstones of the Missisauga and Logan Canyon formations, in which several oil and gas reservoirs have been developed. While this area has been the subject of much research and exploration, the distribution and quality of reservoir sandstone units is poorly understood, particularly in the deep basin, where only few wells have been drilled. Exploration is further complicated by widespread salt tectonism (Kendell, 2012) and the strong influence of diagenesis on reservoir quality (Zhang et al., 2015). Porosity and permeability are important factors in determining reservoir quality, however, these properties are susceptible to alteration as a result of both diagenesis and compaction during burial. It is therefore important to understand the factors which promote high reservoir quality. This study aims to produce predictive stratigraphic models of both sand distribution and reservoir quality in the central Scotian Basin (Fig. 1.1).

“Source to sink” studies (Meade, 1972, 1982; Allen, 2008; Sømme et al., 2009a, 2009b; Martinsen et al., 2010; Macgregor, 2012) and numerical modelling software (Hawie et al., 2017) have been used to better assess the evolution of sedimentary basins and predict the location of sandstone reservoirs in other regions. Such studies integrate sedimentological and geophysical research with forward stratigraphic modelling techniques to generate predictive facies models of complex depositional settings.

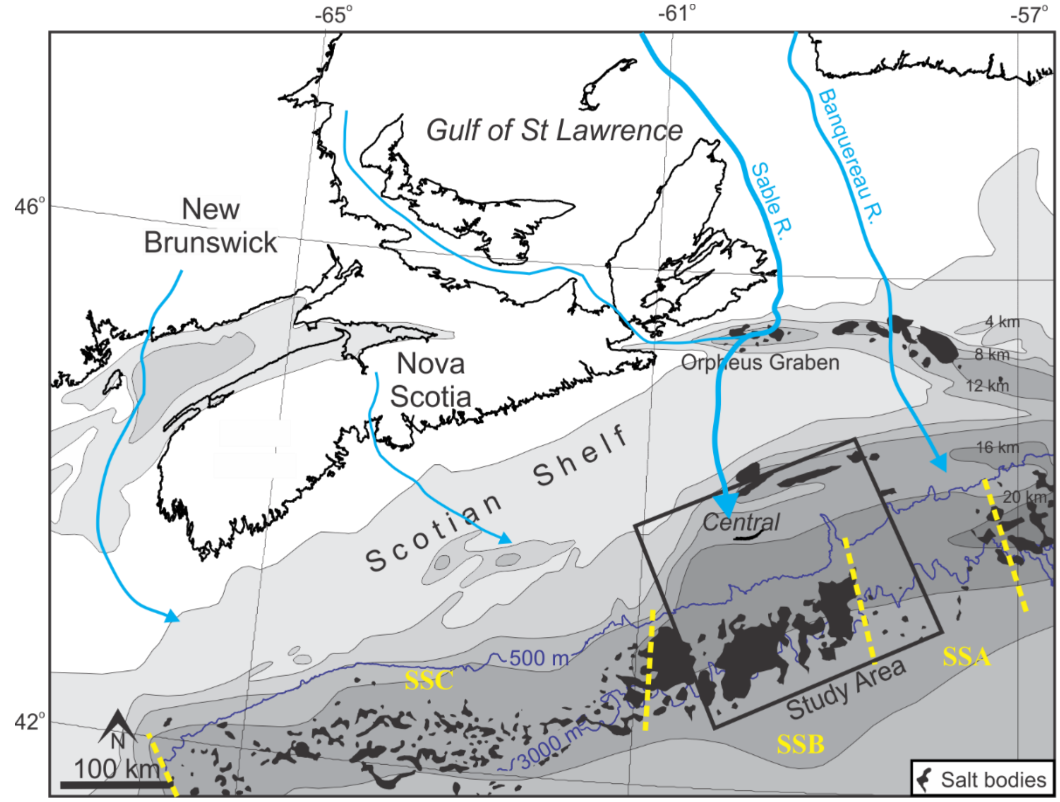

Figure 1.1: Map of study area. Grey tones show basin isopachs (in km: Wade and MacLean, 1990). Present 500 m and 3000 m isobaths are shown. Salt tectonic structural styles (SSA, SSB, and SSC) after Albertz et al. (2010). Salt bodies are after Shimeld et al. (2004).

The factors which influence reservoir quality have been investigated in numerous studies (Walker, 1984; Haszeldine et al., 1999; Chuhan et al., 2001; Gonzales-Acebron et al., 2010; Taylor et al., 2010; Yuan et al., 2015), with authors often attributing the presence of high-quality reservoirs which deviate from predicted porosity-depth trends to limited compaction, limited cementation, or the presence of preserved secondary porosity (Taylor et al., 2010). A variety of minerals have been shown to breakdown during diagenesis, including garnet (Morad et al., 2010), carbonates, and alkali feldspars (Haszeldine et al., 1999) resulting in the formation of secondary porosity.

K-feldspar has a high potential for producing secondary porosity as it is a common detrital mineral in many sandstones and therefore can contribute greatly to porosity enhancement with burial and interaction with basinal fluids. The proportion of K-feldspar in sediments is linked to sediment provenance (Tyrrell et al., 2014), and variations in K-feldspar concentrations during deposition are the result of variations in the rivers from which the sediments were derived. Thus, if the provenance of a region is sufficiently well understood, and the relation between K-feldspar composition and the provenance sources is re-created, numerical modelling software may be able to predict the initial distribution of K-feldspar within the basin. This distribution can then be compared to regional maps of thickness, temperature, and structure to determine the risk of K-feldspar dissolution and the preservation of the resulting secondary porosity.

The Lower Cretaceous delta system of the Scotian Basin is well suited for source to sink studies and provides an opportunity to apply forward stratigraphic modelling to a region experiencing active salt tectonism and diagenetic overprinting. Sedimentary facies and sediment provenance in this basin are reasonably well understood (Cummings and Arnott, 2005; Cummings et al., 2006; Pe-Piper et al., 2008; Gould et al., 2010; Tyrrell et al., 2014; Zhang et al., 2014). Additionally, diagenetic processes (Gould et al., 2010; Karim et al., 2012; Okwese et al., 2012; Pe-Piper et al., 2017), and their influence on K-feldspar occurrence (Pe-Piper and Yang, 2014) have been studied extensively.

The study area is a 185 km x 215 km region in the central Scotian Basin (Fig. 1.1). This area has the highest density of wells in the Scotian Basin, and covers a range of salt-tectonic domains (Kendell, 2012). This study focuses on the Lower Cretaceous reservoir sandstone units from the base of the Barremian (130 Ma) to the Late Albian (101 Ma) (Weston et al., 2012). This age span, which includes the Upper Missisauga Formation and the Naskapi and Cree Members of the Logan Canyon Formation (Wade and MacLean, 1990; Fig. 1.2), is the interval of most producing reservoirs in which basin-scale correlation of seismic markers is possible.

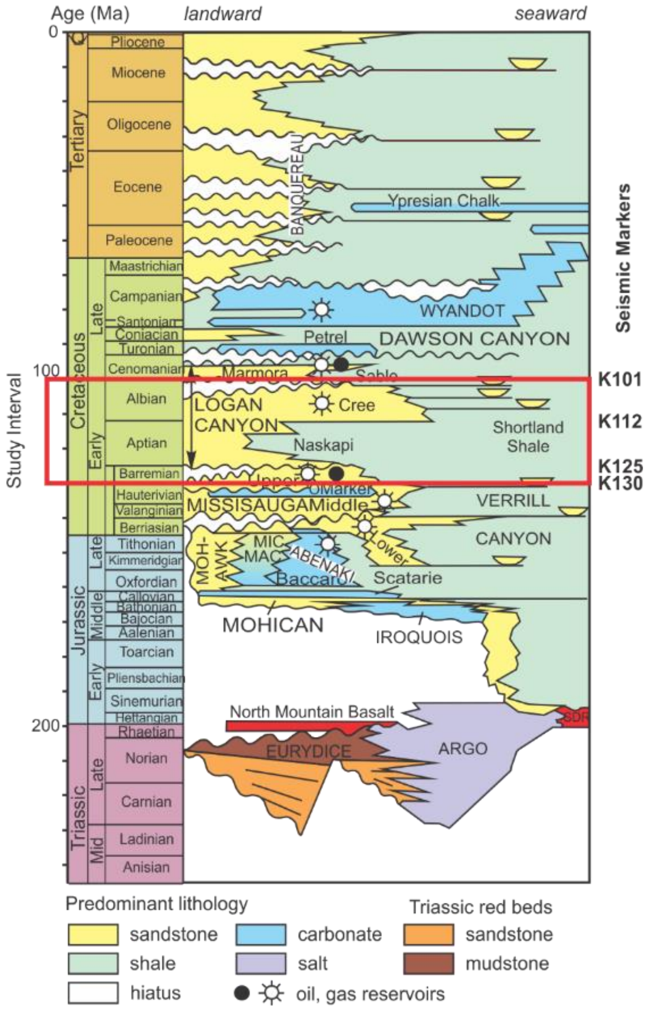

Figure 1.2: Stratigraphic column for the central Scotian Basin (Weston et al., 2012) showing the study interval. Seismic markers after OETR (2011).

This study uses DionisosFlow ^{TM} software, a dynamic-slope model (i.e. diffusion based model) which uses empirical transport laws (Granjeon and Joseph, 1999) to simulate sediment deposition. Input parameters are derived from an integrated multi-disciplinary approach to stratigraphic modelling, in which relevant research conducted in the study area is used to determine system inputs. Information regarding the catchment areas (size and relief), sediment properties (grain size and density), and basin properties (bathymetry) during the study time are of particular importance (Hawie et al., 2017).

The use of these properties allows for the creation of models which are predictive within a known degree of uncertainty, and can be used to better understand the evolution of sediment sources through time, the impact of changes in source composition, improve our knowledge of sediment transport pathways within the basin, and also predict the distribution of potential reservoir units in the study area. In order to determine the potential impact of diagenesis on secondary porosity, K-feldspar distribution is also simulated in order to predict regions which have a high potential to produce secondary porosity. K-feldspar inputs are based on a petrographic study of the central Scotian Basin with particular emphasis on changes in K-feldspar proportion with depth, and with sediment sources.

Finally, this project aims to test the following questions using a combination of modelling and petrographic analysis; **1)** are provenance pathways based on sandstone petrology (Zhang et al., 2014) validated by observed sediment distribution and sediment supply; **2)** what proportion of sands were trapped on the slope or bypassed to the deep ocean floor; **3)** what external factors (e.g. climate, salt tectonics, changing sediment supply from river catchments) control the distribution of sands within the study area; **4)** is there spatial variation of feldspar abundance within the Scotian Basin; **5)** to what extent is the Scotian Basin influenced by the dissolution of feldspars; and **6)** can feldspar distribution be modelled and used to predict reservoir quality?

This thesis is centred around two journal articles which are presented in chapters 4 and 5. Questions related to provenance pathways, sand transport, and the generation of reference case models are discussed in chapter 4, and those related to reservoir quality and feldspar distribution are discussed in chapter 5. Material discussed as part of chapters 2 and 3 are summaries of the relevant geological histories and methods of these two papers and are also discussed in each of the two articles.

Chapter 2: Geological setting

The Scotian Basin is located offshore Nova Scotia (Fig. 1.1) and initially formed during the breakup of Pangaea in Mid-Triassic time (Wade and MacLean, 1990). It is a collection of depocentres which have accommodated sediments through the Mesozoic–Cenozoic, over which time more than 12 km (to a maximum of 18 km) of sediments were deposited (Wade and MacLean, 1990). These depocentres host the Upper Jurassic to Lower Cretaceous Missisauga and Logan Canyon formations (Fig. 1.2), which are important oil and gas reservoirs in the Scotian Basin (Wade and MacLean, 1990). The thick siliciclastic sediments of the Missisauga and Logan Canyon formations were accommodated by major listric growth faulting associated with salt withdrawal as early as the Late Jurassic (Kendell, 2012). Withdrawal occurred as the salt-rich evaporite successions of the Argo Formation, which accumulated in the Upper Triassic-Lower Jurassic rift basin, were overlain mainly by Middle Jurassic limestones and Upper Jurassic clastic sediments, deforming and mobilizing the underlying Argo salt (Kendell, 2012).

The Scotian Basin has been divided into several salt structural provinces on the basis of the style of salt deformation. Shimeld (2004) proposed five tectono-stratigraphic salt sub-provinces, which were later reclassified by Albertz et al. (2010) into three principal structural styles (SS) (Fig. 1.1). The region of interest of this study is dominantly a linked salt tectonic system (SSB), with an open-ended roho system and synkinematic sediment wedge (SSA) forming the extreme easterly part of the study area (Albertz et al., 2010; Fig. 1.1).

Kendell (2012) provided the following synthesis of the evolution of salt tectonics in the central Scotian Basin. The incursion of clastic and carbonate sediments into the central Scotian Basin during the Early Jurassic mobilized salt of the Argo Formation, generating abundant salt diapirs which combined to form the Sable Shelf Canopy by the Middle Jurassic. After its formation, this canopy began to expel salt basinward, culminating in the Early Cretaceous, as a result of continuing sediment loading by prograding delta systems in the region. In the eastern portion of the study area (SSA), expulsion rollovers resulted in the break-out of salt to the sea floor forming salt tongues. Sediment loading of the expelled salt in the western portion of the basin, and the formation of salt tongues in the eastern portion formed minibasins along what is now the Scotian Slope. In the central basin, salt displacement was dominantly vertical during the Jurassic and Early Cretaceous; however, by the mid Cretaceous displacement had become dominantly horizontal.

Salt migration from the shelf resulted in the formation of diapirs and salt stocks along the slope, eventually forming the Sable Slope Canopy by the Late Cretaceous. Roho-style salt-based detachment faults expelled salt laterally from the slope canopies into the deep basin, where it merged with previously expelled salt stock canopies (Albertz et al., 2010; Kendell, 2012).

The Missisauga Formation was deposited during the expulsion of the Sable Shelf Canopy, and is composed predominantly of sandstones. It formed between the Kimmeridgian and Barremian, with the Upper member of Late Hauterivian to Barremian age. The Missisauga Formation is overlain by the Logan Canyon Formation, the lower part of which is composed of the shale-rich mainly Aptian Naskapi Member and the sand-rich Albian Cree Member (Wade and MacLean, 1990). The upper Logan Canyon Formation is composed of the Cenomanian Sable Member and Marmora members, which are shale and sand dominated units respectively (Wade and MacLean, 1990).

Provenance studies based on detrital mineral chronology (of zircon, monazite, and muscovite), chemical “fingerprinting” of detrital heavy minerals, and bulk rock geochemistry suggest that during the Kimmeridgian–Cenomanian interval, three main river systems supplied sediment to the Scotian Basin: local rivers from the Meguma Terrane, the Sable River, and the Banquereau River (Zhang et al., 2014) (Fig. 2.1). The Meguma Terrane, located in mainland Nova Scotia, supplied sediments through several small rivers to the western and central basin (Reynolds et al., 2012). The Sable River was a large drainage system extending from southern Labrador to the central Scotian Basin. The drainage basin included the late Paleoproterozoic Makkovik Province of central Labrador, the Mesoproterozoic Grenville Province of southern Labrador, eastern Quebec, the Long Range inlier of western Newfoundland, the Palaeozoic crystalline basement of the Appalachian orogen, and the polycyclic sediments from the Carboniferous Maritimes Basin (Tsikouras et al., 2011; Pe-Piper and Piper, 2012; Piper et al., 2012). The Banquereau River supplied sediment dominantly to the eastern basin and was sourced through the Humber Valley in western Newfoundland from terrains found in central Newfoundland (Tsikouras et al., 2011) with minor sediments sourced from the Grenville and Makkovik provinces in the Labrador Rift (Pe-Piper et al., 2014).

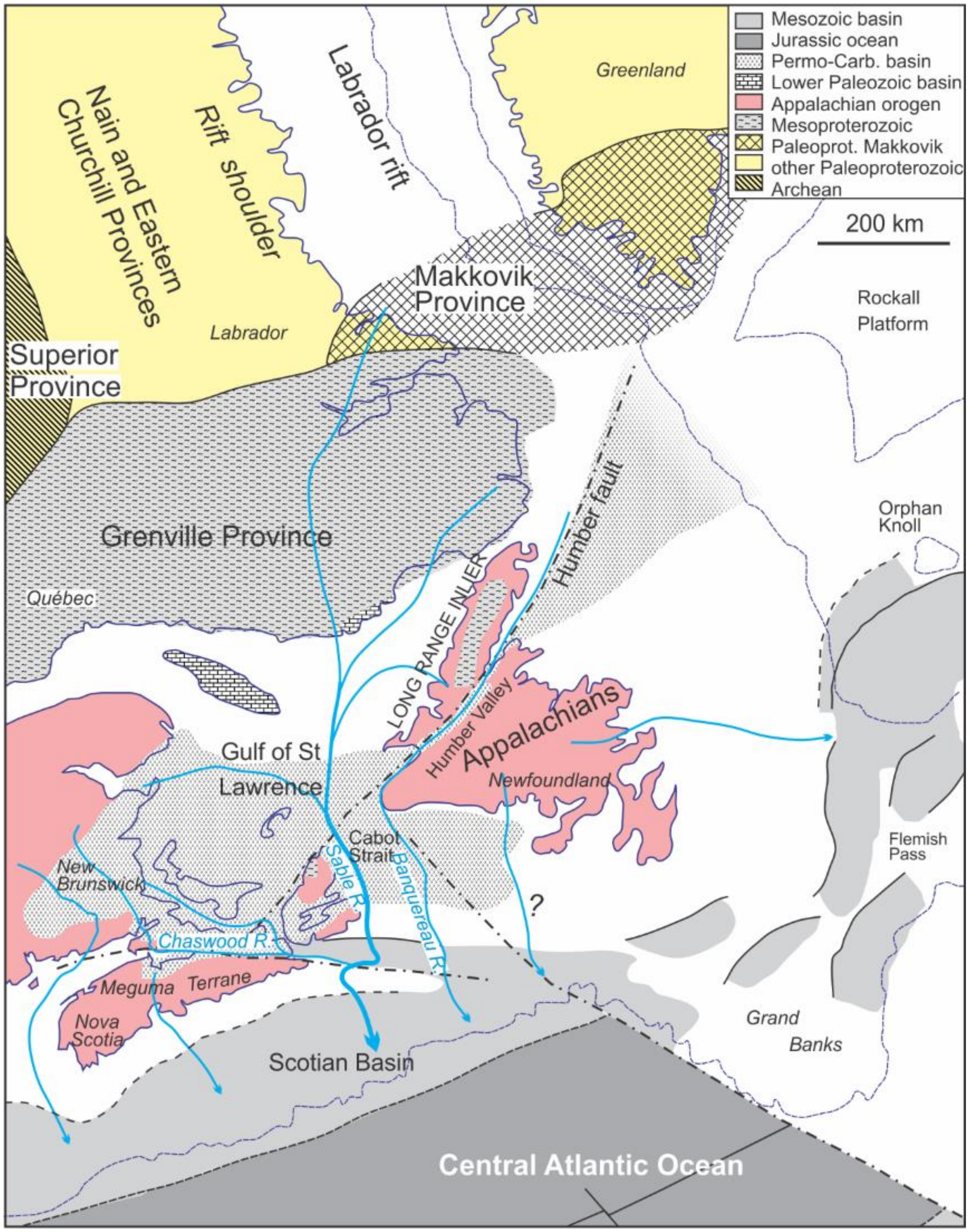

Figure 2.1: Early Cretaceous paleogeography of the hinterland of the Scotian Basin, showing courses of major rivers supplying sediment to the Missisauga and Logan Canyon formations inferred from provenance data by Zhang et al. (2014).

Over time, the catchment areas of these three main sources evolved, thought to be caused by periods of increased and decreased uplift (Zhang et al., 2014). As a result, the three river systems supplying the Scotian Basin were active at different times during the Early Cretaceous. The Middle and Upper Mississauga formations in the central Scotian Basin received sediments from the Sable River, the Banquereau River, and from small rivers draining the Meguma Terrain (Tsikouras et al., 2011; Piper et al., 2012; Reynolds et al., 2012; Pe-Piper et al., 2014; Zhang et al., 2014). However, there was a shift in sedimentation style during the Aptian, when the Naskapi Member was deposited. This shale prone unit was originally interpreted as the result of high eustatic sea-level during the Aptian, trapping sediments inboard from the Scotian Basin (Jansa and Wade, 1975), but recent studies concluded that its formation was largely the result of changes in sediment supply due to a tectonic diversion of the Sable and Banquereau rivers (Piper et al., 2011; Bowman et al., 2012; Chavez et al., 2018). Uplift and tilting of the Meguma Terrain (Reynolds et al., 2012), coupled with the extrusion of basalt into the flow path of the Sable and Banquereau rivers (Bowman et al., 2012), diverted these major rivers, resulting in the deposition of the shale-prone Naskapi Member throughout the Aptian. The Naskapi Member was sourced dominantly by the Meguma Terrane at this time, with additional contribution from reworked Upper Missisauga Formation sediments (Chavez et al., 2018), as the increased uplift would have continued to contribute sediments to the offshore. Sand-rich sedimentation returned during the Albian. During this time the uplift of the Meguma Terrane had slowed (Reynolds et al., 2012) and the Sable and Banquereau rivers eroded through the Aptian basalt flows (Bowman et al., 2012). These sand-rich sediments comprise the Cree Member of the Logan Canyon Formation, and share similar composition and geochemistry with the Upper Missisauga Formation (Piper et al., 2012; Reynolds et al., 2012; Pe-Piper et al., 2014; Zhang et al., 2014), suggesting a return to the pre-Naskapi Member sedimentation conditions.

The Scotian Basin shows a range in diagenetic processes that vary with depth. Shallow sea-floor diagenetic processes resulted in the formation of Fe-rich clays, siderite, phosphate, and early carbonate cements (Okwese et al., 2012). The Fe-rich clays re-crystalized as bertherine rims on quartz grains in thick delta-front sandstone beds (Gould et al., 2010). These bertherine rims later converted to chlorite, inhibiting the formation of silica cements and preserving porosity (Gould et al., 2010). Sea-level lowstands produced kaolinite cements as a result of fluxes of meteoric water. With increasing depth of burial, formation waters precipitated quartz overgrowths followed by Fe-calcite and ankerite cements (Karim et al., 2012).

K-feldspar diagenesis has been shown to occur in the Scotian Basin below approximately 1.9 km, initially with the formation of authigenic K-feldspar and albite following fractures and planes of weakness in K-feldspar grains (Pe-Piper & Yang, 2014). With increasing depth, detrital grains of K-feldspar are dissolved or replaced by ferroan-calcite and ankerite, with grains ultimately disappearing between 3.8 km and 4.5 km. Dissolution has been interpreted to be controlled by burial depth, and appears to be most significant in permeable sandstone units. Additional secondary porosity has been shown to form as a result of fracturing of quartz and carbonate cements (Karim et al., 2012). During late stage diagenesis, this secondary porosity has been filled by illite, chlorite, kaolinite, siderite, barite, and sphalerite (Pe-Piper et al., 2015). Additionally, occurrences of late diagenetic zircon have been observed in the basin (Pe-Piper et al., 2017).

The high-temperature diagenetic mineral assemblages present in the Scotian Basin are related to a widespread Aptian-Albian thermal event (Bowman et al., 2012). This event is recorded by volcanism in the Orpheus Graben, enhanced heat flow in terrestrial basins, high entrapment temperatures in primary fluid inclusions in quartz overgrowths and carbonate cements (Karim et al., 2012), strongly negative $\delta^{13}C$ values in carbonate cements (Karim et al., 2012), apatite fission track results (Grist et al., 1992), and the presence of diagenetic zircon (Pe-Piper et al., 2017). Based on these factors, a paleogeothermal gradient of 50°C/km is interpreted (Pe-Piper et al., 2017). This increased thermal gradient is thought to have heated underlying authochthonous salt and continental basement rocks to temperatures greater than 400°C, which in turn heated circulating brines.

Previous research conducted on the impact of diagenesis on regional reservoir quality in the Scotian Basin by Zhang et al. (2015) concluded that local factors, such as depositional lithofacies and sequence stratigraphy, salt tectonics, secondary porosity, overpressure, and hydraulic fracturing around the top of overpressure, rather than regional factors, are the controlling influence on reservoir quality. Factors which increased secondary porosity are related to the circulation of hot and corrosive basinal fluids through thick permeable sandstones, further promoted by the presence of salt tectonics and the resulting faulting. However, pore throats associated with secondary porosity are commonly small, resulting in a minor contribution to permeability.

Chapter 3: Methods

3.1 Modelling methodology

In this study, stratigraphic modelling was conducted using DionisosFlow™ (IFP Energies nouvelles and BeicipFranlab, 2016a), a diffusion-based forward stratigraphic modelling software that simulates basin infill over geological time scales (Granjeon, 1996). Produced models are then analysed using CougarFlow™ (IFP Energies nouvelles and BeicipFranlab, 2016b) to assess the impact of various simulation parameters, and determine regions of increased sensitivity (Agrawal et al., 2015; Hawie et al., 2015). Models are calibrated against reference wells and seismic surfaces with the goal of reproducing the overall trends of sediment distribution in the basin.

3.1.1 Principles of forward stratigraphic modelling by DionisosFlow™

DionisosFlow™ is a deterministic 4D multi-lithology forward stratigraphic modelling software. It reconstructs geological processes in a sequence of time steps with the intention of quantifying the average geometries and facies of sedimentary units (Granjeon and Joseph, 1999), reproducing the net result of sediment supply, transport, and accommodation that results from uplift, subsidence, and sea level fluctuation. DionisosFlow™ simulates the transport of sediments within basins by combining empirical water- and gravity-driven diffusion equations based on hill slope creeping (linear slope-driven diffusion with transport proportional to gradient) and water discharge-driven transport (non-linear water and gradient driven diffusion equation). The resulting sediment transport equation is:

$$Q_s = -K_{s_i}/\nabla h - K_{w_i} Q_w^m S^n$$

Where: Q_s: sediment flux [km^2y^{-1}]
K_s: diffusion coefficient of hill slope creeping transport [km^2y^{-1}]
h: elevation (m)
K_w: diffusion coefficient of water discharge driven transport [km^2y^{-1}]
Q_w: dimensionless local water discharge cell (normalised by 100 $m^3/(s \cdot km)$)
S: local basin slope gradient
m and n: represent constants between 1 and 2 (Tucker and Slingerland, 1994)
i: the transported lithology

In order to reproduce natural systems, DionisosFlow™ calculates sediment flow within the basin for two different scenarios: 1) low energy long term (LELT), which is the permanent flow determining the sediment transport from typical fluvial sources and oceanographic processes such as longshore drift, and 2) high energy short term (HEST), which handles sediment flow related to high energy events such as major fluvial floods and turbidites (Deville et al., 2015; Hawie et al., 2018), which may be responsible for transporting most sediment.

The average diffusion coefficient represents the ratio between sediment discharge and basin slope (Hawie et al., 2017): ((average sediment thickness x basin length (km)) / (time span (Ma) x basin slope (m/km)). The relationship between the diffusion coefficients for each sediment size class is such that smaller grain sizes have higher coefficients than larger grain sizes.

3.1.2 Principles of sensitivity analysis by CougarFlow™

CougarFlow™ is a statistical software used to evaluate the sensitivity of stratigraphic models generated using DionisosFlow™ (Hawie, 2015). It uses Response Surface Modelling (RSM), in which multiple models are run. Within these models, uncertain parameters are varied, and the response of the models to these variations generate the response surface (Lacroix and Albadi, 2012). The goal of RSM is to approximate the complex interaction between uncertain parameters and simulation results. This study employs Latin Hypercube sampling RSM. This RSM approach performs simulations with randomly chosen values for the uncertain parameters selected between a predefined maximum and minimum to predict the response of the model to all other values of the uncertain parameters (Delaplace et al., 2013). This approach requires a large number of simulations to be run in order to accurately predict the response. To check the accuracy of the produced RSM, a small number of confirmation runs are performed, and their results compared to the RSM of Lacroix and Aldabi (2012). Monte-Carlo sampling can then be applied to the RSM to make predictions, and generate a probabilistic distribution of the response of the models (Lacroix and Albadi, 2012).

A script is used to generate and export maps of the properties of interest, in this case the distribution of sands. The contents of these maps are then compared to the reference case models to determine the degree to which altering parameters has influenced overall distribution. The maps produced for each simulation in the sensitivity analysis are then compared to one another to produce a map of standard deviation, which can be used to identify sensitive areas.

3.1.3 Modelling and calibration strategy

Two types of models have been produced for this study, the first of which are “reference case models”. Such models are calibrated in terms of thickness and lithofacies against well and seismic data. These reference case models are used to predict sand distribution and infer information regarding the evolution of the catchment areas for the study area. The second type of models are feldspar distribution models which are used to predict the distribution of K-feldspar grains in the study area, and predict where diagenesis may play a role in producing secondary porosity.

3.1.3.1 Reference case models

Three separate models were produced to simulate the main units the: Upper Missisauga Formation (130–125 Ma), Naskapi Member (125–112 Ma), and Cree Member (112–101 Ma). Ages are after Gradstein et al. (2005) to align with research conducted as part of the Play Fairway Analysis (OERA, 2016) from which seismic surfaces and previous modelling have been conducted. These units are bounded by the seismic markers K130, K125, K112, and K101 (Fig. 1.2), with the K125 and K112 surfaces calculated as part of this study. The K130 horizon has been picked at a regional maximum flooding surface (MFS) which occurred at 130 Ma (OETR, 2011) known as the Hauterivian MFS, and is approximately equivalent to the “O-marker” which marks the base of the Upper Missisauga Formation on the shelf (Wade and MacLean, 1990). As such, the Upper Missisauga Formation has been assumed to begin at 130 Ma for this study. The K101 marker is picked at the Late Albian Unconformity marking the transition of the Cree Member to the overlying Sable Member (OETR, 2011). The models use a 5 x 5 km grid size and 0.25 Ma time steps with a 185 x 215 km area.

The models were calibrated by altering the sediment supply, water discharge, and sediment grain size proportions of the various sources inferred for each unit, as well as modifying the subsidence to allow for the appropriate sediment accommodation space.

The calibration goal is to attain a minimum 80% calibration in basin thickness, individual well thickness in each calibration well based on lithostratigraphic picks for the Upper Missisauga Formation, Naskapi Member, and Cree Member (Table 3.1), and reference well lithofacies. This process generates three reference case models, which can be used to make comparisons to the existing geological interpretation of the area, and answer questions regarding the evolution of the basin.

This study simulates only clastic sedimentation, although thin carbonate beds are present in several wells. These carbonates are typically bioclastic, part of transgressive condensed units on the shelf (Gould et al., 2012), and pass laterally into condensed sandstones (Cummings et al., 2006). Given the coarse-grained nature of these carbonates, and their facies associations, carbonate beds in this study have been considered to be equivalent to sand-rich sediments during calibration.

Table 3.1: Stratigraphic unit depths from reference and sample wells in the study area.

Well	Well pick (m)					
	Top Marmora Member	Top Sable Member	Top Cree Member	Top Naskapi Member	Top Upper Missisauga Formation	Base Upper Missisauga Formation/TD
Alma F-67*	-	-	1908[1]	2543.6[2]	2843.6[2]	3730[1]
Alma K-85	-	-	1877[2]	2525.3[2]	2843.1[2]	3602[2]
Annapolis G-24*	-	-	3852[1]	4332[2]	5041[2]	5285[1]
Banquereau C-21*	-	-	2389[2]	3384[3]	3575.5[2]	4175[1]
Chebucto K-90*	-	-	2640[1]	3512[4]	3689[2]	4853[1]
Chippewa G-67	-	-	1664.2[2]	2307.5[2]	2383.2[2]	2545.1[2]
Cohasset D-42	-	-	1634.3[2]	2122.9[2]	2247.39[2]	2435.4[2]
Cohasset L-97*	-	-	1550[2]	2109[2]	2220[2]	2409[2]
Crimson F-81*	-	-	3990[1]	4554[2]	4772[2]	5928[1]
Glenelg E-58	-	-	2248.1[2]	3102.8[2]	3364.3[2]	4093[2]
Glenelg E-58A	-	-	2245[5]	3106[5]	3356[5]	4104[5]
Glenelg J-48*	-	-	2301.5[1]	3273[4]	3488[2]	4061[1]
Kegeshook G-67	-	-	1446.5[2]	1948[2]	2035.4[2]	2228[2]
Missisauga H-54	-	-	1646.5[2]	2313.9[2]	2414.5[2]	2712.1[2]
North Banquereau I-93	-	-	2262[2]	3260[4]	3460.2[4]	3785[2]
North Triumph G-43	-	-	2524[2]	3580.1[4]	3892.9[4]	4504[2]
Onondoga B-96	-	-	1975.74[5]	2468.91[5]	2647.22[5]	3191.6[5]
Peskowesk A-99	-	-	1675.8[2]	2378[2]	2465[2]	2754.3[2]
Sable Island 2H-58	1528.29[5]	1845.28[5]	1963.55[5]	2615.83[5]	2707.57[5]	2758.44[5]
Sable Island 5H-58	-	-	1802[5]	2464.64[5]	-	2478.05[5]
Sauk A-57	-	-	2067.5[2]	2880.7[2]	3020.3[2]	3247.3[2]
Tantallon M-41*	-	-	3704[1]	4273.7[2]	4400[2]	4738[1]
Thebaud I-93*	-	-	1746[1]	2541.5[2]	2653.2[2]	3311[1]
Venture B-52*	-	-	2100[1]	2849[2]	2970[2]	3564[1]
Venture D-23	-	-	2024[2]	2826.1[2]	2953.1[2]	3344[2]

[1] OERA (2016), [2] OETR (2012), [3] Correlation to well picks for the North Banquereau I-13 well in Chavez et al. (2018), [4] Chavez et al. (2018), and [5] MacLean and Wade (1993). Reference wells are indicated by*

Salt tectonics played a major role in the evolution of the Scotian Basin during the Early Cretaceous, but the detailed evolution of salt bodies through time is poorly constrained. In order to incorporate the influence of salt tectonics on the basin, only the vertical movement of the salt bodies was considered, using subsidence variations to recreate sediment distribution patterns. A seismic thickness map of the K130–K101 interval (OETR, 2011) defines overall thickness.

This thickness is then distributed through time based on average thickness of sediments in wells for each unit (Tables 3.1 & 3.2) to simulate salt movement. Models are simulated assuming zero sediment porosity for all lithologies and therefore maximum sediment compaction is simulated, so that calculated sediment supply may be overestimated. Unit thickness calibration is measured using thickness error maps generated from comparing simulated thickness with thickness derived from seismic data (Table 3.2). In regions where the presence or mobilization of salt have resulted in a thickness of zero, the thickness is simulated by extrapolating the subsidence rate from the surrounding area, particularly on the edges of the study area. In the basin, areas with no interpreted surface or zero thickness were treated as salt, and were given low subsidence rates to simulate expulsion.

Table 3.2: Mean thickness and percent thickness of the Upper Missisauga Formation, Naskapi Member, and Cree Member based on reference well picks, excluding the Annapolis G-24 well.

Unit	Average thickness (m)	Percent thickness (%)
Cree Member	745.7	48.5
Naskapi Member	174.8	11
Upper Missisauga Formation	684	40.5

A calibration indicator script is used to determine the percent calibration of the simulated model to well logs from ten reference wells (Fig. 3.1). It compares simulated results of thickness and lithofacies (texture) within the 5 by 5 km cell in which each calibration well is located, to the thickness and lithofacies of the well logs. Given the large difference in horizontal resolution between the cell size of the model and the size of the reference wells, changes in lithology which may be the result of facies changes on a much finer scale than the grid size present a difficult challenge in calibration. The focus of model calibrations is therefore to account for the overall distribution of sediments within the study area.

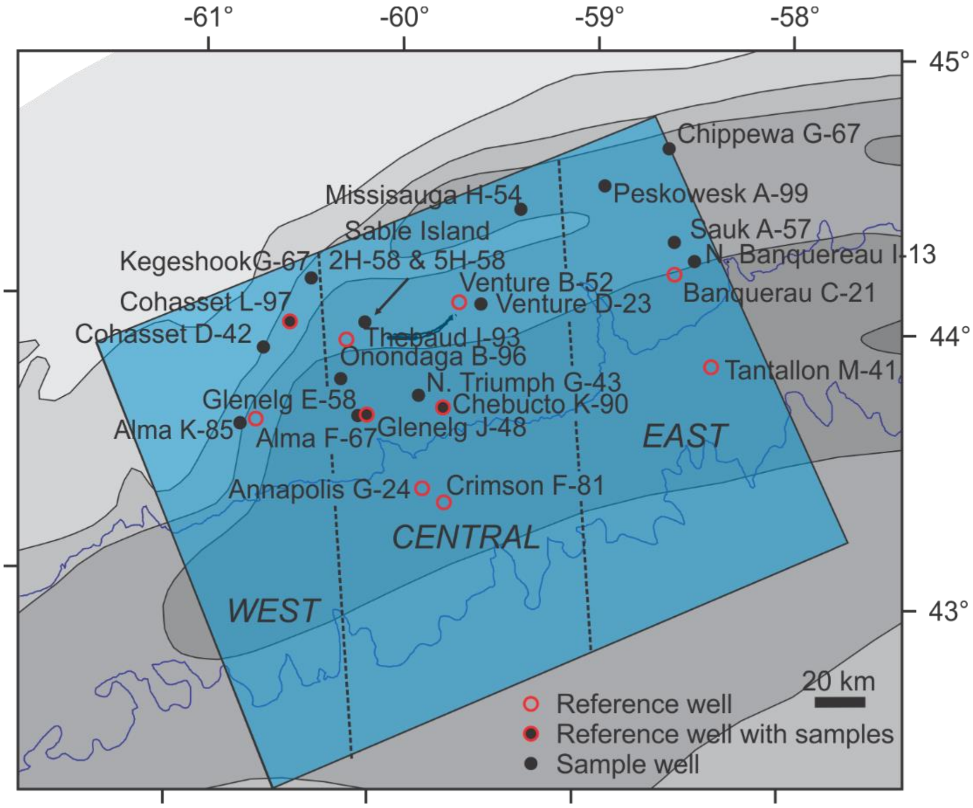

Figure 3.1: Map of study area with reference wells and wells sampled for feldspar content. Grey tones show basin isopachs (in km: Wade and MacLean, 1990). Present 500 m and 3000 m isobaths are shown.

Lithofacies calibration compares simulated facies to lithofacies at the control wells on the basis of their similarity (Appendix 1-1). Lithofacies of the same class result in 100% calibration, with calibration decreasing with greater difference between facies, such that sandstone vs. siltstone returns a greater calibration than sandstone vs. shale. As the lithofacies logs for the reference wells are at a much higher resolution than the simulated logs, it is necessary to upscale the well logs. This is achieved by averaging the lithofacies of the well logs within segments which correspond to the average thicknesses of the time steps generated during simulation.

Reference case wells have been classified into lithofacies (e.g. sandstone, shale, sandy shale), based largely on petrophysical interpretations, which have been calibrated against cuttings data. The quantitative proportions of individual grain sizes (e.g. sandstone vs. mudstone) in each lithofacies are not determined. However, simulated models require ranges of sediment proportions to assign lithofacies to simulated well logs. The numerical cut offs for these simulated lithofacies have been chosen to most closely match the observed lithofacies in wells (Table 3.3). Sediment concentrations in the reference case models are therefore qualitative rather than quantitative in nature.

Table 3.3: Definitions for simulated lithofacies based on simulated sediment proportions.

Lithofacies	Sand (%)	Silt (%)	Shale (%)
Sandstone	>30	<18	
Silty Sandstone	20-30	16-30	
Shaly Sandstone	20-30	<18	
Shale	<16	<16	>50
Sandy Shale	16-20	<18	
Silty Shale	<30	16-30	
Siltstone	<30	>30	
Sandy Siltstone	16-30	>18	
Shaly Siltstone	<35	>18	

To determine the well thickness calibration, the difference between the simulated and actual well thickness is divided by the actual thickness from the well log. It is calibrated by altering the subsidence around individual wells to provide sufficient accommodation space to ensure that each unit is calibrated against sediments from only that unit.

3.1.3.2 Feldspar distribution model

Feldspar distribution models are generated using the reference case models produced following the above methodology. K-feldspar is added to these models as equivalent sediment fractions (e.g. coarse sand sized K-feldspar grains, medium sand sized K-feldspar grains, etc.). The properties of these sediment classes, such as grain size and sediment proportion, are based on the results of the analyses detailed below.

3.2 Feldspar analysis

3.2.1 Sample collection

In order to determine the concentration of feldspar throughout the study area and through time, 48 samples have been analyzed from a total of 15 wells throughout the basin (Fig. 3.1). Samples were taken from sand-rich intervals in the Early Cretaceous. Of these samples 15 are taken from the Upper Missisauga Formation, 5 from the Naskapi Member, 27 from the Cree Member, and a single sample was taken from the Marmora Member (Table 3.4; Fig. 3.2). The central Scotian Basin is represented by 21 samples, with 13 samples taken from the eastern Scotian Basin, and the remaining 9 from the western Scotian Basin (Fig. 3.2).

All samples were obtained from the Canadian Nova Scotia Offshore Petroleum Board (CNSOPB). Initially sidewall cores were requested, as they provide compositional data for specific depths. However, due to sampling regulations, traditional sidewall core samples were unavailable and instead sidewall core rubble, which resulted from the breakdown of the fragile sidewall cores, was permitted for sampling. This rubble was sent to Vancouver Petrographics to produce 38 polished, smear slide thin-sections. Eight additional polished thin sections were analyzed from conventional core.

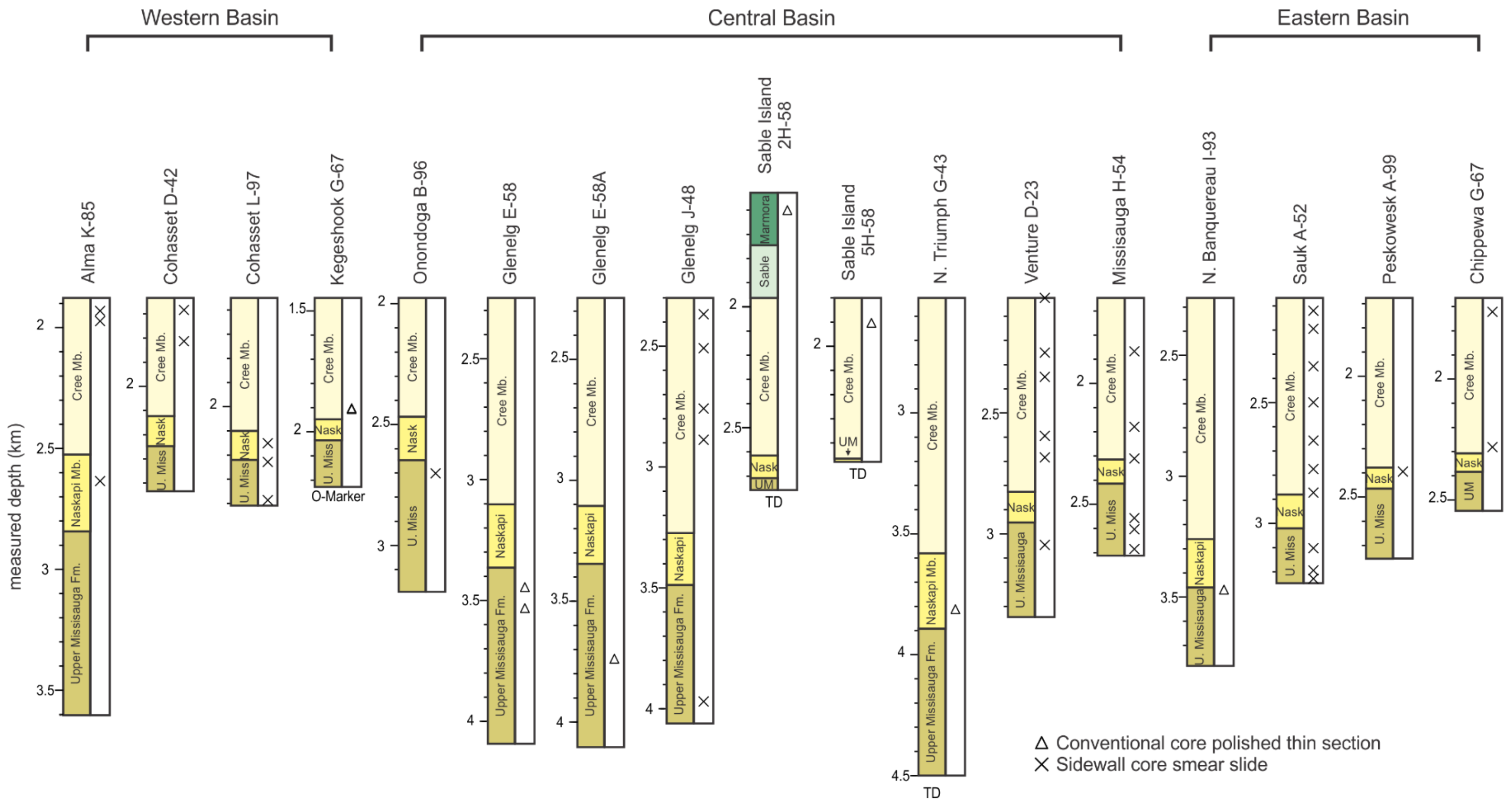

Figure 3.2: Summary of sample depths with well picks taken from table 3.1.

Table 3.4: Summary of analyzed samples showing the analytical technique applied to each sample.

Well	Well #	Type	Sample	Depth (m)	Appendix	EDS	EDS+X-ray map	X-ray map
Alma	K-85	S	1928	1928	3-1		√	
Alma	K-85	S	1971.9	1971.9	3-2		√	
Alma	K-85	S	2633	2633	3-3		√	
Chippewa	G-67	S	5639	1718.8	2-1	√		
Chippewa	G-67	S	7492	2283.6	2-2	√		
Cohasset	D-42	S	5525	1684.02	2-3	√		
Cohasset	D-42	S	5949	1813.26	2-4	√		
Cohasset	L-97	S	2150.1	2150.1	2-5	√		
Cohasset	L-97	S	2228.7	2228.7	2-6	√		
Cohasset	L-97	S	2386.9	2386.9	2-7	√		
Glenelg	E-58	P	E-58-9	3443.86	4-1			√
Glenelg	E-58	P	E-58-17	3532.08	4-2			√
Glenelg	E-58A	P	E-58A-10	3737.9	4-3			√
Glenelg	J-48	S	2365	2365	3-4		√	
Glenelg	J-48	S	2507	2507	3-5		√	
Glenelg	J-48	S	2758.5	2758.5	3-6		√	
Glenelg	J-48	S	2890	2890	3-7		√	
Glenelg	J-48	S	3970	3970	3-8		√	
Kegeshook	G-67	P	1902.3	1902.3	4-4			√
Kegeshook	G-67	P	1906.36	1906.36	4-5			√
Missisauga	H-54	S	6117	1864.46	2-8	√		
Missisauga	H-54	S	7160	2182.34	2-9	√		
Missisauga	H-54	S	7579	2310.07	2-10	√		
Missisauga	H-54	S	8390	2557.27	2-11	√		
Missisauga	H-54	S	8541	2603.29	2-12	√		
Missisauga	H-54	S	8823	2689.25	2-13	√		
North Banquereau	I-93	P	3469.27	3469.27	4-6			√
North Triumph	G-43	P	G-43-24	3811.53	4-7			√
Onondoga	B-96	S	8860	2700.53	3-9		√	
Peskowesk	A-99	S	2395	2395	2-14	√		
Sable Island	2H-58	P	1600.27	1600.27	2-15	√		
Sable Island	5H-58	P	1903.66	1903.66	2-16	√		
Sauk	A-57	S	6952	2118.97	3-10		√	
Sauk	A-57	S	7185	2189.99	3-11		√	
Sauk	A-57	S	7710	2350.01	3-12		√	
Sauk	A-57	S	8196	2498.14	3-13		√	
Sauk	A-57	S	8717	2656.94	3-14		√	
Sauk	A-57	S	9110	2776.73	3-15		√	
Sauk	A-57	S	9421	2871.52	3-16		√	
Sauk	A-57	S	10194	3107.13	3-17		√	
Sauk	A-57	S	10498	3199.79	3-18		√	
Sauk	A-57	S	10607	3233.01	3-19		√	
Venture	D-23	S	2026	2026	3-20		√	
Venture	D-23	S	2254	2254	3-21		√	
Venture	D-23	S	2357	2357	3-22		√	
Venture	D-23	S	2606	2606	3-23		√	
Venture	D-23	S	2690	2690	3-24		√	
Venture	D-23	S	3055	3055	3-25		√	

P = polished thinsection and S = smear slide.

3.2.2 SEM analysis

In order to determine the composition of these sandstones, point counting was conducted using back scattered electron (BSE) images from a scanning electron microscope (SEM). The rubbles contain a large variety of grain sizes as a result of their fragmentation. As a result, distinguishing between some mineral phases can be difficult using the optical microscope, but SEM analyses also allows for more precise chemical differentiation of minerals. An approach similar to that of Zhang et al. (2015) has been applied to point counting analysis, in which minerals are differentiated on the basis of chemical analysis and by using their gray-scale brightness, which is controlled by their mean atomic number on a scale from 0–255 (Tovey and Krinsley, 1992). The SEM analysis was completed in the Regional Analytical Centre at Saint Mary's University using a LEO 1450 VP SEM, acquiring the back scattered electron (BSE) images and electron-dispersive spectroscopy (EDS) chemical analyses of minerals. This SEM has a maximum resolution of 3.5 nm at 30 kV. It is equipped with an INCA X-max 80 mm^2 silicon-drift detector EDS system that has a detection limit >0.1%. A tungsten filament produces a 10 μm beam, and is calibrated with a cobalt standard. A minimum of 600 detrital mineral grains were analyzed in each sample. Samples have been analyzed using three techniques (Table 3.2; Fig. 3.3): **1)** SEM EDS analysis (Appendix 2); **2)** SEM EDS and X-ray mapping analysis (Appendix 3); and **3)** X-ray mapping analysis (Appendix 4). Mineral names have been abbreviated following Whitney and Evans (2010) in the following chapters and supporting appendices (Appendices 2-4).

3.2.2.1 SEM EDS based analysis

Large volumes of EDS analyses were taken from each site, with grains of varying brightness targeted to determine the range of minerals present (Fig. 3.3A). Additionally, to determine the presence of plagioclase grains, particularly albite, grains which displayed cleavage were targeted. The results of these analyses were then combined with the approach used by Zhang et al. (2015) to determine the proportion of minerals present in each site. This approach has been conducted on 14 samples.

3.2.2.2 SEM EDS and X-ray mapping based analysis

Low resolution X-ray maps have been produced for each site (Fig. 3.3B). Element maps of Si, Na, and K were then used to determine likely grains of quartz, plagioclase, and K-feldspar which were then confirmed using EDS analysis (Fig. 3.3A). 26 samples have been analyzed using this technique.

3.2.2.3 X-ray mapping based analysis

Seven samples have been analyzed using only X-ray maps and gray-scale brightness to determine mineral abundances (Fig. 3.3A&B). Si, Na, and K maps are used to determine the abundance of plagioclase and K-feldspar respectively, with mineral habit used to differentiate K-feldspar from other K rich minerals with similar brightness such as muscovite.

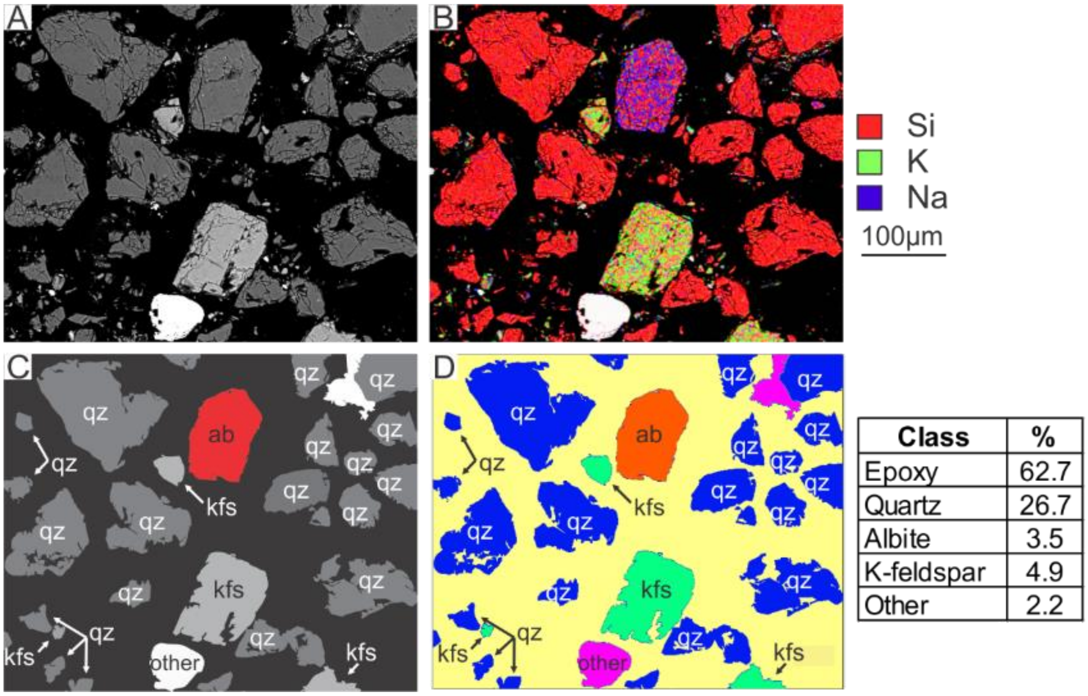

Class	%
Epoxy	62.7
Quartz	26.7
Albite	3.5
K-feldspar	4.9
Other	2.2

Figure 3.3: Representative images of modal abundance analysis showing: **A)** a BSE image of a site of interest; **B)** a quantitative X-ray map showing distribution of Si (red), K (green), and Na (blue); **C)** a traced BSE image with false colouring; and **D)** MultiSpec^{TM} output window with results.

3.2.3 Modal abundances

BSE images were processed using CorelDraw^{TM} (Corel, 2016) software. Images were traced using the PowerTrace^{TM} tool (Corel, 2016) (Fig. 3.3C) and mineral species of interest have been coloured for image analysis. Coloured minerals are those which could not be differentiated on the basis of their grey-scale brightness, such as albite and oligoclase from quartz, and K-feldspar when carbonates are present. The traced images have been analyzed using MultiSpec^{TM} (Purdue Research Foundation, 2016) to determine the area percentage of all grains in the images on the basis of their gray-scale brightness and colouring (Fig. 3.3D). Due to the reliance on smear slide samples of disaggregated sand in this study, it is difficult to determine if minerals are detrital or diagenetic. Detrital mineral assemblages in the Scotian Basin are dominated by quartz and feldspar species, therefore, the compositional data from these samples is represented as the normalized percentage of quartz, plagioclase, and K-feldspar.

3.2.4 Grain size measurements

Grain size was measured using ImageJ^{TM} (NIH, 2019) image processing software. Quartz and K-feldspar grains were measured manually from BSE images, with minimum of 300 total grains measured for each sample. A minimum grain size cut-off was based on the size of the finest quartz grain present (Table 5.2).

Chapter 4: Forward stratigraphic modelling of sediment pathways and depocentres in salt-influenced passive-margin basins: Lower Cretaceous, central Scotian Basin

Published paper with additional edits: Basin Research, 2019. DOI: 10.111/bre12342

4.1 Introduction

The offshore of Nova Scotia has been the site of several producing oil and gas fields and continues to be an area of active oil and gas exploration. There is particular interest in the Lower Cretaceous sandstones of the Missisauga and Logan Canyon formations, in which several oil and gas reservoirs have been developed (OETR, 2011). While this area has been the subject of much research and exploration, the distribution and quality of reservoir sandstone units is poorly understood, particularly in the deep basin, where few wells have been drilled. Exploration is further complicated by the widespread salt tectonism and the strong influence of diagenesis on reservoir quality. “Source to sink” studies (Meade, 1972, 1982; Allen, 2008; Sømme et al., 2009a, 2009b; Martinsen et al., 2010; Macgregor, 2012) and numerical modelling software (Hawie et al., 2017) have been used to better assess the evolution of sedimentary basins and predict the location of sandstone reservoirs in other regions. Such studies integrate sedimentological and geophysical research with forward stratigraphic modelling techniques to generate predictive facies models of complex depositional settings. However, due to the complications associated with modelling and seismic interpretation in salt basins, the majority of published modelling research has been conducted in regions without active salt tectonism (Gulf of Lion: Rabineau et al., 2005; Abu Dhabi: Agrawal et al., 2015; Levant Basin: Hawie et al., 2017), with simulations of sediment deposition in association with salt tectonics conducted using only 2D modelling (Prather 2000; Kubo et al., 2005).

The Early Cretaceous delta system of the Scotian Basin is well suited for source to sink studies and provides an opportunity to apply forward stratigraphic modelling to a region experiencing active salt tectonism at the time. Sedimentary facies and sediment provenance are well understood (Cummings and Arnott, 2005; Cummings et al., 2006; Pe-Piper et al., 2008; Gould et al., 2010; Zhang et al., 2014) and salt tectonics during the Early Cretaceous played a major role in the distribution of sediments on the shelf, slope, and basin. This study aims to answer questions related to the strong influence of salt tectonics in the Scotian Basin, particularly whether deep water sands are trapped on the slope, or bypass into the deep basin. It also examines what mechanisms led to the formation of a regional shale-dominated unit in the Aptian, the Naskapi Member. In addition, this study attempts to provide a simplified framework for forward stratigraphic modelling in salt-influenced basins, and for understanding and predicting the distribution of sediments in these systems.

Stratigraphic modelling software generally use three approaches to simulate sediment deposition (Granjeon and Joseph, 1999; Huang et al., 2015): **1)** geometric models, which use simple geometric rules to recreate sediment distribution; **2)** fluid flow models, which use physical equations to simulate the transport of individual grains of sediment based on their incorporation with moving fluids; and **3)** dynamic-slope models (diffusion based models), which use empirical transport laws to simulate sediment transport and continuity.

The study area is a 185 km x 215 km region of the central Scotian Basin (Fig. 4.1). This area has the highest density of deep-water wells in the Scotian Basin, and covers a range of salt-tectonic domains (Kendell, 2012). This study focuses on the Lower Cretaceous reservoir sandstone units from the base of the Barremian (130 Ma) to the top of the Albian (101 Ma). This age span, which includes the Upper Missisauga Formation and the Naskapi and Cree Members of the Logan Canyon Formation (Fig. 4.2), is the interval of most producing reservoirs in which basin-scale correlation of seismic markers is possible.

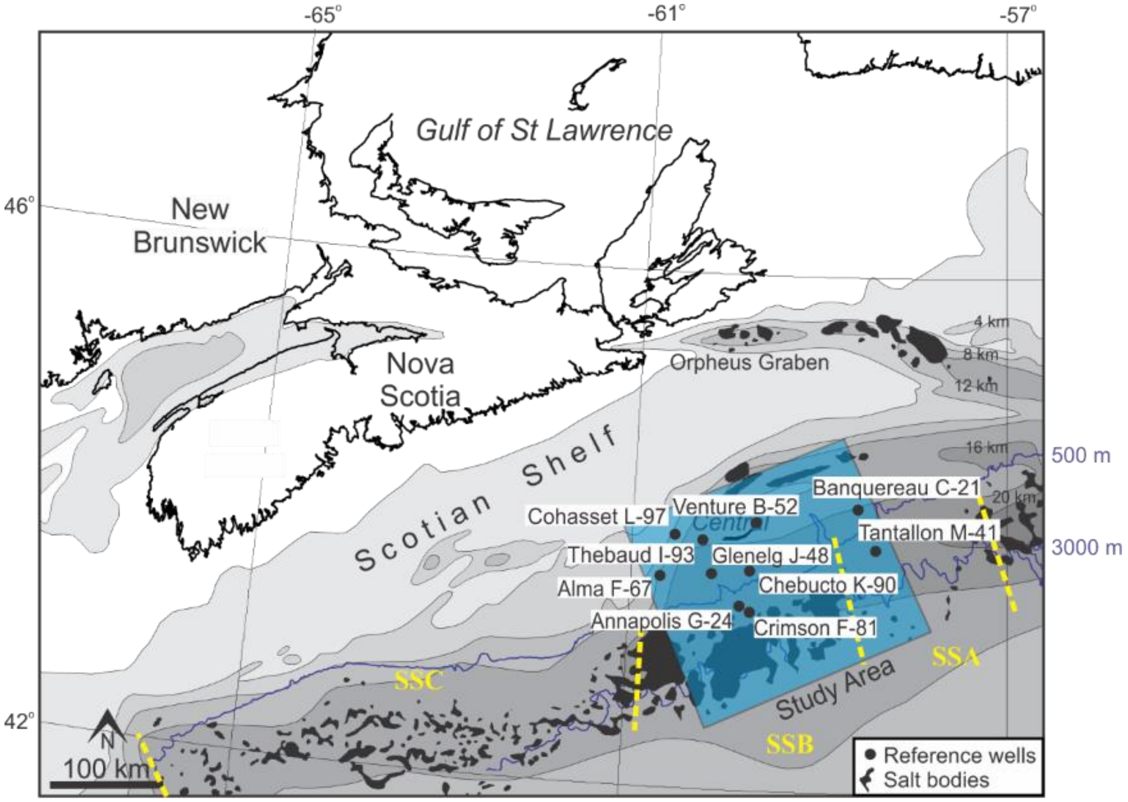

Figure 4.1: Map of study area and reference wells. Grey tones show basin isopachs (in km: Wade and MacLean, 1990). Present 500 m and 3000 m isobaths are shown. Salt tectonic structural styles (SSA, SSB, and SSC) after Albertz et al. (2010). Salt bodies are after Shimeld (2004).

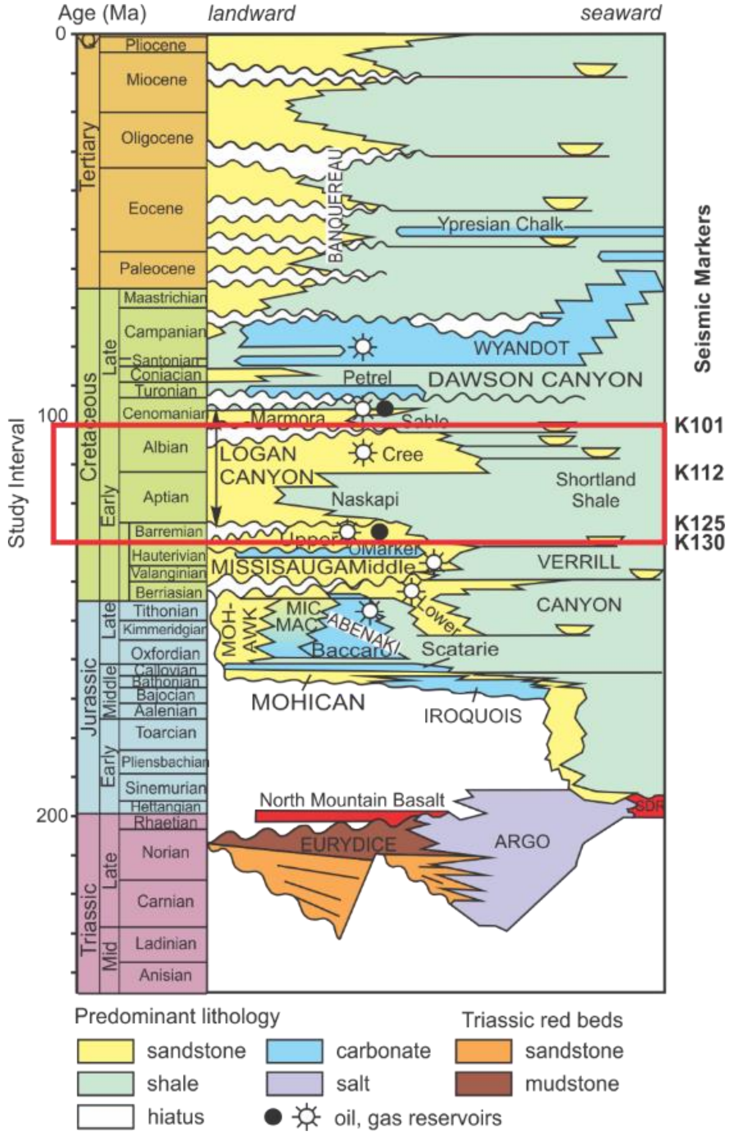

Figure 4.2: Stratigraphic column for the central Scotian Basin (Weston et al., 2012) showing the study interval. Seismic markers after OETR (2011).

This study uses an integrated multi-disciplinary approach to stratigraphic modelling, in which relevant research conducted in the study area is used to determine system inputs. Information regarding the catchment areas (size and relief), sediment properties (grain size and density), and basin properties (bathymetry) during the study time are of particular importance (Hawie et al., 2017). The use of these properties allows for the creation of models which are predictive within a known degree of uncertainty, and can be used to better understand the evolution of sediment sources through time, the impact of changes in source composition, improve our knowledge of sediment transport pathways within the basin, and also predict the distribution of potential reservoir units in the study area. This modelling is used to test; **1)** if provenance pathways based on sandstone petrology (Zhang et al., 2014) are validated by observed sediment distribution and sediment supply; **2)** what proportion of sands were trapped on the slope or bypassed to the deep ocean floor; and **3)** what external factors (e.g. climate, salt tectonics, changing sediment supply from river catchments) control the distribution of sands within the study area.

4.2 Geological setting

The Scotian Basin is located offshore Nova Scotia (Fig. 4.1) and initially formed during the breakup of Pangaea in Mid-Triassic time. It is a collection of depocentres which have accommodated sediments through the Mesozoic–Cenozoic, over which time more than 12 km (to a maximum of 18 km) of sediments were deposited (Wade and MacLean, 1990). These depocentres host the Upper Jurassic to Lower Cretaceous Missisauga and Logan Canyon formations (Fig. 4.2), which are important oil and gas reservoirs in the Scotian Basin (Wade and MacLean, 1990). The thick siliciclastic sediments of the Missisauga and Logan Canyon formations were accommodated by major listric faulting associated with salt withdrawal in the Late Jurassic through Early Cretaceous (Kendell, 2012). Withdrawal occurred as the salt rich evaporite successions of the Argo Formation, which accumulated in the Upper Triassic to Lower Jurassic rift basin, were overlain by Middle Jurassic limestones and Upper Jurassic clastic sediments, deforming and mobilizing the underlying Argo salt.

The Scotian Basin has been divided into several salt structural provinces on the basis of the style of salt deformation. Shimeld (2004) proposed five tectono-stratigraphic salt sub-provinces, which were later reclassified by Albertz et al. (2010) into three principal structural styles (SS) (Fig. 4.1). The region of interest of this study is dominantly a linked salt tectonic system (SSB), with an open-ended roho system and synkinematic sediment wedge (SSA) forming the extreme easterly part of the study area (Albertz et al., 2010) (Fig. 4.1).

Kendell (2012) provided the following synthesis of the evolution of salt tectonics in the central Scotian Basin. The incursion of clastic sediments into the central Scotian Basin during the Early Jurassic mobilized salt of the Argo Formation, generating abundant salt diapirs which combined to form the Sable Shelf Canopy by the Middle Jurassic. After its formation, this canopy began to expel salt basinward, culminating in the Early Cretaceous, as a result of continuing sediment loading by prograding delta systems in the region. In the eastern portion of the study area (SSA), expulsion rollovers resulted in the break-out of salt to the sea floor forming salt tongues. Sediment loading of the expelled salt in the western portion of the basin and the formation of salt tongues in the eastern portion formed minibasins along the slope. In the central basin, salt displacement was dominantly vertical during the Jurassic and Early Cretaceous, however, by the mid Cretaceous displacement had become dominantly horizontal.

Salt migration from the shelf resulted in the formation of diapirs and salt stocks along the slope, eventually forming the Sable Slope Canopy by the Late Cretaceous. Roho-style salt-based detachment faults expelled salt laterally from the slope canopies into the deep basin where it merged with previously expelled salt stock canopies (Albertz et al., 2010; Kendell, 2012).

The Missisauga Formation was deposited during the expulsion of the Sable Shelf Canopy and is composed predominantly of sandstones. It formed between the Kimmeridgian and Barremian, with the Upper member of Late Hauterivian to Barremian age, bounded by the K130 and K125 seismic markers (OETR 2011). The Missisauga Formation is overlain by the Logan Canyon Formation (Wade and MacLean, 1990), the lower part of which is composed of the shale-rich Aptian Naskapi Member (K125–K112) and sand-rich Albian Cree Member (K112–K101).

Provenance studies based on detrital mineral chronology (of zircon, monazite, and muscovite), chemical “fingerprints” of detrital heavy minerals, and bulk rock geochemistry suggest that during the Kimmeridgian–Albian interval, three main river systems supplied sediment to the Scotian Basin: local rivers from the Meguma Terrane, the Sable River, and the Banquereau River (Zhang et al., 2014) (Fig. 4.3). The Meguma Terrane, located in mainland Nova Scotia, supplied sediments through several small rivers to the western and central basin (Reynolds et al., 2012). The Sable River was a large drainage system which sourced sediments from a variety of terrains to the central Scotian Basin, including the Mesoproterozoic Grenville Province of southern Labrador and eastern Quebec, the late Paleoproterozoic Makkovik Province of central Labrador, the Long Range inlier of western Newfoundland, Palaeozoic crystalline basement of the Appalachian orogen, and polycyclic sediments from the Carboniferous Maritimes Basin (Tsikouras et al., 2011; Pe-Piper and Piper, 2012; Piper et al., 2012). The Banquereau River supplied sediment dominantly to the eastern basin and was sourced through the Humber Valley in western Newfoundland from terrains found in central Newfoundland (Tsikouras et al., 2011) with minor sediments sourced from the Grenville and Makkovik provinces in the Labrador Rift (Pe-Piper et al., 2014).

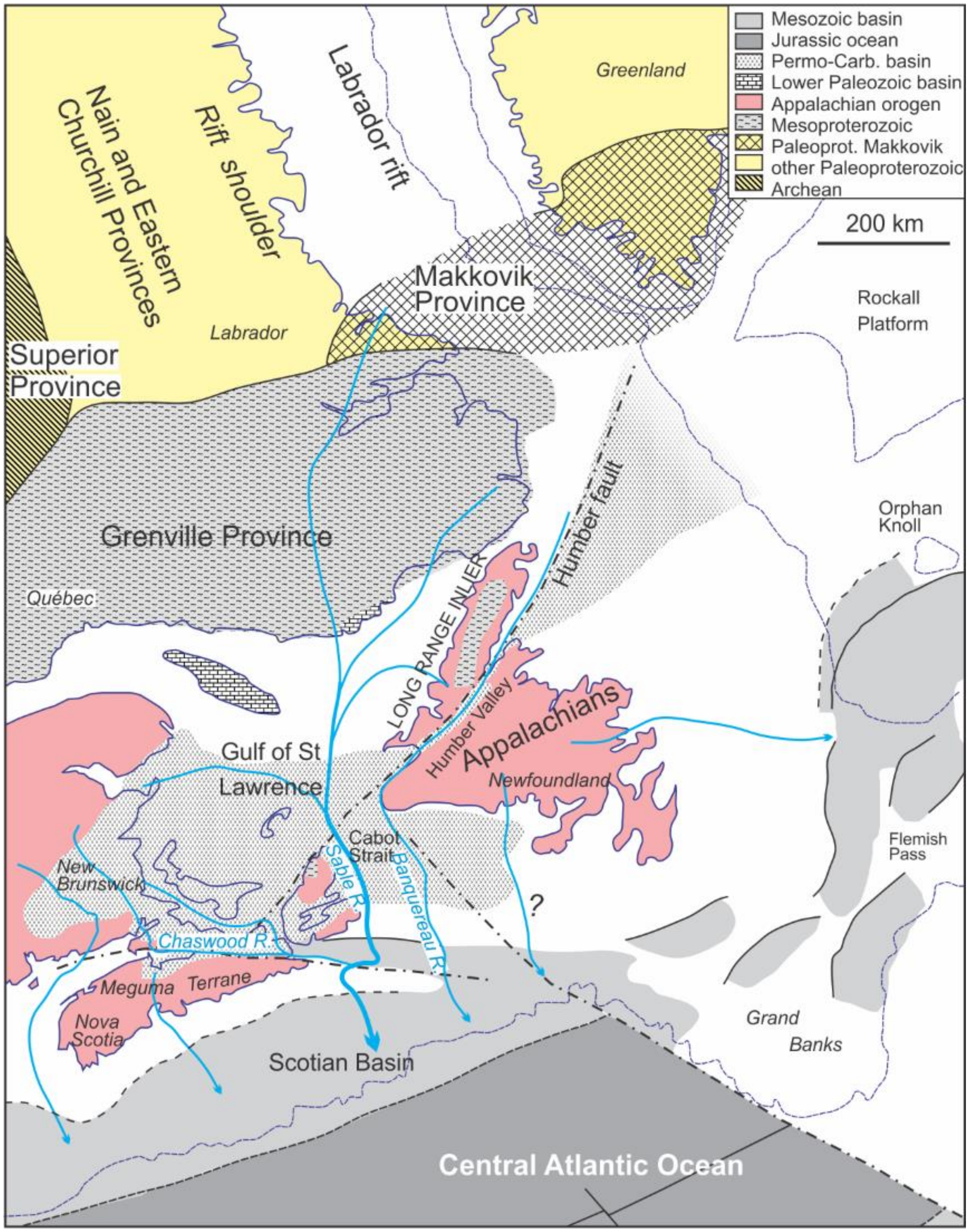

Figure 4.3: Early Cretaceous paleogeography of the hinterland of the Scotian Basin, showing courses of major rivers supplying sediment to the Missisauga and Logan Canyon formations inferred from provenance data by Zhang et al. (2014).

Over time, the catchment areas of these three main sources evolved, with periods of increased and decreased uplift (Zhang et al., 2014). As a result, the three river systems supplying the Scotian Basin were more active at different times during the Early Cretaceous. The Middle and Upper Mississauga formations in the central Scotian Basin received sediments from the Sable River, the Banquereau River, and from small rivers draining the Meguma Terrain (Tsikouras et al., 2011; Piper et al., 2012; Reynolds et al., 2012; Pe-Piper et al., 2014; Zhang et al., 2014). However, there was a shift in sedimentation style during the Aptian, when the Naskapi Member was deposited. This shale prone unit was originally interpreted as the result of high eustatic sea level during the Aptian trapping more sediment inboard within the Scotian Basin (Jansa and Wade, 1975), but recent studies concluded that its formation was in part the result of a tectonic diversion of the Sable and Banquereau rivers (Piper et al., 2011; Bowman et al., 2012; Chavez et al., 2018). Uplift and tilting of the Meguma Terrain (Reynolds et al., 2012) coupled with the extrusion of basalt into the flow path of the Sable and Banquereau rivers (Bowman et al., 2012) diverted these major rivers, resulting in the deposition of the shale-prone Naskapi Member throughout the Aptian. The Naskapi Member was sourced dominantly by the Meguma Terrane at this time, with additional contribution from reworked Upper Missisauga Formation sediments (Chavez et al., 2018), as the increased uplift would have continued to contribute sediments to the offshore. Sand-rich sedimentation returned during the Albian; during this time the uplift of the Meguma Terrane had slowed (Reynolds et al., 2012) and the Sable and Banquereau rivers eroded through the Aptian basalt flows and related uplift (Bowman et al., 2012). These sand-rich sediments comprise the Cree Member of the Logan Canyon Formation, and share similar composition and geochemistry with the Upper Missisauga Formation (Piper et al., 2012; Reynolds et al., 2012; Pe-Piper et al., 2014; Zhang et al., 2014), suggesting a return to the pre-Naskapi Member sedimentation conditions.

4.3 Modelling methodology

In this study, stratigraphic modelling was conducted using DionisosFlow™, a diffusion based forward stratigraphic modelling software that simulates basin infill over geological time scales (Granjeon, 1996). Produced models are then analysed using CougarFlow™ to assess the impact of various simulation parameters, and determine regions of increased sensitivity (Agrawal et al., 2015; Hawie et al., 2015). Models are calibrated against reference wells and seismic surfaces with the goal of reproducing the overall trends of sediment distribution in the basin.

4.3.1 Principles of forward stratigraphic modelling by DionisosFlow™

DionisosFlow™ is a deterministic 4D multi-lithology forward stratigraphic modelling software application. It reconstructs geological processes in a sequence of time steps with the intention of quantifying the average geometries and facies of sedimentary units (Granjeon and Joseph, 1999), reproducing the net result of sediment supply, transport, and accommodation that results from uplift, subsidence, and sea level fluctuation. DionisosFlow™ simulates the transport of sediments within basins by combining empirical water- and gravity-driven diffusion equations based on hill slope creeping (linear slope-driven diffusion with transport proportional to gradient) and water discharge-driven transport (non-linear water and gradient driven diffusion equation). The resulting sediment transport equation is:

$$Q_s = -K_{s_i}/\nabla h - K_{w_i} Q_w^m S^n$$

Where: Q_s: sediment flux [km^2y^{-1}]
K_s: diffusion coefficient of hill slope creeping transport [km^2y^{-1}]
h: elevation (m)
K_w: diffusion coefficient of water discharge driven transport [km^2y^{-1}]
Q_w: dimensionless local water discharge cell (normalised by 100 $m^3/(s\cdot km)$)
S: local basin slope gradient
m and n: represent constants between 1 and 2 (Tucker and Slingerland, 1994)
i: the transported lithology

In order to reproduce natural systems, DionisosFlow™ calculates sediment flow within the basin for two different scenarios: 1) low energy long term (LELT), which is the permanent flow determining the sediment transport from typical fluvial sources and oceanographic processes such as longshore drift, and 2) high energy short term (HEST), which handles sediment flow related to high energy events such as major fluvial floods and turbidites (Deville et al., 2015; Hawie et al., 2018), which may be responsible for transporting most sediment.

The average diffusion coefficient represents the ratio between sediment discharge and basin slope (Hawie et al., 2017): ((Average sediment thickness x basin length (km)) / (time span (Ma) x basin slope (m/km)). The relationship between the diffusion coefficients for each sediment size class is such that smaller grain sizes have higher coefficients than larger grain sizes.

4.3.2 Principles of sensitivity analysis by CougarFlow™

CougarFlow™ is a statistical software used to evaluate the sensitivity of stratigraphic models generated using DionisosFlow™ (Hawie et al., 2015). It uses Response Surface Modelling (RSM), in which multiple models are run. Within these models, uncertain parameters are varied, and the response of the models to these variations generate the response surface (Lacroix and Albadi, 2012). The goal of RSM is to approximate the complex interaction between uncertain parameters and simulation results. This study employs Latin Hypercube sampling RSM. This RSM approach performs simulations with randomly chosen values for the uncertain parameters selected between a predefined maximum and minimum to predict the response of the model to all other values of the uncertain parameters (Delaplace et al., 2013). This approach requires a large number of simulations to be run in order to accurately predict the response. To check the accuracy of the produced RSM, a small number of confirmation runs are performed, and their results compared to the RSM of Lacroix and Aldabi (2012). Monte-Carlo sampling can then be applied to the RSM to make predictions, and generate a probabilistic distribution of the response of the models (Lacroix and Albadi, 2012).

A script is used to generate and export maps of the properties of interest, in this case the distribution of sands. The contents of these maps are then compared to the reference case models to determine the degree to which altering parameters has influenced overall distribution. The maps produced for each simulation in the sensitivity analysis are then compared to one another to produce a map of standard deviation, which can be used to identify sensitive areas. Maps used in this study report variance as a percentage varied (i.e. (SD/Reference case)×100 %) from the reference case model, to show which regions showed the greatest variance relative to the reference case model.

4.3.3 Modelling and calibration strategy

Three separate models were produced to simulate the main units the: Upper Missisauga Formation (130–125 Ma), Naskapi Member (125–112 Ma), and Cree Member (112–101 Ma). Ages are after Gradstein et al. (2005) to align with research conducted as part of the Play Fairway Analysis (OERA, 2016) from which seismic surfaces and previous modelling have been conducted. These units bounded by the seismic markers K130, K125, K112, and K101 (Fig. 1.2), with the K125 and K112 surfaces calculated as part of this study. The K130 horizon has been picked at a regional maximum flooding surface (MFS) which occurred at 130 Ma (OETR, 2011) kniow as the Hauterivian MFS, and is approximitly equivalent to the “O-marker” which marks the base of the Upper Missisauga Formation on the shelf (Wade and MacLean, 1990). As such, the Upper Missisauga Formation has been assumed to begin at 130 Ma for this study. The K101 marker is picked at the Late Albian Unconformity marking the transition of the Cree Member to the overlying Marmora and Sable members (OETR, 2011). The models use a 5 x 5 km grid size and 0.25 Ma time steps with a 185 x 215 km area.

The models were calibrated by altering the sediment supply, water discharge, and sediment grain size proportions of the various sources inferred for each unit, as well as modifying the subsidence to allow for the appropriate sediment accommodation space. The calibration goal is to attain a minimum 80% calibration in basin thickness, individual well thickness in each calibration well based on lithostratigraphic picks for the Upper Missisauga Formation, Naskapi Member, and Cree Member (Table 4.1), and reference well lithofacies. This process generates three ‘reference case’ models, which can be used to make comparisons to the existing geological interpretation of the area, and answer questions regarding the evolution of the basin.

Table 4.1: Stratigraphic unit depths from reference wells in the study area.

Well	Well pick (m)			
	101 Ma	112 Ma	125 Ma	130 Ma
Alma F-67	1908[1]	2543.6[2]	2843.6[2]	3730[1]
Annapolis G-24	3852[1]	4332[2]	5041[2]	5285[1]
Banquereau C-21	2389[2]	3384[3]	3575.5[2]	4175[1]
Chebucto K-90	2640[1]	3512[4]	3689[2]	4853[1]
Cohasset L-97	1550[2]	2109[2]	2220[2]	2409[2]
Crimson F-81	3990[1]	4554[2]	4772[2]	5928[1]
Glenelg J-48	2301.5[1]	3273[4]	3488[2]	4061[1]
Tantallon M-41	3704[1]	4273.7[2]	4400[2]	4738[1]
Thebaud I-93	1746[1]	2541.5[2]	2653.2[2]	3311[1]
Venture B-52	2100[1]	2849[2]	2970[2]	3564[1]

[1]OERA (2016), [2]OETR (2012), [3]Correlation to well picks for the North Banquereau I-13 well in Chavez et al. (2018), and [4]Chavez et al. (2018).

This study simulates only clastic sedimentation, although thin carbonate beds are present in several wells. These carbonates are typically bioclastic, part of transgressive condensed lag units on the shelf (Gould et al., 2012), and pass laterally into condensed sandstones (Cummings et al., 2006). Given the coarse-grained nature of these carbonates, and their facies associations, carbonate beds in this study have been considered to be equivalent to sand-rich sediments during calibration.

Salt tectonics played a major role in the evolution of the Scotian Basin during the Early Cretaceous, but, the detailed evolution of individual salt bodies and associated withdrawal basins is poorly constrained. In order to incorporate the influence of salt tectonics on the basin, only the vertical movement of the salt bodies was considered, using subsidence variations to recreate sediment distribution patterns. A seismic thickness map of the K130–K101 interval (OETR, 2011) defines overall thickness, which is then distributed through time based on average thickness of sediments in wells for each unit (Tables 4.1 & 4.2) to simulate salt movement. Models are simulated assuming zero sediment porosity for all lithologies and therefore maximum sediment compaction is simulated, so that calculated sediment supply is slightly overestimated. Unit thickness calibration is measured using thickness error maps generated from comparing simulated thickness with thickness derived from seismic data (Table 4.2). In regions where the presence or mobilization of salt have resulted in a thickness of zero, the thickness is simulated by extrapolating the subsidence rate from the surrounding area, particularly on the edges of the study area. In the basin, areas with no interpreted surface or zero thickness were treated as salt, and were given low subsidence rates to simulate expulsion.

Table 4.2: Mean thickness and percent thickness of the Upper Missisauga Formation, Naskapi Member, and Cree Member based on reference well picks, excluding the Annapolis G-24 well.

Unit	Average thickness (m)	Percent thickness (%)
Cree Member	745.7	48.5
Naskapi Member	174.8	11
Upper Missisauga Formation	684	40.5

A calibration indicator script is used to determine the percent calibration of the simulated model to well logs from ten reference wells (Fig. 4.1). It compares simulated results of thickness and lithofacies (texture) within the 5 by 5 km cell in which each calibration well is located, to the thickness and lithofacies of the well logs. Given the large difference in horizontal resolution between the cell size of the model and the size of the reference wells, changes in lithology which may be the result of facies changes on a much finer scale than the grid size present a difficult challenge in calibration. The focus of model calibrations is therefore to account for the overall distribution of sediments within the study area.

Lithofacies calibration compares simulated facies to lithofacies at the control wells on the basis of their similarity. Lithofacies of the same class result in 100% calibration, with calibration decreasing with greater difference between facies, such that sandstone vs siltstone returns a greater calibration than sandstone vs shale. As the lithofacies logs for the reference wells are at a much higher resolution than the simulated logs, it is necessary to upscale the well logs. This is achieved by averaging the lithofacies of the well logs within segments which correspond to the average thicknesses of the time steps generated during simulation.

Reference case wells have been classified into lithofacies (e.g. sandstone, shale, sandy shale), based largely on petrophysical interpretations, which have been calibrated against cuttings data. The quantitative proportions of individual grain sizes (e.g. sandstone vs. mudstone) in each lithofacies are not determined. However, simulated models require ranges of sediment proportions to assign lithofacies to simulated well logs. The numerical cut offs for these simulated lithofacies have been chosen to most closely match the observed lithofacies in wells. Sediment concentrations in the reference case models are therefore qualitative rather than quantitative in nature.

To determine the well thickness calibration, the difference between the simulated and actual well thickness is divided by the actual thickness from the well log. It is calibrated by altering the subsidence around individual wells to provide sufficient accommodation space to ensure that each unit is calibrated against sediments from only that unit.

The modelling approach used in this study implemented a closed box approach, in which sediment supplied to the study area remain in the area. This approach leads to the accumulation of sediments at the distal edge of the model, which prevents some sediments from being deposited at their expected distance from the sediment source. In order to determine if sands are capable of reaching the deep basin, the reference case models were extended by two rows and given a bathymetry 2 km deeper than the initial model edge. These rows of cells act as a trench which allows sediments to continue to move past the original model boundary. This approach does not maintain the thickness calibration, but it does allow for the observation of a more realistic distribution of sediment towards the edge of the model and provides a proxy for the volume of sediment bypass.

4.4 DionisosFlow™ Parameters

In order to estimate the order of magnitude of the diffusion coefficients used to simulate sediment transport in DionisosFlow™ and to produce reference case models, data about sea floor bathymetry, subsidence, sea level, water discharge, sediment supply, and sediment properties (i.e. grain size and density) are required.

4.4.1 Bathymetry

DionisosFlow™ requires a starting configuration in order to simulate basin infill: this is the initial bathymetry. The reconstructed paleobathymetry of the K130 surface is used as the initial bathymetry for this study (Fig. 4.4A). Each subsequent model uses the top of the previous reference case model as its initial bathymetry, with reconstructed bathymetric maps (Figs 4.4B-D) used for calibration. Different approaches were used to recreate the bathymetry of the shelf, slope, and basin. Palynological studies from wells in the Scotian Basin (Weston et al., 2012; Natural Resources Canada 2016) were used both for biostratigraphy and for depositional environment that generally is expressed as inner, middle, or outer neritic. Lithofacies interpretations are also available for some wells (Gould et al., 2012). To determine the shelf morphology and bathymetry, the trends in the depositional environments and facies have been interpolated (Fig. 4.4).

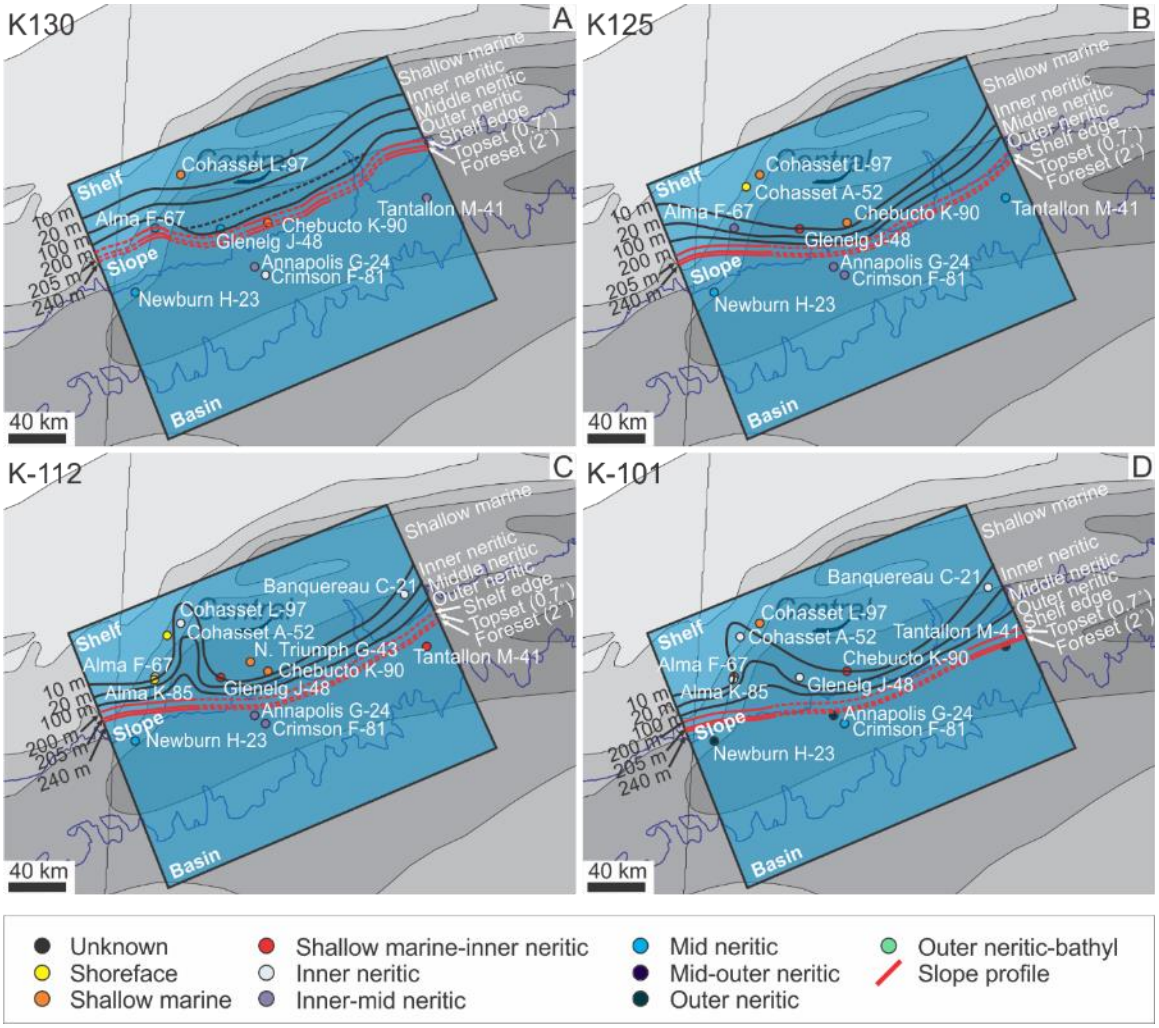

Figure 4.4: Summary of depositional environments during the study interval. A) the base of the Upper Missisauga Formation. B) the base of the Naskapi Member. C) the base of the Cree Member. D) the top of the Cree Member. Paleoenvironment references shown in Appendix 1-8.

The shelf edge is an important component of the paleo bathymetry, marking the shift from the shallow, low gradient shelf to the steeper and deeper continental slope and deep basin. Shelf edge interpretations are based primarily on reflection seismic profiles (Piper et al., 2004; Deptuck, 2008; Smith and Kendell, 2011; Deptuck et al., 2014, 2015) and the shale-out of the O-Marker limestone in the mid Hauterivian (Wade and MacLean, 1990). Shelf edge interpretations have been extrapolated (indicated by the dashed red line in Fig. 4.4) where no data are available.

Recent work has compared ancient and modern clinoforms of various size, age, and sediment composition to determine the relation between topset, foreset, and bottomset height, extent, and gradient (Patruno et al., 2015). These analysis are based on interpretation of published seismic cross sections, which have not been compaction corrected. Such analysis shows that gradients are correlated to one another and that extents also correlate to one another, such that as bottomset gradient increases, so too does foreset gradient. However, gradient and extent do not show a significant correlation. These relationships can be used to determine the likely values for clinoforms in the area given minimal information, such as that present in the central Scotian Basin. Estimates of foreset distance of 1 km from the Alma well (Piper et al., 2004) and an estimated foreset angle of 2°, give a topset angle of 0.7° for 0.4 km and a bottomset angle of 0.6°, which are extended to the edge of the study area.

4.4.2 Sea Level

Eustatic curves representing the fluctuation of sea level through time are used to produce transgressive and regressive events with DionisosFlow™. This study uses the Miller et al. (2005) curve, as it was generated on the basis of research conducted on wells from the western Atlantic margin.

4.4.3 Source evolution

Based on published provenance studies (Tsikouras et al., 2011; Piper et al., 2012; Reynolds et al., 2012; Pe-Piper et al., 2014; Zhang et al., 2014), three sources are used to simulate the Upper Missisauga Formation and Cree Members: a large central source to reproduce the Sable River, an Eastern source to reproduce the Banquereau River, and a Western source to reproduce input from the Meguma Terrane (Fig. 4.5A). During the Aptian blockage of the Sable and Banquereau rivers (Chavez et al., 2018), a single source is used to simulate the Naskapi Member (Fig. 4.5B). Regions of influence for all three sources are based on the results of published provenance studies (Tsikouras et al., 2011; Piper et al., 2012; Reynolds et al., 2012; Pe-Piper et al., 2014; Zhang et al., 2014).

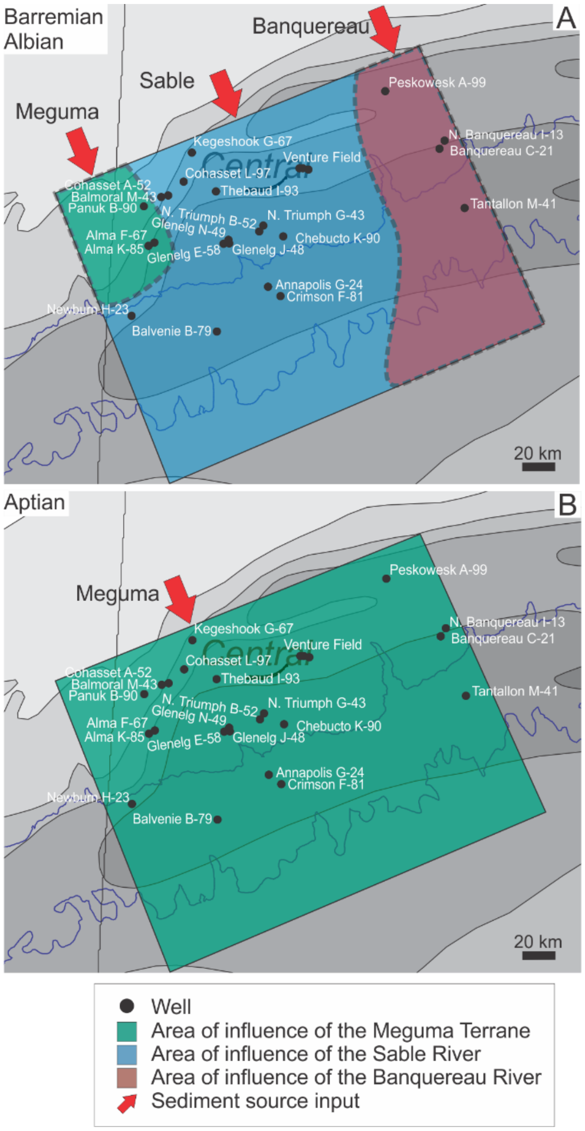

Figure 4.5: Summary of proposed river inputs to the central Scotian Basin during the Early Cretaceous to A) the Upper Missisauga Formation and Cree Member, and B) Naskapi Member.

4.4.4 Uplift and catchment area

Sediment supply from the catchment areas is estimated rather than simulated, and then calibrated on the basis of sediment thickness maps of the study area. The initial estimates of water discharge and volumes of sediment inputs from the various catchment areas are based on comparison with hundreds of modern systems, which shows that as drainage area increases so too does water discharge, and that sediment load increases with relief and drainage area (Milliman and Syvitski, 1992). Published data on detrital minerals and rock geochemistry presented below (Table 4.3) (Fig. 4.6) are used to constrain the catchment areas that supplied sediment to the Scotian Basin. Northward-propagating rifting and ocean spreading in the Late Jurassic–Early Cretaceous (Louden et al., 2004) dominated the paleogeography of the region, leading to uplift of the Labrador Rift (Tappe et al., 2007) and reactivation of old fault lineaments in the Appalachians (Pe-Piper and Piper, 2012). Resulting uplift produced high rates of sediment supply in the later Mesozoic.

Table 4.3: Estimated area, relief, water discharge, and sediment load from all catchment areas supplying the study area.

River	Catchment Area	Area (km^2)	Uplift (km)	Water Discharge (m^3/s)	Sediment Load (km^3/Ma)
Banquereau	Makkovik	36400	1.5	450	2500
	Southern Newfoundland	21550	0.25	275	300
	Humber Valley	5500	0.25	70	200
	Total	-	-	**795**	**3000**
Meguma	Appalachian bedrock	75600	0.25	900	300
	Shear zones	50	0.4	2	60
	Total	-	-	**902**	**360**
Sable	Grenville + Makkovik	146000	1.5	1750	5000
	Carboniferous Maritimes Basin	113600	0.73	1250	1500
	Long Range inlier	5200	0.56	70	200
	Total	-	-	**3070**	**6700**

*Values represent maximum potential values. Cf. Figure 4.6.

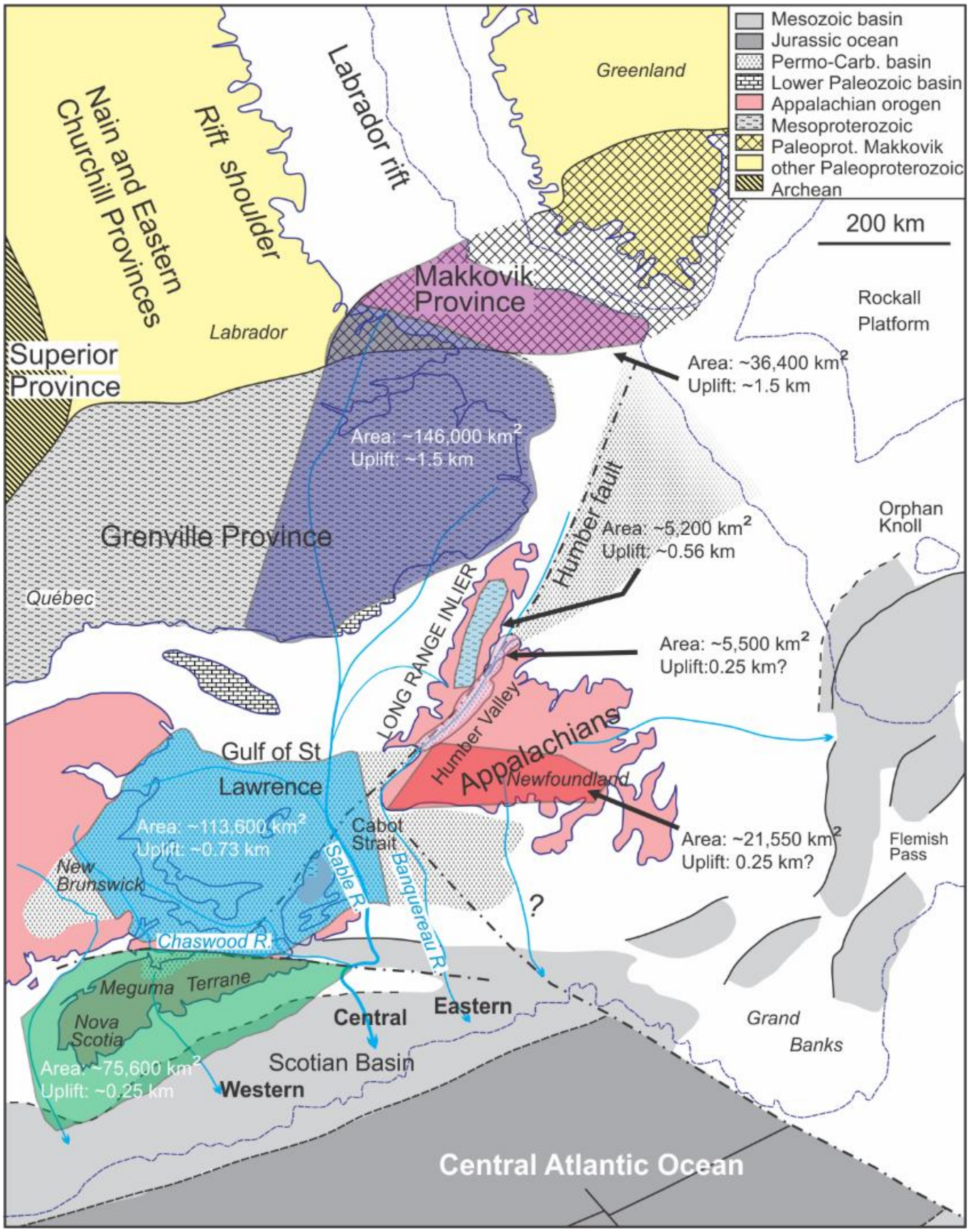

Figure 4.6: Estimates of area of river catchments from different bedrock units and rates of uplift in the hinterland of the Scotian Basin in the Early Cretaceous. Base map from Zhang et al. (2014). Cf. Table 3.

The area of the Labrador rift and Grenville Province supplying the Scotian Basin is estimated on the basis of reconstructions proposed by Zhang et al. (2014) and Pe-Piper et al. (2014). These studies suggest that there was major contribution from the Mesoproterozoic, Grenville Province, and minor supply from Late Paleoproterozoic sources, presumably the Makkovik Province. Therefore, the northern extent of the catchment area should include only a small area of Paleoproterozoic rocks. The western extent of this catchment area is difficult to constrain, as the Grenville Province covers a significant area of Labrador and Quebec. A catchment area is estimated around sediment pathways suggested by Zhang et al. (2014). The area considered for the Carboniferous Maritimes Basin, Long Range inlier (Williams and Grant, 1998), and Humber Valley (Zhang et al., 2014) correspond to their modern extents, truncated at suspected drainage divides based on Zhang et al. (2014) (Table 4.3). The catchment area of southern Newfoundland is based on paleodrainage patterns from Lowe et al. (2011). The contribution of the Labrador rift to the Banquereau River is estimated using the portion of the Makkovik Province on the Labrador side of the rift not contributing to the Sable River (Table 4.3). The fault-bounded Meguma Terrane is constrained based on the region outlined by Reynolds et al. (2009) (Table 4.3). Areas were measured using CorelDraw^{TM} software.

The relief of catchment areas can be assessed from estimated slip on faults, apatite fission track unroofing studies, and modern geomorphological analogues (Hendriks et al., 1993; Reynolds et al., 2009). Relief of the Meguma Terrane is based on sediment budget calculations of detrital muscovite sourced from the Meguma Terrane (Reynolds et al., 2009). The volume of sediments eroded during the Early Cretaceous suggests uplift of about 0.25 km on the inner Scotian Shelf and 0.4 km in shear zones during the Early Cretaceous (Reynolds et al., 2009).

Unroofing studies using apatite fission track modelling are available for the Maritimes Basin and Long Range inlier. The change in temperature over time, based on an average geothermal gradient of 25°C/km, yields uplift of approximately 0.73 km for the Maritimes Basin (Grist et al., 1995), and a maximum of 0.56 km for the Long Range Inlier (Hendriks et al., 1993) for the study period (130–101 Ma). These values may be overestimates, as several studies indicate a regional heating event within the Cretaceous in the Scotian Basin with an estimated gradient of >40°C/km (Grist et al., 1992; Li et al., 1995; Beck and Housen, 2003). In the absence of data from southern Newfoundland and the Humber Valley, a value of 0.25 km based on the tilting of Newfoundland during uplift is used (Twenhofel and MacClintock, 1940).

The Labrador Rift was a major source for the Sable River during the Early Cretaceous, when it was in its rifting phase (Zhang et al., 2014). To estimate its relief, comparison is made with the rift shoulders of the analogous modern East African Rift. Two large scale plateaus on opposite sides of the rift, the Ethiopian and Somalian plateaus, located in the eastern branch of the East African Rift have been considered. These plateaus have been shown to grade from 3600 m and 3000 m respectively on the rift shoulders, to several hundred metres in the lowlands over the course of hundreds of kilometres (Chorowicz, 2005). A mean elevation of 1.5 km, based on the transition from the rift shoulders of these plateaus to the lowlands, has been applied to the Labrador Rift. This value has been used for both the contribution to the Sable and Banquereau rivers.

Values for catchment areas and their estimated relief are plotted on diagrams from Milliman and Syvitski (1992) (Fig. 4.7; Table 4.3). The largest potential source is the Sable River in terms of both water discharge and sediment load, followed by the Banquereau River, and then the Meguma Terrane river(s). Values obtained from the reconstruction of the catchment areas for the various sources are therefore used as maximum values in the simulations.

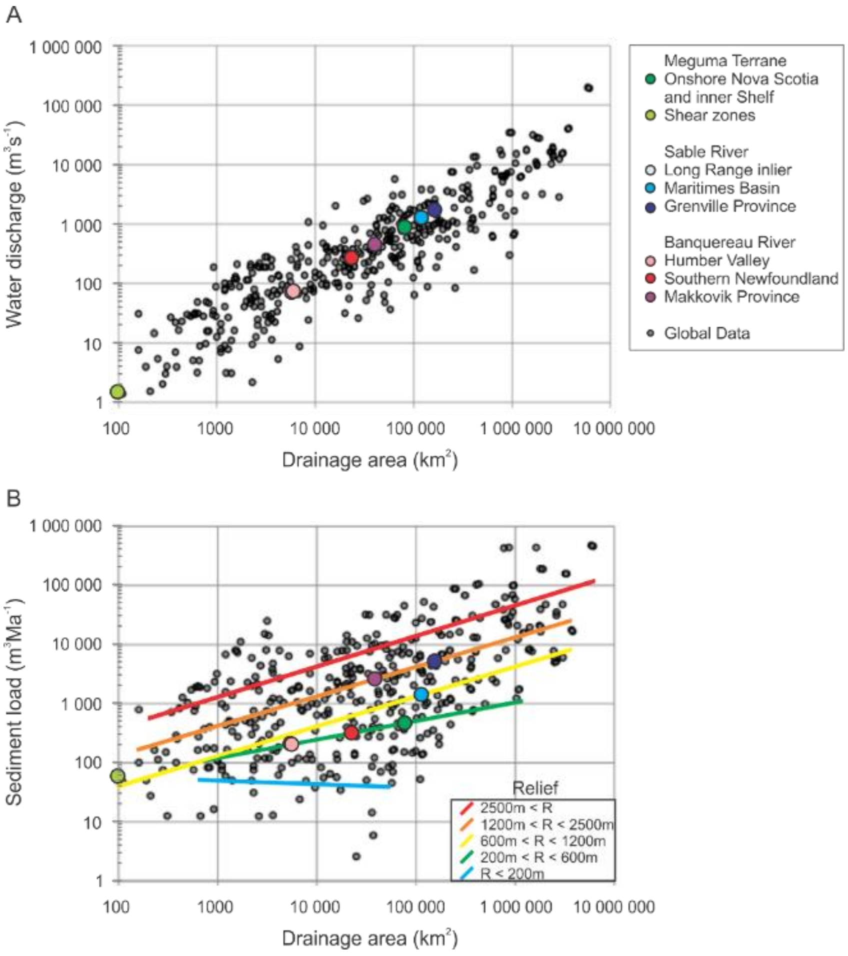

Figure 4.7: The relationship between A) Water discharge vs catchment area for rivers globally (Dai and Trenberth, 2002), with catchment areas for this study plotted along a line of best fit in order to estimate water discharge; and B) sediment load as a function of catchment area and relief (R) (Milliman and Syvitski, 1992), with drainage areas for this study plotted along lines of best fit based on their relief. Modified from Hawie et al., (2017).

4.4.5 Sediment properties

Sediment grain size and density are important variables used in the modelling process. To determine the distribution of grain size throughout the central Scotian Basin, petrographic point counting was performed on 371 samples throughout the study area from the Missisauga Formation and Cree Member. The average grain size is between 100 and 200 µm (Fig. 4.8) and dominantly quartz rich, which suggests that the average density should approximate quartz (specific gravity 2.65; Nesse, 2013). The sediment used in the models was chosen to include the natural range of grain sizes present in the study area, which includes grain sizes of 0.04 mm (flocculated clay), 0.06 mm (silt), 0.075 mm (very fine sand), 0.2 mm (fine sand), 0.4 mm (medium sand), and 0.65 mm (coarse sand).

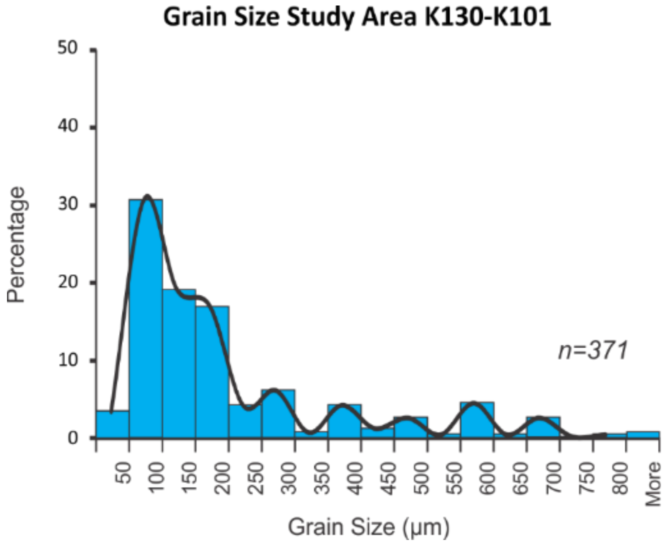

Figure 4.8: Distribution of mean grain sizes of sandstones in the central Scotian Basin from the Upper Missisauga Formation to the Cree Member based on point counting of 371 samples.

4.4.6 Diffusion coefficients

Diffusion coefficients for each sediment class are calculated for each unit separately on the basis of the previously mentioned sediment transport equation (Appendix1-2), with separate LELT coefficients estimated for the shelf and basin environments on the basis of the slope predicted from the bathymetric maps. Diffusion coefficients are adjusted to distribute sediments on the shelf, produce the appropriate slope morphologies, and drive sediments into the basin. The coefficients for all sediment classes are modified by the same proportion, to maintain the ratio between the grain sizes present in natural systems. HEST coefficients are calculated on the basis of the variation in precipitation runoff from the climate modelling of Haywood et al. (2004) for the Barremian in the Weald Basin, UK due to their similar paleo-latitude. Simulations use double the water discharge of the LELT values, HEST events are set to last for 3 month periods, to represent the large influx of precipitation present in the fall in comparison to other seasons. During this time sediment load is also increased by 250% to account for additional sediment transported by the increased water discharge (N. Hawie, personal communication).

4.5 CougarFlow™ parameters

CougarFlow™ sensitivity analysis is designed to test the influence of water discharge, sediment flux, subsidence, and sediment composition on the distribution of sand throughout the study area.

4.5.1 Water discharge and sediment flux

Water discharge determines the energy at which sediments enter the study area, as a result elevated water discharge will result in coarser sediments being dispersed farther and hence deeper into the basin. Sensitivity analysis tests ±10% variation in water discharge for each source. The sediment flux controls the total amount of sediment entering the system. Sufficient sediment is required to produce the compacted total volume of each unit. Furthermore, a decrease in sediment supply results in less coarse sediment being transported to the basin, while oversupply results in more coarse sediment. Sensitivity analysis tests ±20% variation in sediment supply.

4.5.2 Sediment composition

The relative proportions of different grain sizes of the sediment entering the system has been used to calibrate from the lithology interpretations of wireline and cuttings logs in the reference wells. To determine the impact this parameter has on the distribution of sand for each interval, the amount of clay entering the system has been altered by ±25% for all units. Clay content variations, which may simulate fluctuations in climatic processes, influences the distribution of sands, particularly in the deep basin.

4.5.3 Subsidence

The modelling approach recreates the mobility of salt from subsidence rates. However, this approach is only an approximation of the movement based on sediment thicknesses, as it only takes into account a uniform rate of subsidence, and is based on the total thickness divided into the three units. In order to attempt to account for differing rates of salt mobility during this time, the subsidence has been varied (Table 4.5). Such variations have been applied only where the salt canopy is present (OETR, 2011).

Table 4.4: Variation of subsidence for each unit for CougarFlow^{TM} analysis.

Unit	Type	Well	% of total thickness
Upper Missisauga Formation	Thinnest well	Annapolis G-24	17
	Thickest well	Crimson F-81	59.7
	Difference		42.6
Naskapi Member	Thinnest well	Thebaud I-93	7.1
	Thickest well	Annapolis G-24	49.5
	Difference		42.3
Cree Member	Thinnest well	Crimson F-81	29.1
	Thickest well	Cohasset L-97	65.1
	Difference		36

*Variation was generated for each unit by taking the difference between the maximum and minimum percent range from well picks compared to the thickness of the study interval for each unit (i.e. the thickness of K130–K125 compared to the thickness of K130–K101 in the Annapolis G-24 well compared to the Crimson F-81 well).

4.6 Simulation Results

The simulation results of the reference case models for all three units are presented in this section in the context of their paleogeographic location. The shelf is the region proximal to the sediment input with a gradient of less than 1°, terminating at the shelf break. The slope is defined as having a simulated angle greater than 1°, and passes seaward into the basin which is the area of less than 1° gradient seaward of the slope extending to the edge of the study area.

Table 4.5: Summary of estimated water discharge and sediment flux for all stratigraphic units.

Source	Input	Upper Missisauga		Naskapi Member		Cree Member	
		Min	Max	Min	Max	Min	Max
Sable River	Water Discharge (m^3/s)	500	2200	-		400	800
	Sediment Flux (km^3/Ma)	3450		-		2000	
Meguma Terrane	Water Discharge (m^3/s)	250	500	50	150	25	250
	Sediment Flux (km^3/Ma)	450		525		300	
Banquereau River	Water Discharge (m^3/s)	200	700	-		50	200
	Sediment Flux (km^3/Ma)	300		-		175	

Table 4.6: Calibration results for the Upper Missisauga Formation, Naskapi Member, and Cree Member; showing the wells with the lowest and highest facies calibration and the overall calibration.

Unit	Calibration Type	Well	Facies (%)	Thickness (%)	Total (%)
Upper Missisauga	Worst	Cohasset L-97	72.3	97.8	85
	Best	Crimson F-81	95.3	99	97.1
	Total		81.1	90.4	85.7
Naskapi Member	Worst	Banquereau C-21	72.6	95	83.8
	Best	Tantallon M-41	95.1	98.6	96.8
	Total		87.4	91.6	89.5
Cree Member	Worst	Venture B-52	61.2	95.8	78.5
	Best	Crimson F-81	96.5	96.5	96.5
	Total		81.2	90.3	85.8

4.6.1 Upper Missisauga Formation

The simulation of the Upper Missisauga Formation used the Sable River as the principal source of sediment and water, followed by much less supply from the Meguma Terrane rivers and the Banquereau River (Table 4.5). The reference case model is calibrated to optimise thickness and facies prediction at the reference wells. It shows an overall progradational character in the Upper Missisauga. The overall facies calibration is 81.1% with values for individual wells ranging from 72% to 95% (Table 4.6). Unit thickness is calibrated to greater than 80% in the majority of the study area, with lower calibration around the reference-case wells and in association with salt bodies in the basin (Fig. 4.9A).

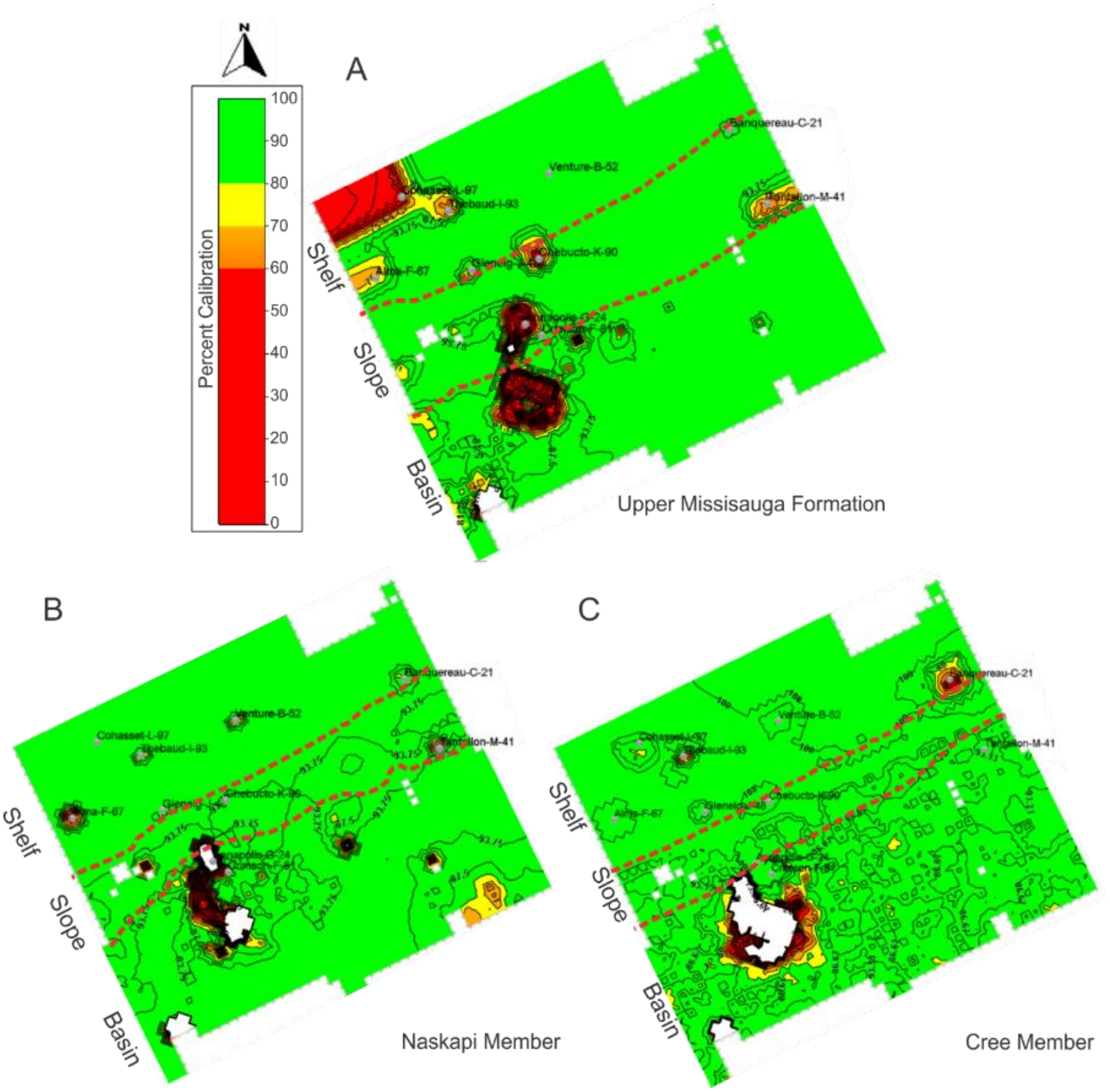

Figure 4.9: Percent thickness error for simulations of : A) the Upper Missisauga Formation, B) Naskapi Member, and C) Cree Member.

The modelled Upper Missisauga Formation is up to 1665 m thick, with the largest sediment accumulations on the slope and farther out in the basin. Thick sediments occur in three regions on the slope: (1) in the western basin seaward of Alma F-67 (1000–1200 m thick); (2) on the eastern slope between Banquereau C-21 and Tantallon M-41 (700–1300 m thick); and (3) in the central slope, east of Chebucto K-90 (~1665 m thick). In the basin, the largest accumulations are near the Crimson F-81 well (1000–1600 m). Sediment pathways resulting from the withdrawal of salt bodies appear to be present basinward of the Alma F-67 well, with thicknesses of less than 1000 m. The remainder of the basin and shelf are generally less than 500 m thick, with the thinnest sediment located within the deep basin.

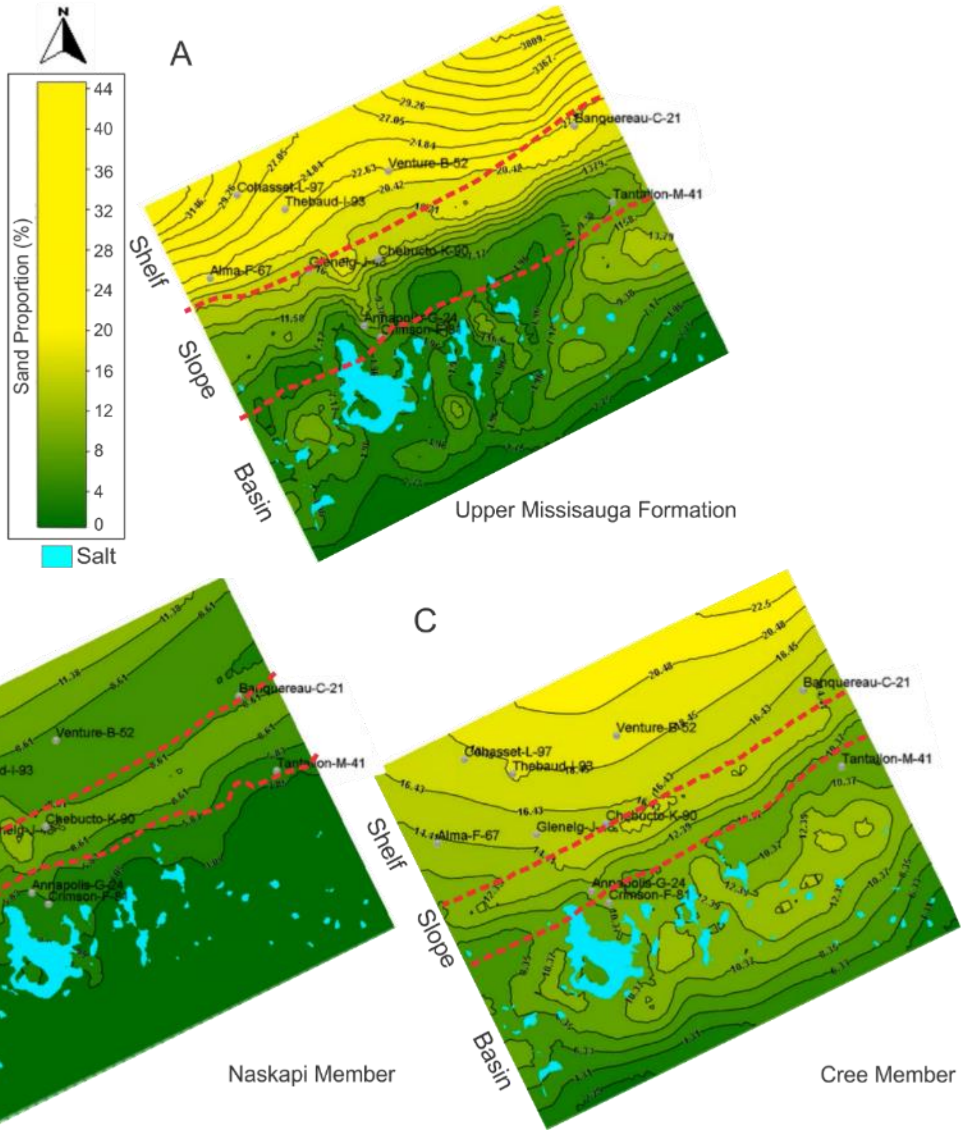

Figure 4.10: Weighted average simulated sand proportion maps for A) the Upper Missisauga Formation, B) Naskapi Member, and C) Cree Member. Blue represents outline of main salt canopies (defined as areas with less than 200 m sediment thickness) and other structures in the distal areas.

The modelled proportion of sand (Fig. 4.10A) shows that sand is dominantly deposited on the shelf, where its proportion ranges from 14–44%, with higher concentrations of sand in the east, decreasing westward. Sand proportions in the basin range from 5–14% and sand extends to the edge of the study area. Sand in the basin tends to collect along corridors and in small basins associated with areas of increased thickness, particularly in the western basin. In the eastern basin, a large body of sand extends beyond the Tantallon M-41 well and contains the highest sand proportion in the basin (>13%).

Table 4.7: Percentage contributions of varied parameters during CougarFlow™ analysis for each stratigraphic unit.

Parameter	Contribution (%)		
	Upper Missisauga Formation	Naskapi Member	Cree Member
Sable River (Clay proportion)	89.2	-	93.8
Banquereau River (Clay proportion)	1.6	-	1
Meguma Terrane (Clay proportion)	2	98	3.1
Sediment Supply	0.17	0.2	1.1
Discharge	4.9	0.1	0.1
Subsidence	2.7	1.5	0.9
SUM	100	100	100

Results of uncertainty analysis on 40 runs (Table 4.7) suggest that the Sable River clay proportion has the largest total effect at 89%, followed by discharge which contributes 5%. A combination of subsidence at 3%, the Meguma Terrane at 2%, and the Banquereau River at 2% make up the remaining contribution (Table 4.7). CougarFlow™ results show that the variance of the sand percentage on the shelf ranges from 9 to 45% of the sand proportion present in the reference case model (Fig. 4.11A). Thus for a mean concentration of sand on the shelf of 30%, a 25% variance would indicate mean values of between 23% and 37% sand. The shelf shows highest variance for sand distribution and variance increases towards the shelf edge. In the basin, sand percentage shows variance of 15–160%. The greatest variation is observed along the slope and basinward of the

Annapolis G-24 and Crimson F-81 wells. Regions displaying low variance (<25%) are observed basinward of the Tantallon M-41, Annapolis G-24 and Crimson F-81, and Alma F-67 wells. High variance (>45%) is also observed at the edge of the simulated area (Fig. 4.11A).

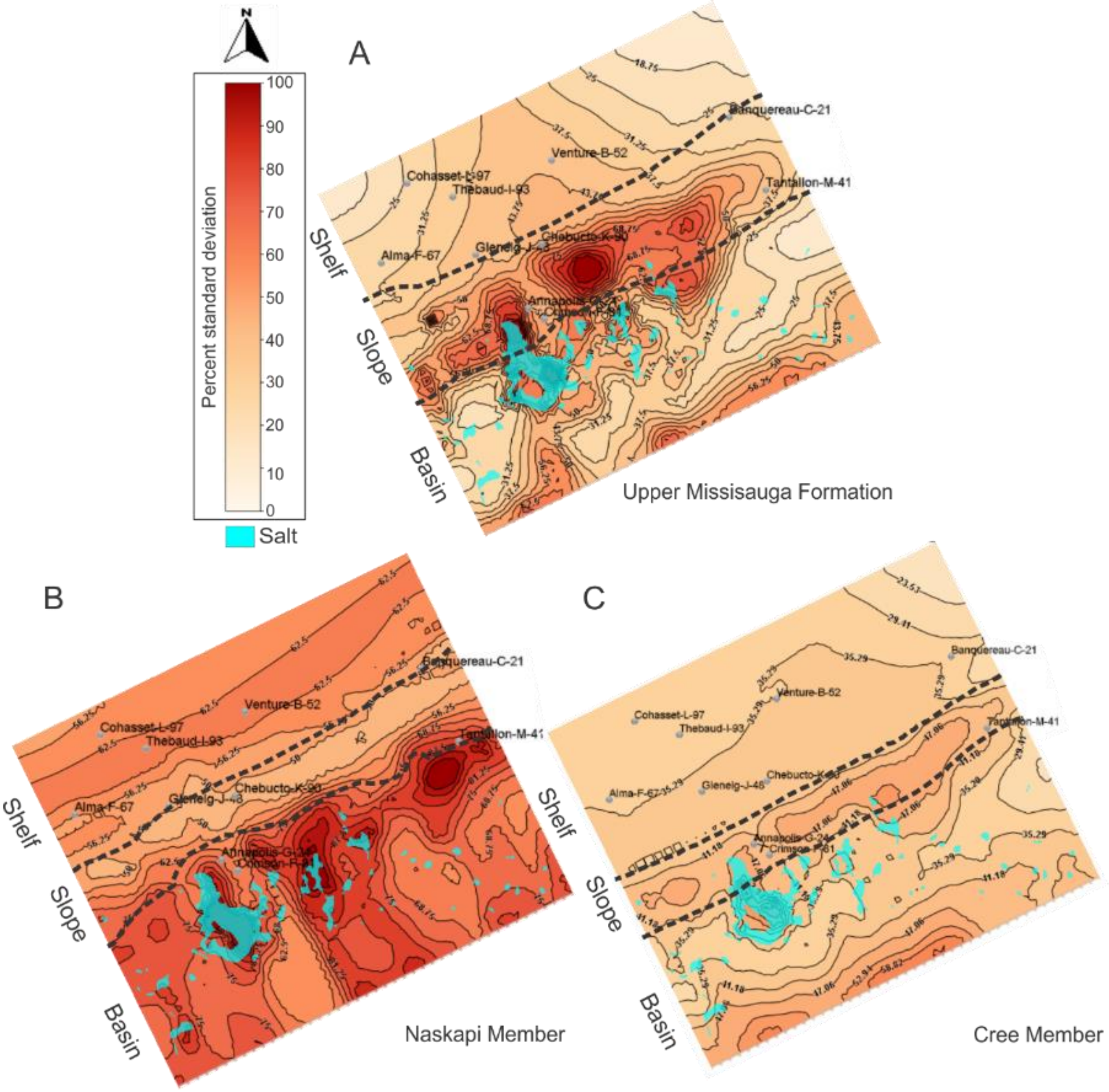

Figure 4.11: Sensitivity maps of simulated sand distribution shown as percent standard deviation for A) the Upper Missisauga Formation, B) Naskapi Member, and C) Cree Member. Blue represents outline of main salt canopies (defined as areas with less than 200 m sediment thickness) and other structures in the distal areas.

4.6.2 Naskapi Member

The Naskapi Member has an overall facies calibration of 87% with values for individual wells ranging from 73% to 95% (Table 4.6). The Naskapi Member was modelled using only one source, from the Meguma Terrane, which was meant to imitate the shift in sedimentation style during this time. The sediment supply from this source was greater than during Upper Missisauga deposition (Table 4.5), but the total sediment budget is several times smaller due to the modelled lack of contribution from Sable and Banquereau river sources. Unit thickness is calibrated to greater than 80% in the majority of the study area, with lower calibration around the reference-case wells and in association with salt bodies in the basin (Fig. 4.9B).

The Naskapi Member shows similar patterns of sediment thickness to the Upper Missisauga. It reaches a maximum thickness of 800 m, with the majority of sediments captured on the slope and the maximum thickness near the Annapolis G-24 well (Fig. 4.10B). Sediments are generally less than 250 m thick on the shelf, and less than 150 m thick in the basin. Sediments follow a similar corridor to the deeper basin as in the Upper Missisauga Formation, although the maximum accumulation is less than 300 m.

The proportion of sand present in the Naskapi Member ranges from 8–20% on the shelf, to 2–8% in the basin. Sand is more evenly distributed in this member than in the Upper Missisauga, and it does not appear to concentrate in corridors in the basin, although, some minor bodies are present on the upper slope. Results of uncertainty analysis after 40 CougarFlow™ runs (Table 4.7) shows that the input from the Meguma Terrane has the largest total effect at 98%, with additional contribution from subsidence at 2% and minor contributions from sediment supply and discharge (Table 4.7). The shale-prone Naskapi Member shows generally greater variance in sand abundances than the other units in this study. CougarFlow™ results show that variance on sand distribution estimates on the shelf ranges from 50 to 65% (Fig. 4.11B). The highest variance on the shelf is mid-way between the landward edge of the simulated area and the shelf edge. The variance on sand distribution in the basin ranges from 55 to 150%. The greatest variation is observed in the basin seaward of the base of the slope (Fig. 4.11B). High variance (>80%) is also observed at the eastern edge of the simulated area. Regions displaying relatively low variance (<60%) are present basinward of the Tantallon M-41 well, and along the slope (Fig. 4.11B).

4.6.3 Cree Member

Simulation of the Cree Member used three active sources as in the Upper Missisauga: the Sable River is the principal source of sediment and water, followed by the Meguma Terrane, and then the Banquereau River (Table 4.5), with the Sable River larger than the other two sources combined. The total sediment flux used to reproduce the Cree Member is lower than that for the Upper Missisauga Formation during each individual time step, suggesting a change in the amount of sediment supplied from the source areas during this time. The reference-case model for this interval has been calibrated to an average of 81% on the basis of lithofacies (ranging from 61–96%; Table 4.6). Unit thickness is calibrated to greater than 80% in the majority of the study area, with lower calibration around the reference-case wells and in association with salt bodies in the basin (Fig. 4.9C).

The Cree Member has a maximum thickness of 2100 m. In this unit there is lesser sediment accumulation in the Annapolis G-24, and Crimson F-81 area relative to the previous units. The minimum thickness on the shelf is 350 m, and the thickness in the basin is typically less than 600 m, excluding the salt corridors and area seaward of Alma F-67, where sediment can be as thick as 900 m to 1650 m and 1000 m to 1800 m respectively. Sand distribution in the Cree Member ranges from 10–25% on the shelf decreasing from east to west to 2–15% in the basin (Fig. 4.10C). Sand in the basin tends to collect along corridors and small basins associated with areas of increased sediment thickness, particularly in the western and central basin. In the eastern basin, large bodies of sand are located south west of the Tantallon M-41 well (>14%), seaward of the Alma F-67 well (>10%), and seaward of the Annapolis G-24 and Crimson F-81 wells (>12%).

Results of uncertainty analysis are shown in Table 4.7, with the Sable River source showing largest total effect at 94% after analysing the results of 40 runs. The remaining contribution is a result of the combination of the Meguma Terrane at 3%, subsidence at 1%, and the Banquereau River at 1% (Table 4.7). The Cree Member shows variances in sand distribution ranging from 20–45% on the shelf, and 20–60% in the basin (Fig. 4.11C). The eastern shelf shows lowest variance (20–30%) in the landward corner of the modelled area, increasing slightly toward the central shelf and shelf edge. Similar to the Upper Missisauga Formation, the greatest variance is observed along the slope (45–60%), whereas low variance (<30%) is found in much of the deep basin (Fig. 4.11C).

4.7 Discussion

4.7.1 Differences between model results and geology

4.7.1.1 Thickness calibration error

Reference-case thickness calibration shows that modelled thicknesses have high errors adjacent to reference wells and salt bodies (Fig. 4.9). The former is an artifact of the procedure used to assign total subsidence to the three time intervals examined, the latter is a result of dividing the total thickness by the average sediment thickness of each well to produce thickness maps for each unit. While this average generates a representative thickness for each unit as a whole, it does not provide a high thickness calibration on the wells: the error is associated with correcting the difference in the calculated “average” versus “actual”thickness. Thickness error is therefore not related to errors in the sediment inputs, but rather to the data to which the thickness is calibrated. Thickness calibration error could be reduced using intermediate seismic picks rather than interpolation.

4.7.1.2 Lithofacies calibration error

Low calibration of lithofacies to reference-case wells was locally noted in the Upper Missisauga Formation, where the Cohasset L-97 and Venture B-52 wells were calibrated to 72% and 74% respectively, and the Venture B-52 well shows a low calibration of 61% in the Cree Member. The low calibration in the Cohasset L-97 well is an edge effect resulting from its proximity to the model sediment input point. Here, coarse sediment fractions accumulate rapidly in the model resulting in low proportions of fine grained fractions. Since the Cohasset L-97 well is relatively muddy in the Upper Missisauga Formation, it yields a low calibration. Detailed correlations in the area of this well show that within three cells of the simulated grid, the Lawrence D-14 well is much sandier (Gould et al., 2012) and would provide a greater degree of calibration.

Abundant fluvial-deltaic channels were active during the Early Cretaceous, particularly in the central basin (Smith and Kendell, 2011), where the Venture B-52 well is located. These channel systems are commonly less than the size of the cells used during simulations, and can be filled with either sand or shale depending on the depositional environment at their time of formation (Cummings et al., 2006). Local autocyclic variability in sand and mud deposition in estuarine and tidal flat depositional systems takes place on a spatial scale that cannot be captured by a model with a 5 km grid or 0.25 Ma timesteps. The poor lithofacies calibrations of these wells are therefore not considered to represent a failure of the model to capture the overall sediment distribution, rather the inability to capture fine scale variation in sedimentation in some areas.

In the Naskapi Member, the lithofacies calibration of the Banquereau C-21 well is only 75%. Well logs suggest that the Banquereau C-21 well contains more sandy intervals than other distal wells in the Naskapi Member perhaps due to local sediment supply from Newfoundland, which was not simulated in this study.

4.7.2 Accuracy of provenance model

Reference-case models were calibrated against unit thickness from seismic picks and at wells with >80% match (Fig. 4.9). Facies were also calibrated to a minimum of 80%, with the exception of wells mentioned in the previous section. This suggests that the provenance model (Fig. 4.3) used to generate simulations supplied a sufficient volume of sediments and recreated the distribution of sand. Simulation of the Naskapi

Member used only a single, small volume, muddy source. This approach resulted in a high calibration of both lithofacies and thickness, suggesting that the large river systems that supplied sediments to the Upper Missisauga Formation and Cree Member were either diverted (for example westward along the modern St Lawrence estuary), or sediment was trapped up-dip from the central Scotian Basin.

While this study does not track the rivers from their catchment areas to the basin, sediment volumes used to generate the models can be used to make inferences regarding the possibility of up-dip sediment accommodation preventing coarse-grained sediments from being transported to the shelf and basin during the Aptian. Simulations suggest that a total of 17,250 km^3 of sediments were supplied to the Scotian Basin during the Barremian, and 22,000 km^3 during the Albian (Table 4.5). If it is assumed that the lower rate of sediment supply during the Albian was also in effect during the Aptian, then approximately 26,000 km^3 of sediments were deposited outside of the Scotian Basin during the deposition of the Naskapi Member. Sediment volumes of this magnitude would require an actively subsiding basin in order to trap the sediments up-dip from the central Scotian Basin. The major sedimentary basins which lay along the proposed sediment supply path of the Sable River are Paleozoic in age, and experienced significant uplift and erosion during the Mesozoic (Keen and Piper, 1990), supplying polycyclic sediments to the Scotian Basin (Tsikouras et al., 2011). The most proximal Lower Cretaceous sediments in the Scotian Basin are found in the Orpheus Graben (Fig. 4.1). However, Aptian sediments in the Orpheus Graben are shale prone, similar to those of the central Scotian Basin (Jansa and Pe-Piper, 1985).

Minor Lower Cretaceous deposits of the Chaswood Formation have been identified in several regions of mainland Nova Scotia and Cape Breton Island (Falcon-Lang et al., 2007). These deposits are the proximal, onshore equivalents of the Missisauga and Logan Canyon formations, and are preserved in several small fault bounded basins. Lower Cretaceous sediments in these deposits are up to 170 m total thickness as preserved, and typically less than 5 km^2 in area (Falcon-Lang et al., 2007). The largest preserved deposit appears to be in the Elmsvale Basin at approximately 40 km^2 in area (Pe-Piper and Piper, 2010), and thus accounts for less than 2 km^3 of Aptian sediment. These onshore deposits are therefore likely too small to have prevented sediments from reaching the Scotian Basin without major diversion of the Sable River, as presently exposed. Although, thermal maturity of contained plant material has been used to infer greater burial (~800m) and therefore thickness in the past (Hacquebard, 1984). Given the high degree of model calibration, high sediment supply volumes, and lack of sufficiently large and active basins along the path of the Sable River during the Aptian, the scenario of the Sable and Banquereau rivers being diverted during this time appears correct.

4.7.3 Sediment input

The style of sedimentation for the Upper Missisauga Formation and Cree Member are very similar in terms of sediment distribution and source. These two units also have a very similar average thickness based on well picks (Table 4.2), despite the Upper Missisauga depositing over a 5 Ma period compared to the 11 Ma period for the Cree Member. The similarity in thickness between these two units requires a lesser rate of input of sediment to the Cree Member. This is reflected in the sediment inputs to the model, which receives approximately half of the Upper Missisauga Formation supply from the Banquereau and Sable rivers, and approximately a quarter less from the Meguma Terrane (Table 4.5). Climate, lithology, and relief are generally considered to be the most important factors in controlling terrigenous sediment supply (Wolman and Gerson, 1978). During the Early Cretaceous the climate of Eastern Canada fluctuated from more arid to more humid. Analysis of K content of detrital sediment (Gould et al., 2014) suggests that the Upper Missisauga was deposited under a humid climate which transitioned upwards to more arid conditions, whereas the Cree Member ranged from relatively arid at the base, transitioning to more humid by the top of the unit. There is thus no evidence that climatic conditions were the cause of the difference in sediment supply. Provenance studies do not suggest that there were any large scale changes in the catchment areas supplying the region, so that a change in lithologies being eroded was not likely a contributing factor. Apatite fission track modelling of the Maritimes Basin and Long Range inlier (Hendriks et al., 1993; Grist et al., 1995), and basement subsidence plots of the Labrador rift (Dickie et al., 2011) do not suggest a decrease in uplift rates during this time. A major change in relief and uplift is therefore likely not the cause for this change in supply. Given that diversion of the Sable and Banquereau rivers had been established during the Aptian, and that other potential influences on sediment supply are not likely to have had a major effect, it is probable that these rivers experienced episodic diversion during the deposition of the Cree Member.

4.7.4 Sand transport

Simulation results show that in the Upper Missisauga Formation and Cree Member sand is trapped dominantly on the shelf (Fig. 4.10A and C), but some was transported into the deep basin along salt-tectonics-related corridors and deposited in withdrawal minibasins along the slope and basin. During deposition of the Naskapi Member, sands were trapped dominantly on the shelf with very limited transport into the basin (Fig. 4.10B). Simulated sand-rich sediment accumulation on the shelf follows a trend similar to that predicted by previous net to gross sand maps (OETR, 2011), with more sands in the eastern shelf decreasing to the west and decreasing significantly at the shelf edge in both the Upper Missisauga Formation and Cree Member.

Seismic interpretations of deep basin sediments also show a trend of sediment pathways developing around areas of increased salt activity (Smith and Kendell, 2011), similar to that in the reference case models (Fig. 4.10). Potentially sand-rich sediment accumulation has been interpreted from seismic data in minibasins to the west and the south of the Annapolis G-24 and Crimson F-81 wells (Smith and Kendell, 2011). Cores from the Tantallon M-41 well show that sands were transported into the basin as a result of prodeltaic sediment failure and turbidity currents (Piper et al., 2010). These authors suggested that, of the sediments transported beyond the shelf break, minor sand was deposited in small minibasins, but that much of the sand was transported past the Tantallon M-41 well and onto the continental rise. Wells from the Alma and Glenelg fields also have evidence for submarine slides which were capable of transporting sands, as well as muds, to the deep basin (Piper et al., 2004).

The distribution of simulated sand bodies (Fig. 4.10) is consistent with the interpretations of these previous studies, supporting their predictions of sand transport into the deep basin, likely as a result of turbidity current flows partially by-passing the slope. The largest concentrations of sand resulting from this style of deposition appears to be in the eastern basin seaward of the Tantallon M-41 well. Sand was also transported along salt-tectonics-related corridors, particularly in the western edge of the simulated area, accumulating seaward of the Alma F-67, Annapolis G-24, and Crimson F-81 wells.

In simulations conducted using the extended map area with a 2 km deep row of cells at the seaward edge of the model, 5–22 % of the sand reaching the slope and basin accumulated at the edge of the model in the Upper Missisauga Formation and Cree Member (compare Fig. 4.12 with Fig. 4.10), suggesting that sands are capable of being transported beyond the study area.

4.7.5 Sensitivity analysis

CougarFlow™ analysis suggest that the largest controlling factor for sand distribution in all three units is the sediment composition (mud proportion) of the largest sediment source to the unit. In the case of the Upper Missisauga Formation and Cree Member this is the Sable River, and in the Naskapi Member it is the Meguma Terrane river(s). The highest variance is generally observed along the slope in association with salt bodies (Fig. 4.11). However, sensitivity maps of the Upper Missisauga Formation and Cree Member also show areas of low variance in the basin, corresponding to areas where elevated sand concentration is predicted (Fig. 4.11). The area basinward of the

Tantallon M-41 well in particular shows low variance in the Upper Missisauga Formation. This suggests that predictions of sand accumulation in this area are robust.

4.7.6 Model limitations

The stratigraphic modelling software is capable of recreating the general depositional environment of the study area. However, it does not always faithfully represent a natural system, for example, because of grid resolution, stochastic controls on facies distribution, model boundary effects and the mobility of salt within the basin. These limitations need to be put in context in order to interpret the simulation results.

4.7.6.1 Closed box

The closed box approach used in the generation of the reference case models used in this study prevents sediments from being deposited with a natural distribution at the edge of the study area. In order to determine the extent to which coarse-grained sediments are capable of being transported beyond the study area, two models have been produced for each unit (Figs 4.10, 4.12). The second set of models add two additional rows of cells along the reference case model boundary which are 2 km deeper than the adjacent cells, and act as a trench which traps any sediment that would have exited the study area in an open model. These extended models show that sand is capable of being transported beyond the study area into deep water. Comparison between the reference case and extended model results are useful for determining if more proximal sediments in the basin are also influenced by the closed box approach.

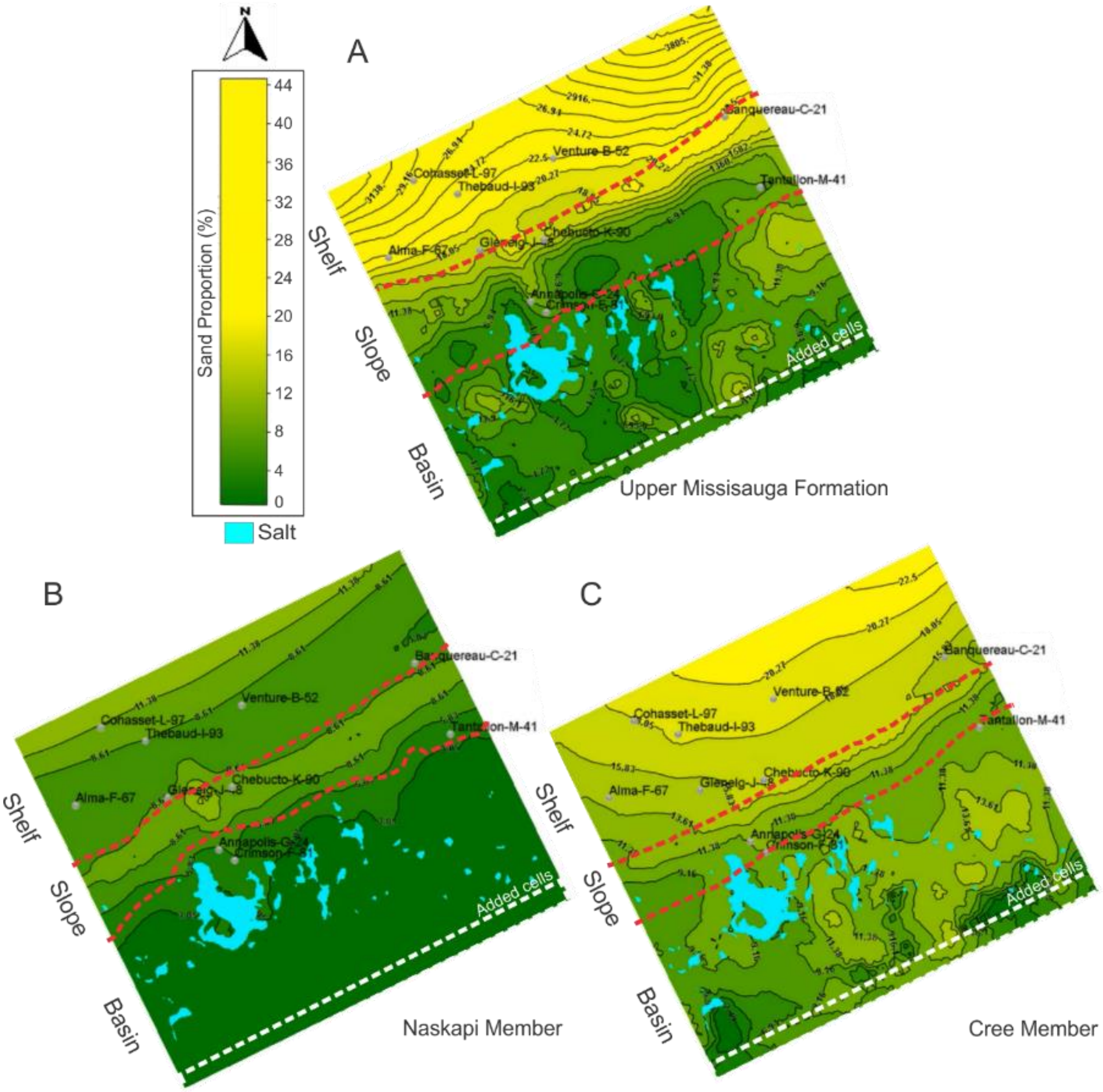

Figure 4.12: Weighted average sand proportion maps for the A) Upper Missisauga Formation, B) Naskapi Member, and C) Cree Member, simulated with an extended downslope map area (white dashed line). Blue represents outline of main salt canopies (defined as areas with less than 200 m sediment thickness) and other structures in the distal areas.

All three units show a bulk decrease in sand content in the basin of approximately 2% for the extended model (compare Figs 4.10 and 4.12), with an increase of 2–10% in sand content at the model boundary in the Upper Missisauga Formation and Cree Member. This increased sand content is concentrated in channels which extend from the sand bodies shown in the reference case models (Fig. 4.10A and C), suggesting that 5–22 % of sediments which crossed the shelf break in the reference case models should have been transported beyond the model boundary. The sand bodies present in the Upper Missisauga Formation (Fig. 4.10A) show lower sand proportions, but their positions are unchanged. Similarly, the mud-prone Naskapi Member does display any significant changes in the basin (Figs 4.10B and 4.12B). In the Cree Member, sand deposits in the western and central basin remain in the same location (Figs 4.10C and 4.11C). However, the large eastern deposit seaward of the Tantallon M-41 well exhibits minor migration towards the model boundary (Fig. 4.11C). While the majority of the sand body has not been displaced, the areas of maximum accumulation within the deposit (Fig. 4.10C) have migrated up to 24 km in the extended model (Fig. 4.11C).

Given that the migration of these bodies is small, and that the remainder of the sand deposits present in the basin have not been affected, the closed box does not appear to significantly influence the distribution of sand bodies in the shallow basin. Therefore, while generating extended models is useful in predicting the behaviour of sand at the edge of the simulated area, it is not necessary in order to understand the distribution of sands on the slope and basin. Additionally, this comparison supports the results of the sensitivity analyses which suggest that the distribution of sand bodies in the reference case models are correct.

4.7.6.2 Salt tectonics

During the Early Cretaceous, salt movement was dominantly sub-vertical in structures along the slope as the salt stocks and diapirs amalgamated, but substantial horizontal expulsion occurred in the basin. Previous modelling studies had limited success in recreating the initial salt distribution (Albertz et al., 2010), although general features of salt movement could be replicated. The simplified approach used in this study captures the net tendencies of sediment accumulation as a result of salt mobilization, not the movement of the salt itself, including the possibility of lateral displacement of overlying sediment. Better definition of the evolution of salt tectonics in the region requires further analysis.

4.7.7 Application of model framework to exploration in the Gulf of Mexico

The Wilcox Group is a Lower Tertiary sedimentary sequence located in the Gulf of Mexico which passes from fluvial deltaic successions onshore to a turbidite system in the deep basin (Brown and Loucks, 2009). Whereas the onshore and deep water deposits of this formation have been drilled and are well understood, the intervening paleo-slope and proximal abyssal plain are poorly defined and are potential targets for exploration. Salt withdrawal is suggested to have modified the paleoslope, producing minibasins and incised canyons (McDonnel et al., 2008). Due to the distance of the deep water deposits from the shelf, and lack of information regarding their deposition, two theories for their origin have been proposed: a draw-down model in which a substantial drop in sea level allowed fluvial system to distribute sediments further into the basin (Rosenfield and Pindall, 2003), and a scenario in which sediments were supplied by a very large river system which was able to prograde hundreds of kilometres into the basin (Sweet and Blum, 2011). Given the general similarity of the Wilcox system to the Scotian Basin, the approach used in our study may be applied to the Gulf of Mexico to predict the general distribution of reservoir sands within these canyons and mini-basins along the slope, as well as to test the hypotheses of sediment delivery to the basin.

4.8 Conclusions

Stratigraphic models of the central Scotian Basin have been produced using DionisosFlow™, a forward stratigraphic modelling software, and analysed using CougarFlow™, a statistical analysis software. These models were calibrated on the basis of reference wells and seismic surfaces, with parameters drawn from previously conducted sedimentological and geophysical studies. The generation of these models has been complicated by the high degree of facies variability present on a fine spatial scale in regions with complex depositional history, and the presence of salt tectonics in the region which are difficult to constrain and have been approximated in this study using unit thickness. Despite these complications, the reference case models have been calibrated to capture the major trends of sediment distribution for the Upper Missisauga Formation (Hauterivian-Barremian), Naskapi Member (Aptian), and Cree Member (Albian). The simplified approach to modelling of salt bodies on the basis of preserved sediment thickness and subsidence has the potential to be applied to other basins where salt tectonics were actively controlling sediment distribution, but where the rate of withdrawal of salt bodies is not well known, such as in the Gulf of Mexico.

The high degree of both thickness and facies calibration present on a basin wide scale suggest that the provenance pathways proposed in the literature for the Early Cretaceous are broadly correct. Sediment supply suggests that the Naskapi Member likely formed as the result of tectonic diversion of the Sable River and Banquereau rivers, and the decrease in sediment supply to the Cree Member compared to the Upper Missisauga Formation, despite a lack in changes to the catchment areas, also suggests episodic diversion of these rivers during the Albian. The sediment budget methodology applied to this study can be used in other regions where sediment routing systems are ambiguous or where the origin of highstand shale units is contested.

Sand distribution maps and sensitivity analyses suggest that sand is distributed dominantly on the shelf, with transport to the basin occurring in salt withdrawal corridors by turbidity current flows. This study predicts that there likely are accumulations of sandy sediments seaward of the Alma F-67, Annapolis G-24, and Crimson F-81 wells, with a large deposit seaward of the Tantallon M-41 well in both the Upper Missisauga Formation and Cree Member. Extended area simulations show sand transport beyond the study area, suggesting that there is potential for exploration in the deep basin. This demonstrates how forward stratigraphic modelling can be applied where depositional settings are controlled by salt tectonism. Sensitivity analysis also shows that sand distribution is controlled by source composition, particularly the Sable River in the Barremian and Albian, and the Meguma Terrane source during the Aptian. Understanding the causes for variations in sediment delivery to the basin is therefore important in predicting the distribution of reservoir units.

Chapter 5: Predictive modelling of reservoir quality associated with the dissolution of K-feldspar during diagenesis: Lower Cretaceous, central Scotian Basin

5.1 Introduction

Porosity and permeability are important factors in determining reservoir quality, however, these properties are susceptible to alteration as a result of both diagenesis and compaction during burial. It is therefore important to understand the factors which promote high reservoir quality, and if possible, attempt to predict where these reservoirs are likely to occur. This study aims to provide a framework for predicting reservoir quality by applying stratigraphic modelling techniques and petrographic studies to the Scotian Basin for anticipating the influence of diagenesis on detrital minerals present in the study area.

While compaction invariably reduces both porosity and permeability (Schmoker and Gautier, 1988; Schmoker and Schenk, 1994; Ehrenberg et al., 2008), diagenesis is capable of both reducing and enhancing these properties. The presence of high-quality reservoirs which deviate from predicted porosity-depth trends is often attributed to limited compaction, limited cementation, or presence of preserved secondary porosity (Taylor et al., 2010). The interaction of sediments with basinal fluids, and increasing temperature and pressure, ordinarily results in decreased porosity and pore throat size via the formation of authigenic quartz overgrowths, clays, and carbonate cements. However, the breakdown of unstable minerals during burial and diagenesis can produce and preserve secondary porosity in the appropriate environments (Taylor, 1996; Taylor et al., 2010; Zhu et al., 2012).

A variety of minerals have been shown to break down during diagenesis, including garnet (Morad et al., 2010), carbonates, and alkali feldspars (Haszeldine et al., 1999). K-feldspar has a high potential for producing secondary porosity as it is a common detrital mineral in many sandstones sediments and therefore can contribute greatly to porosity enhancement. The influence of burial on K-feldspar has been investigated in several basins, e.g. Bohai Bay, east China (Yuan et al., 2015); the Cameros Basin, Spain (Gonzales-Acebron et al., 2010); the Fountain Formation, USA (Walker, 1984); the Haltenbanken area, Norway (Chuhan et al., 2001); the central graben of the North Sea (Haszeldine et al., 1999); and the Scotian Basin offshore eastern Canada (Pe-Piper and Yang 2014). With depth and increasing temperature (Wilkinson et al., 2001), K-feldspar has been shown to break down and produce numerous authigenic phases, including authigenic K-feldspar, albite, kaolinite, and illite. The impact that such by-products have on secondary porosity is dependant on the degree to which they are retained within the system, such that open systems allow for the retention of porosity (Wilkinson et al., 1997; Zhu et al., 2004; Zhang et al., 2014), and closed systems result in any newly generated porosity being filled (Giles and de Boer, 1990; Chuhan et al., 2001; Higgs et al., 2007). Open systems typically contain abundant faults and fractures or beds with high permeability, which allow for fluids to circulate easily. This allows for both the supply of basinal fluids, which break down the K-feldspar, but also for the by-products to be carried away to deposit in other parts of the basin (Haszeldine et al., 1999).

The proportion of K-feldspar to other detrital minerals in sediments is linked to sediment provenance (Tyrrell et al., 2014), so that the variations in K-feldspar proportions during deposition are the result of changes in the rivers from which the sediments were derived. As a result, if the provenance of a region is sufficiently well understood, and the relation between K-feldspar proportion and the provenance sources is re-created, numerical modelling software may be able to predict the initial distribution of K-feldspar within the basin. This distribution can then be compared to regional maps of depth, thickness, temperature, and structure to determine the risk of K-feldspar dissolution and preservation of the resulting secondary porosity. Given the relationship between temperature and K-feldspar dissolution (Wilkinson et al., 2001) and between burial depth and temperature (Issler, 1984), sample depths have been converted to depth below sea floor to better take into account the impact of burial on K-feldspar stability.

This study builds upon previous stratigraphic modelling conducted in the Scotian Basin (Sangster et al., 2019), and focuses on the Lower Cretaceous reservoir sandstone units from the base of the Barremian (130 Ma) to the top of the Albian (101 Ma). This age span, which includes the Upper Missisauga Formation and the Naskapi and Cree Members of the Logan Canyon Formation (Fig. 5.1), is an interval of producing reservoirs within the Scotian Basin which has been the focus of multiple studies that investigated sediment provenance (Tsikouras et al., 2011; Piper et al., 2012; Reynolds et al., 2012; Pe-Piper et al., 2014; Zhang et al., 2014) and diagenetic processes (Gould et al., 2010; Karim et al., 2012; Okwese et al., 2012; Pe-Piper and Yang, 2014; Pe-Piper et al., 2017). The study area is a 185 x 215 km region of the central Scotian Basin (Fig. 5.2).

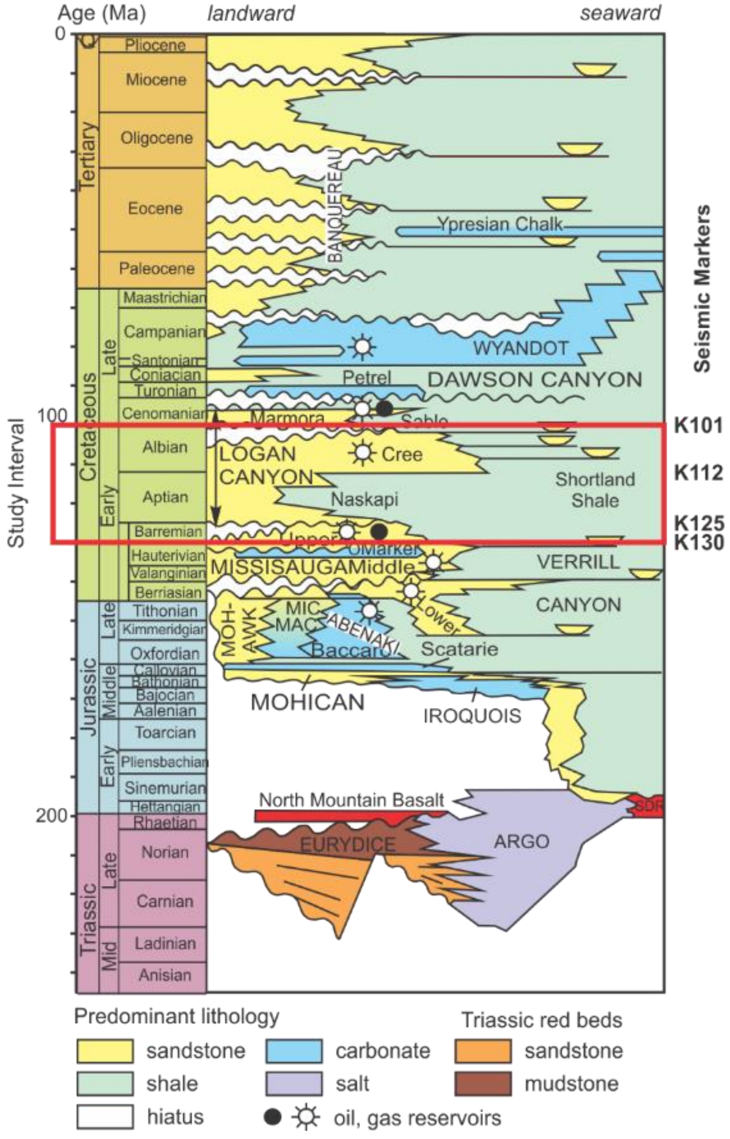

Figure 5.1: Stratigraphic column for the central Scotian Basin (Weston et al., 2012) showing the study interval. Seismic markers after OETR (2011).

K-feldspar distribution is modelled using DionisosFlow^{TM}, a diffusion based, deterministic 4D multi-lithology forward stratigraphic modelling software, which simulates basin infilling over geological time scales (Granjeon, 2014). Reference case models generated in a previous study (Sangster et al., 2019) are used as the basis for these simulations. This study aims to determine **1)** if there is spatial variation of feldspar proportion within the Scotian Basin, **2)** the extent to which the Scotian Basin is influenced by the dissolution of feldspars, and **3)** whether feldspar distribution can be modelled and used to predict reservoir quality.

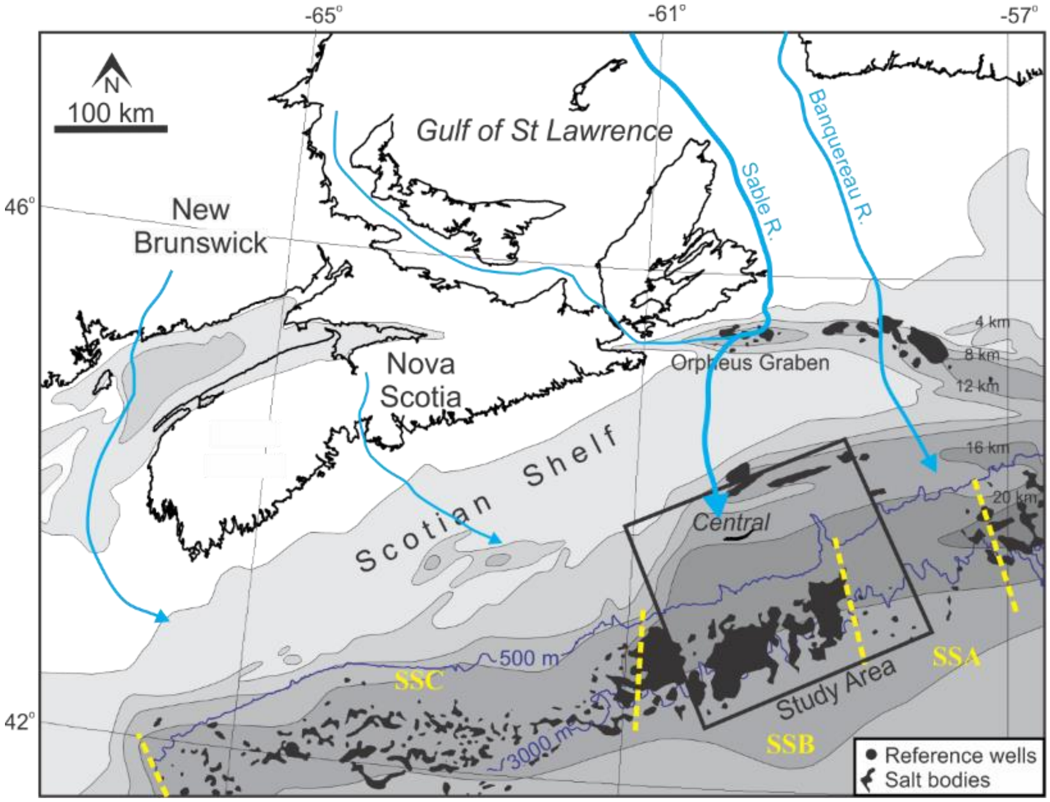

Figure 5.2: Map of study area. Grey tones show basin isopachs (in km: Wade and MacLean, 1990). Present 500 m and 3000 m isobaths are shown. Salt tectonic structural styles (SSA, SSB, and SSC) after Albertz et al. (2010). Salt bodies are after Shimeld (2004).

5.2 Geological setting

The Scotian Basin is located offshore Nova Scotia (Fig. 5.2) and initially formed in the breakup of Pangaea during the Mid-Triassic. It is a collection of depocentres which have accommodated more than 12 km (to a maximum of 18 km) of Mesozoic-Cenozoic sediments (Wade and MacLean, 1990). These thick sediments were accommodated as a result of the remobilization of salt-rich evaporite successions of the Upper Triassic to Lower Jurassic Argo Formation. Mobilization occurred as a result of loading from overlying Jurassic and Cretaceous deltaic-sediments, generating a detached salt sheet in some areas and causing widespread listric faulting in the basin (Ings and Shimeld, 2006; Kendell, 2012). The thick siliciclastic Upper Jurassic–Lower Cretaceous Missisauga and Logan Canyon formations formed as a result of enhanced sediment supply in part from the rising Labrador rift.

The Upper Missisauga Formation is a sand-rich interval which formed in the Late Hauterivian to Barremian. This unit is overlain by the Logan Canyon Formation, which is composed of four members that alternate between shale and sand-dominated units: the Aptian Naskapi Member, Albian Cree Member, and the Cenomanian Sable and Marmora members (Wade and MacLean, 1990).

Provenance studies conducted in the Scotian Basin based on detrital mineral chronology, chemical fingerprinting of detrital minerals, and bulk rock geochemistry suggest that the Missisauga and Logan Canyon formations were deposited by three main river systems that supplied different parts of the Basin (Fig. 5.2): local rivers from the Meguma Terrane, the Sable River, and the Banquereau River (Tsikouras et al., 2011;

Piper et al., 2012; Reynolds et al., 2012; Pe-Piper et al., 2014; Zhang et al., 2014). The western basin was deposited dominantly by the minor rivers draining the Meguma Terrane of mainland Nova Scotia, which also had a minor contribution to the central basin (Reynolds et al., 2012). The central Scotian Basin contains sediments which were transported by the Sable River from a variety of sources, including the Grenville Province of southern Labrador and eastern Quebec, the Makkovik Province of central Labrador, the Long Range inlier of western Newfoundland, crystalline basement of the Appalachian orogen, and polycyclic sediments from the Carboniferous Maritimes Basin (Tsikouras et al., 2011; Pe-Piper and Piper, 2012; Piper et al., 2012). Sediments in the eastern basin were supplied by the Banquereau River from western Newfoundland, including the Humber Valley fault zone (Tsikouras et al., 2011), with minor sediments sourced from the Makkovik Province in the Labrador Rift (Pe-Piper et al., 2014). While several of these rivers transport sediments from catchment areas which contain feldspars, Pb isotope data suggest that the majority of K-feldspar supplied to the Scotian Basin originated from the Grenville province of Labrador and eastern Quebec (Tyrrell et al., 2014).

The Scotian Basin shows a variation in influence of diagenetic processes with depth. Shallow sea-floor diagenetic processes resulted in the formation of Fe-rich clays, siderite, phosphate, and early carbonate cements (Okwese et al., 2012). The Fe-rich clays recrystallized as bertherine rims on quartz grains in thick delta front sandstone beds (Gould et al., 2010). These bertherine rims later converted to chlorite, inhibiting the formation of silica cements and preserving porosity (Gould et al., 2010). Sea-level lowstands produced kaolinite cements as a result of fluxes of meteoric water. With increasing depth of burial, formation waters precipitated quartz overgrowths followed by Fe-calcite and ankerite cements (Karim et al., 2012).

K-feldspar diagenesis has been shown to occur in the Scotian Basin below 1.9 km (Pe-Piper and Yang, 2014), initially with the formation of authigenic K-feldspar and albite following fractures and planes of weakness in K-feldspar grains. With increasing depth, grains are dissolved or replaced by ferroan-calcite and ankerite, with grains ultimately disappearing between 3.8 km and 4.5 km. Dissolution has been interpreted to be controlled by burial depth, and appears to be most significant in permeable sandstone units. Additional secondary porosity has been shown to form as a result of fracturing of quartz and carbonate cements (Karim et al., 2012). During late stage diagenesis, this secondary porosity has been filled by illite, chlorite, kaolinite, siderite, barite, and sphalerite (Pe-Piper et al., 2015). Additionally, occurrences of late diagenetic zircon have been observed in the basin (Pe-Piper et al., 2017).

The high temperature diagenetic mineral assemblages present in the Scotia Basin are related to a widespread thermal event which occurred in the Aptian-Albian (Bowman et al., 2012). This event is recorded by volcanism in the Orpheus Graben, enhanced heat flow in terrestrial basins, high entrapment temperatures in primary fluid inclusions in quartz overgrowths and carbonate cements (Karim et al., 2012), strongly negative $\delta^{13}C$ values in carbonate cements (Karim et al., 2012), apatite fission track modelling (Grist et al., 1998), and the presence of diagenetic zircon (Pe-Piper et al., 2017). Based on these factors, a geothermal gradient of 50°C/km is interpreted for the Aptian-Albian (Pe-Piper et al., 2017). This increased thermal gradient is thought to have heated underlying autochthonous salt and continental basement rocks to temperatures greater than 400°C, which in turn heated circulating brines.

Previous research conducted on the impact of diagenesis on regional reservoir quality in the Scotian Basin by Zhang et al. (2015), concluded that local factors, such as depositional lithofacies and sequence stratigraphy, salt tectonics, secondary porosity, overpressure, and hydraulic fracturing around the top of overpressure, rather than regional factors, are the controlling influence on reservoir quality. Factors which increased secondary porosity are related to the circulation of hot and corrosive basinal fluids through thick permeable sandstones, further promoted by the presence of salt tectonics and the resulting faulting. However, pore throats associated with secondary porosity are commonly small, resulting in a minor contribution to permeability.

5.3 Methods

5.3.1 Feldspar analysis

In order to determine the proportion of feldspar throughout the study area and through time, 48 samples have been analyzed from a total of 15 wells throughout the basin (Fig. 5.3). Samples were taken from sand-rich intervals of Lower Cretaceous sediments. Of these samples 15 are taken from the Upper Missisauga Formation, 5 from the Naskapi Member, 27 from the Cree Member, and a single sample was taken from the Marmora Member (Table 5.2; Fig. 5.4). The central Scotian Basin is represented by 21 samples, with 13 samples taken from the eastern Scotian Basin, and the remaining 9 from the western Scotian Basin (Fig. 5.4).

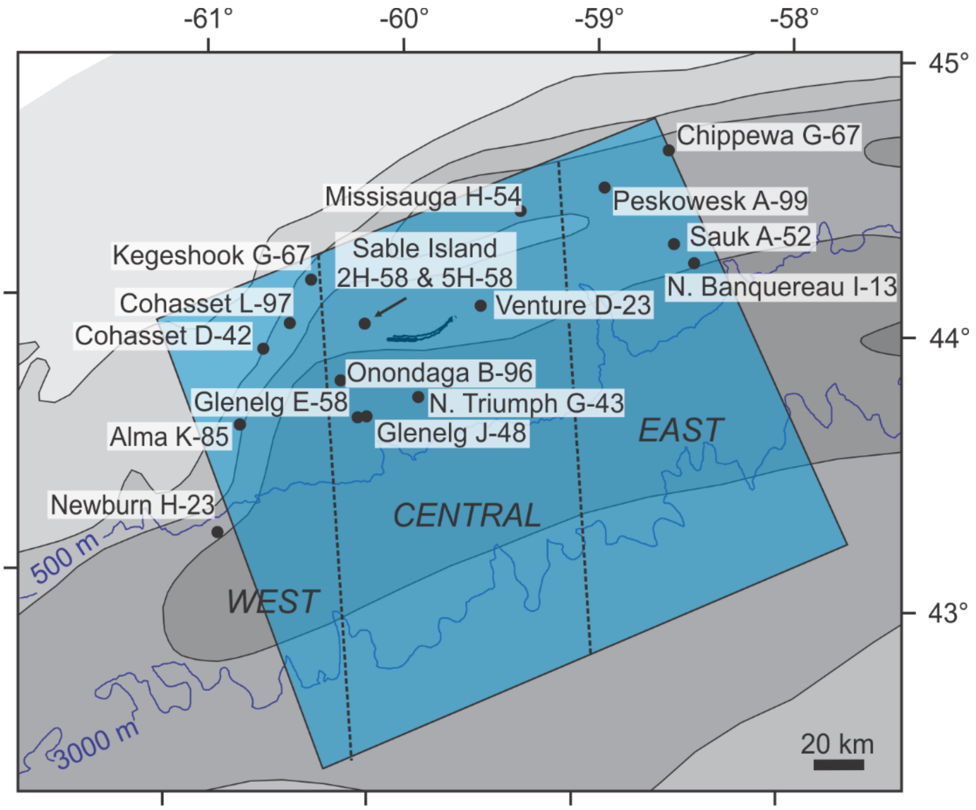

Figure 5.3: Location of wells with analyzed samples, and division of the study area into east, central, and west regions.

All samples were obtained from the Canadian Nova Scotia Offshore Petroleum Board (CNSOPB). Initially sidewall cores were requested, as they provide compositional data for specific depths. However, due to sampling regulations, traditional sidewall core samples were unavailable, and instead sidewall core rubble, which resulted from the breakdown of the fragile sidewall cores, was permitted for sampling. This rubble was sent to Vancouver Petrographics to produce 38 polished, smear slide thin-sections. Eight additional polished thin sections were analyzed from conventional core.

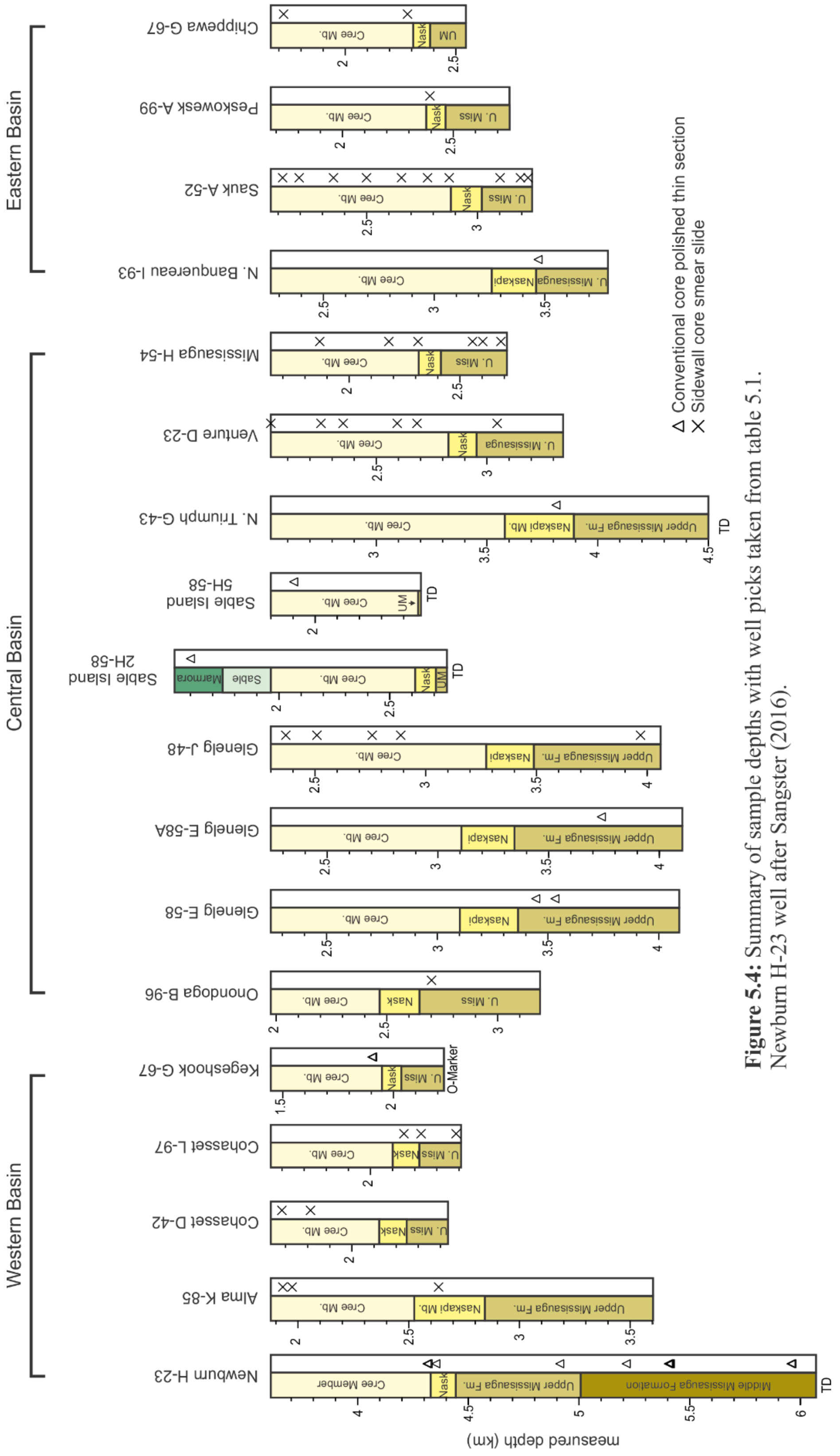

Figure 5.4: Summary of sample depths with well picks taken from table 5.1. Newburn H-23 well after Sangster (2016).

Table 5.1: Stratigraphic unit depths from sampled wells.

Well	Top Marmora Member	Top Sable Member	Top Cree Member	Top Naskapi Member	Top Upper Missisauga Formation	Base Upper Missisauga Formation/TD
Alma K-85	1551[1]	1718.5[1]	1877[1]	2525.3[1]	2843.1[1]	3602[1]
Chippewa G-67	1378[1]	1584.96[1]	1664.2[1]	2307.5[1]	2383.2[1]	2545.1[1]
Cohasset D-42	1298.45[1]	1543.81[1]	1634.3[1]	2122.9[1]	2247.39[1]	2435.4[1]
Cohasset L-97	1245[1]	1409.78[1]	1550[1]	2109[1]	2220[1]	2409[1]
Glenelg E-58	1829[1]	1962[1]	2248.1[1]	3102.8[1]	3364.3[1]	4093[1]
Glenelg E-58A	-	-	2245[2]	3106[2]	3356[2]	4104[2]
Glenelg J-48	1975[1]	2137.6[1]	2301.5[1]	3273[3]	3488[4]	4061[1]
Kegeshook G-67	1122[1]	1355.16[1]	1446.5[1]	1948[1]	2035.4[1]	2228[1]
Missisauga H-54	1316.74[1]	1558.14[1]	1646.5[1]	2313.9[1]	2414.5[1]	2712.1[1]
North Banquereau I-93	1954[1]	2165[1]	2262[1]	3260[3]	3460.2[3]	3785[1]
North Triumph G-43	1861.6[1]	2153[1]	2524[1]	3580.1[3]	3892.9[3]	4504[1]
Onondoga B-96	1596.26[2]	1797.73[2]	1975.74[2]	2468.91[2]	2647.22[2]	3191.6[2]
Peskowesk A-99	1378.5[1]	1582[1]	1675.8[1]	2378[1]	2465[1]	2754.3[1]
Sable Island 2H-58	1528.29[2]	1845.28[2]	1963.55[2]	2615.83[2]	2707.57[2]	2758.44[2]
Sable Island 5H-58	1435.32[2]	1700.8[2]	1802[2]	2464.64[2]	-	2478.05[2]
Sauk A-57	1717.24[1]	1888.24[1]	2067.5[1]	2880.7[1]	3020.3[1]	3247.3[1]
Venture D-23	1666[1]	1913.7[1]	2024[1]	2826.1[1]	2953.1[1]	3344[1]

[1] OETR (2011), [2] MacLean and Wade (1993), and [3] Chavez et al. (2018).

Table 5.2: Summary of samples analyzed showing modal composition and grain size

Sample						Grain size								Composition(%)			
Well	Well #	Type[1]	Depth (m)	Unit	Location	Mean grain size (µm)		Cutoff	Differ[2]		Grains counted			Qz	Kfs	Plag	Total feldspar
						Qz	Kfs		µm	%	Qz	Kfs	Total				
Alma	K-85	S	1928	Cree	West	73	67	30	6	8	434	74	508	88.38	9.06	2.55	11.62
Alma	K-85	S	1971.9	Cree	West	75	65	30	10	14	252	62	314	80.68	15.08	4.24	19.32
Alma	K-85	S	2633	Naskapi	West	69	66	30	3	4	366	65	431	84.76	9.08	6.17	15.24
Chippewa	G-67	S	1718.8	Cree	East	121	108	63	13	10	245	72	317	81.21	17.24	1.55	18.79
Chippewa	G-67	S	2283.6	Cree	East	127	122	63	5	4	400	25	425	94.89	4.61	0.50	5.11
Cohasset	D-42	S	1684.02	Cree	West	73	72	30	2	2	273	49	322	86.48	11.28	2.24	13.52
Cohasset	D-42	S	1813.26	Cree	West	85	76	30	9	11	250	60	310	82.45	13.90	3.66	17.55
Cohasset	L-97	S	2150.1	Naskapi	West	60	51	30	9	15	282	27	309	91.55	6.91	1.54	8.45
Cohasset	L-97	S	2228.7	U. Miss	West	117	92	50	25	21	280	21	301	89.32	7.14	3.54	10.68
Cohasset	L-97	S	2386.9	U. Miss	West	106	93	50	13	12	281	45	326	90.55	8.71	0.74	9.45
Glenelg	E-58	P	3443.86	U. Miss	Central	76	71	30	5	7	266	50	316	90.50	3.22	6.27	9.50
Glenelg	E-58	P	3532.08	U. Miss	Central	168	133	30	36	21	272	46	318	92.89	3.68	3.43	7.11
Glenelg	E-58A	P	3737.9	U. Miss	Central	70	68	30	2	2	291	39	330	89.60	5.26	5.14	10.40
Glenelg	J-48	S	2365	Cree	Central	78	68	30	10	12	265	41	306	82.40	9.91	7.70	17.60
Glenelg	J-48	S	2507	Cree	Central	122	113	50	9	7	274	45	319	87.38	9.26	3.36	12.62
Glenelg	J-48	S	2758	Cree	Central	72	60	40	12	16	256	57	313	85.27	11.95	2.78	14.73
Glenelg	J-48	S	2890	Cree	Central	89	76	30	13	14	262	58	320	87.38	6.54	6.08	12.62
Glenelg	J-48	S	3970	U. Miss	Central	130	-	30	-	-	306	0	306	97.33	0.00	2.67	2.67
Kegeshook	G-67	P	1902.3	Cree	West	258	218	30	40	16	274	87	361	88.21	11.76	3.64	15.40
Kegeshook	G-67	P	1906.36	Cree	West	325	280	30	45	14	244	85	329	90.19	7.62	2.20	9.81
Missisauga	H-54	S	1864.46	Cree	Central	106	97	30	9	9	220	90	310	74.67	22.35	2.99	25.33
Missisauga	H-54	S	2182.34	Cree	Central	154	118	50	36	23	256	64	320	90.16	8.55	1.29	9.84
Missisauga	H-54	S	2310.07	Naskapi	Central	88	68	30	20	23	272	52	324	89.56	9.05	1.40	10.44
Missisauga	H-54	S	2557.27	U. Miss	Central	134	-	30	-	-	304	0	304	99.85	0.00	0.15	0.15
Missisauga	H-54	S	2603.29	U. Miss	Central	87	74	30	12	14	281	60	341	90.58	8.26	1.16	9.42
Missisauga	H-54	S	2689.25	U. Miss	Central	110	92	30	19	17	249	54	303	89.64	8.90	1.46	10.36

[1] P = polished thinsection and S = smear slide; [2] Difference between mean grain size of quartz and K-feldspar.

Table 5.2: (Continued)

Sample						Grain size								Composition(%)			
Well	Well #	Type[1]	Depth (m)	Unit	Location	Mean grain size (µm)		Cutoff	Differ[2]		Grains counted			Qz	Kfs	Plag	Total feldspar
						Qz	Kfs		µm	%	Qz	Kfs	Total				
North Banquereau	I-93	P	3469.27	U. Miss	East	413	380	100	34	8	297	28	325	96.62	1.99	1.38	3.38
North Triumph	G-43	P	3811.53	Naskapi	Central	76	64	30	13	16	340	12	352	96.27	0.93	2.80	3.73
Onondoga	B-96	S	2700.53	U. Miss	Central	60	59	30	2	3	280	42	322	89.16	8.36	2.48	10.84
Peskowesk	A-99	S	2395	Naskapi	East	47	44	20	3	6	268	39	307	90.74	7.70	1.55	9.26
Sable Island	2H-58	P	1600.27	Marmora	Central	155	152	30	3	2	251	70	321	84.81	14.94	0.25	15.19
Sable Island	5H-58	P	1903.66	Cree	Central	149	144	30	5	4	266	57	323	86.98	11.96	1.06	13.02
Sauk	A-52	S	2118.97	Cree	East	137	131	50	6	4	265	71	336	91.00	7.11	1.90	9.00
Sauk	A-52	S	2189.99	Cree	East	95	103	30	-8	-9	229	78	307	85.58	9.82	4.59	14.42
Sauk	A-52	S	2350.01	Cree	East	104	90	30	14	14	201	106	307	79.86	16.50	3.64	20.14
Sauk	A-52	S	2498.14	Cree	East	67	59	30	8	12	249	74	323	89.95	5.71	4.34	10.05
Sauk	A-52	S	2656.94	Cree	East	97	88	30	9	10	248	88	336	86.35	12.77	0.88	13.65
Sauk	A-52	S	2776.73	Cree	East	200	187	30	13	6	263	78	341	86.35	12.78	0.88	13.65
Sauk	A-52	S	2871.52	Cree	East	67	61	30	6	9	269	35	304	93.52	4.69	1.79	6.48
Sauk	A-52	S	3107.13	U. Miss	East	111	83	30	28	25	290	42	332	95.14	2.95	1.90	4.86
Sauk	A-52	S	3199.79	U. Miss	East	196	158	50	38	19	273	32	305	96.04	3.22	0.74	3.96
Sauk	A-52	S	3233.01	U. Miss	East	160	138	50	23	14	276	31	307	91.14	7.91	0.95	8.86
Venture	D-23	S	2026	Cree	Central	97	85	30	12	12	245	57	302	92.28	6.65	1.08	7.73
Venture	D-23	S	2254	Cree	Central	66	58	30	8	11	255	48	303	92.02	4.35	3.63	7.98
Venture	D-23	S	2357	Cree	Central	158	146	50	12	8	285	30	315	86.89	10.22	2.89	13.11
Venture	D-23	S	2606	Cree	Central	116	93	30	23	19	273	48	321	94.73	3.45	1.81	5.27
Venture	D-23	S	2690	Cree	Central	104	99	50	5	4	248	71	319	86.89	10.22	2.89	13.11
Venture	D-23	S	3055	U. Miss	Central	83	70	30	13	16	268	46	314	88.74	7.83	3.43	11.26

[1] P = polished thinsection and S = smear slide; [2] Difference between mean grain size of quartz and K-feldspar.

In order to determine the composition of these sandstones, point counting was conducted using back-scattered electron (BSE) images from a scanning electron microscope (SEM). The rubbles contain a large variety of grain sizes as a result of their fragmentation. As a result, distinguishing between some mineral phases can be difficult using the optical microscope, but SEM analyses also allows for more precise chemical differentiation of minerals. An approach similar to that of Zhang et al. (2015) has been applied to point counting analysis, in which minerals are differentiated on the basis of chemical analysis and by using their gray-scale brightness, which is controlled by their mean atomic number on a scale from 0–255 (Tovey and Krinsley, 1992). Samples have been analyzed using three techniques (Table 5.2): **1)** SEM electron dispersive spectroscopy (EDS) analysis; **2)** SEM EDS and X-ray mapping analysis; and **3)** X-ray mapping analysis. Samples analyzed using only SEM EDS analysis rely on gray-scale brightness to identify minerals which have not been directly analyzed, as a result quartz and plagioclase species cannot be reliably differentiated. SEM analysis was completed in the Regional Analytical Centre at Saint Mary's University using a LEO 1450 VP SEM, acquiring the back scattered electron (BSE) images and electron-dispersive spectroscopy (EDS) chemical analyses of minerals. This SEM has a maximum resolution of 3.5 nm at 30 kV. It is equipped with an INCA X-max 80 mm^2 silicon-drift detector EDS system that has a detection limit >0.1%. A tungsten filament produces a 10 μm beam, and is calibrated with a cobalt standard.

A minimum of 600 detrital mineral grains were counted in each sample. A combination of X-ray maps and large numbers of EDS analyses were taken at each site to identify the various detrital species. BSE images were processed using CorelDraw^{TM} software, and analyzed using MultiSpec^{TM} to determine the area percentage of all grains in the images on the basis of their gray-scale brightness. Due to the reliance on smear slide samples in this study, it is difficult to determine if minerals are detrital or diagenetic. Detrital mineral assemblages in the Scotian Basin are dominated by quartz and feldspar species, therefore, the compositional data from these samples is represented as the normalized percentage of quartz, plagioclase, and K-feldspar. Point counting results are measured in abundance by volume, however, for simplicity the results are expressed as a straight percent. Grain size was measured using ImageJ^{TM} image processing software. Quartz and K-feldspar grains were measured manually, with minimum of 300 total grains measured for each sample (Table 5.2). A minimum grain size cut-off was based on the size of the finest quartz grain present (Table 5.2).

5.3.2 Principles of forward stratigraphic modelling by DionisosFlow

DionisosFlow^{TM} is a deterministic 4D multi-lithology forward stratigraphic modelling software that simulates basin infill over geological time scales by reproducing the net result of sediment supply, transport, and accommodation that results from uplift, subsidence, and sea level fluctuation (Granjeon, 1996). It simulates sediment transport using empirical water and gravity driven diffusion equations based on hill slope creeping (linear slope driven diffusion with transport proportional to slope) and water discharge driven transport (non-linear water and slope driven diffusion equation). The average diffusion coefficient represents the ratio between sediment discharge and basin slope (Hawie et al., 2017): ((Average sediment thickness x basin length (km)) / (time span (Ma) x basin slope (m/km)). In this equation, different sediment size classes are assigned individual diffusion coefficients such that smaller grain sizes have higher coefficients than larger grain sizes. Diffusion coefficients and river inputs defined iteratively in “reference case models” (Sangster et al., 2019) calibrated to lithofacies in wells and total sediment thickness. Two types of diffusion coefficients are employed by this software to simulate a natural system: 1) low energy long term (LELT), which is the permanent flow determining the sediment transport from typical fluvial sources and oceanographic processes such as longshore drift, and 2) high energy short term (HEST), which handles sediment flow related to high energy events such as major fluvial floods and turbidites (Deville et al., 2015; Hawie et al., 2018).

5.4 Results

5.4.1 Feldspar analysis

5.4.1.1 Feldspar proportion

Analyzed samples show a wide range in feldspar proportion, from 0–22%, with an average of approximately 8% (Table 5.2). Samples with the highest average K-feldspar proportion are located in the western basin at 10%, with both the central and eastern basin having an average proportion of approximately 8% (Table 5.2). Samples taken from less than 2 km burial depth all belong to the Cree Member, while samples from depths below 3 km are all Upper Missisauga Formation. Between 2 and 3 km burial depth samples from all three units are present at overlapping depths (Fig. 5.5).

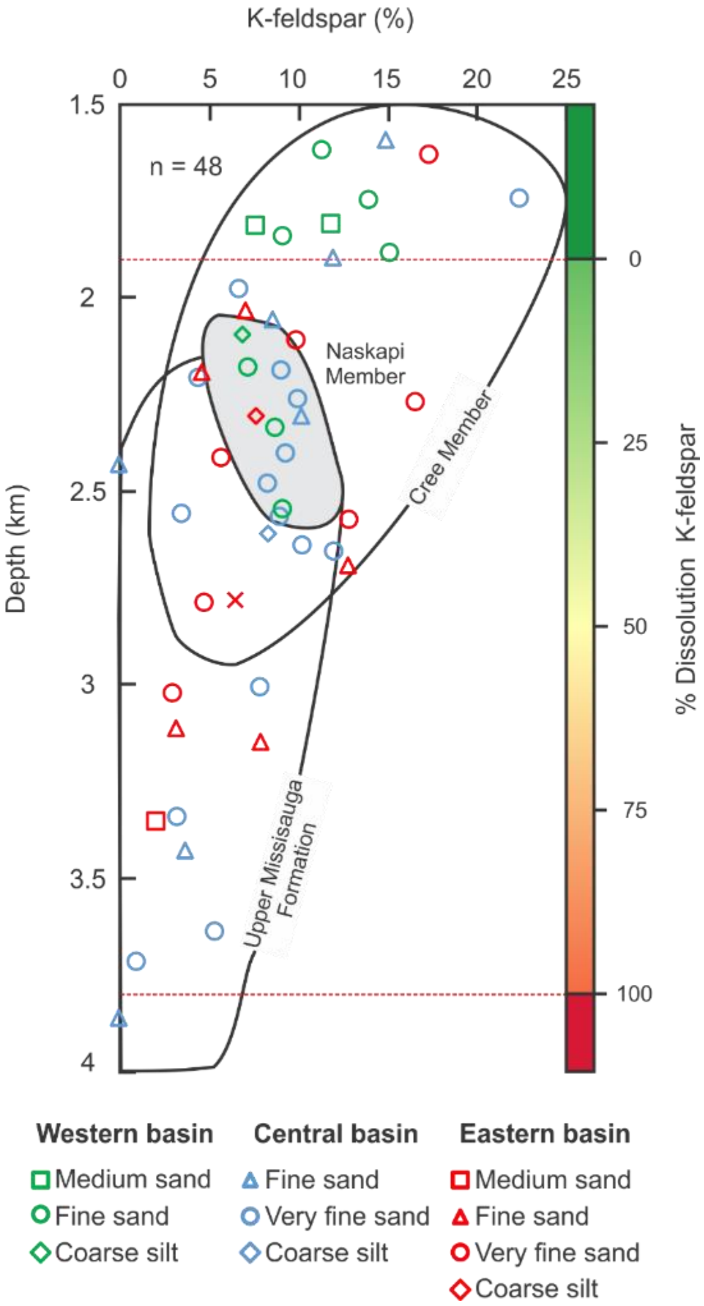

Figure 5.5: Plot of modal composition vs depth. Fields outline the unit from which samples have been taken.

Samples have been analyzed from depths ranging from 1590–3862 m. Their modal composition shows a decrease in the proportion of K-feldspar with increasing depth (Fig. 5.5), with samples shallower than 1.9 km showing an average K-feldspar proportion of 14%, decreasing to 8% from 1.9–3 km, and to 4% at burial depths greater than 3 km (Fig. 5.5). Of the 48 samples analyzed, only two show a K-feldspar proportion of 0%: both samples are from the central basin and were taken from depths of 2429 m and 3862 m (Table 5.2). When K-feldspar proportion is compared to mean grain size, the widest ranges in proportion are observed in the fine and very fine sand fractions (Fig. 5.6). The highest mean K-feldspar proportions are observed in the very fine sand fraction at 9%, followed by coarse silt at approximately 8% and the medium and fine sand fractions sharing a value of 7% (Table 5.2). All of the samples with greater than 15% K-feldspar are present in the very fine grained sand fraction (Fig. 5.6), although these samples are largely from shallow burial depths of less than 1.9 km (Table 5.2).

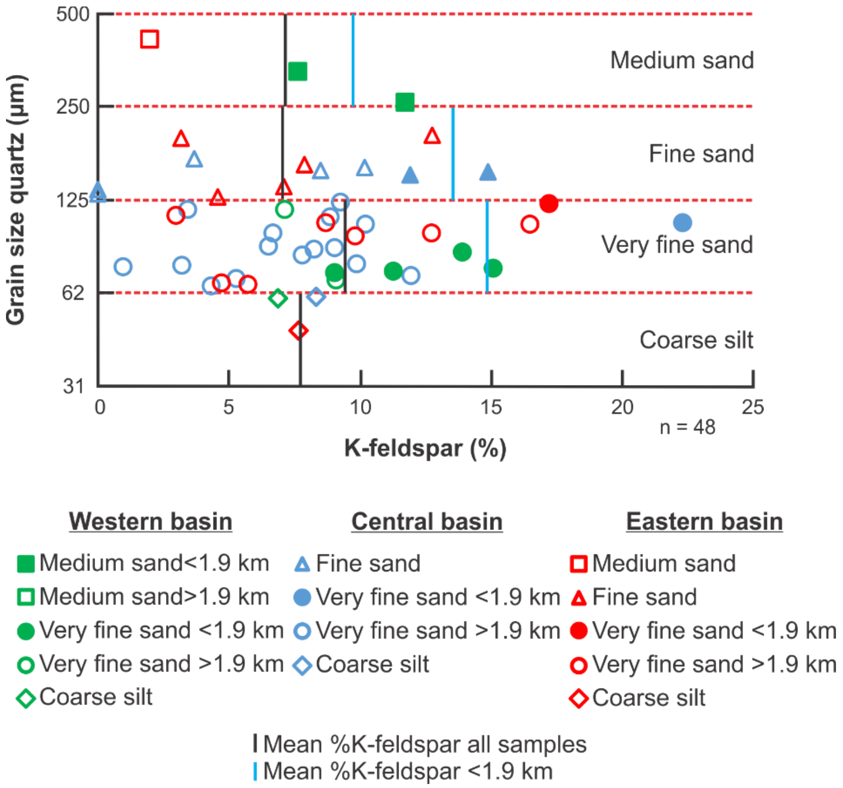

Figure 5.6: Plot of mean grain size of quartz vs. percent K-feldspar.

5.4.1.2 Grain size analysis

The majority of samples analyzed, 30 out of 48 samples, have a modal composition of very fine sand, with the next most frequent grain size being fine sand (Table 5.2). Measured K-feldspar grains within these samples are, on average, smaller than the measured quartz grains (Fig. 5.7). The difference between grain sizes ranges from 2% to as high as 25%, with only one sample having a larger K-feldspar mean grain size (Table 5.2). When the difference is compared to the proportion of K-feldspar in each sample (Fig. 5.8A), a greater difference is observed in association with lower K-feldspar proportions. Samples containing less than 10% K-feldspar show a maximum difference of 25% and average of 12% compared to a maximum of 16% and an average of 9% difference in samples with greater than 10% K-feldspar (Fig. 5.8A). Unlike K-feldspar proportion, grain size analysis does not show a clear relationship with depth of the difference between quartz and K-feldspar grain size (Fig. 5.8B). Samples with a mean grain size of fine or very fine sand show the greatest range of difference, however, average differences are similar for all grain sizes (Fig. 5.8C).

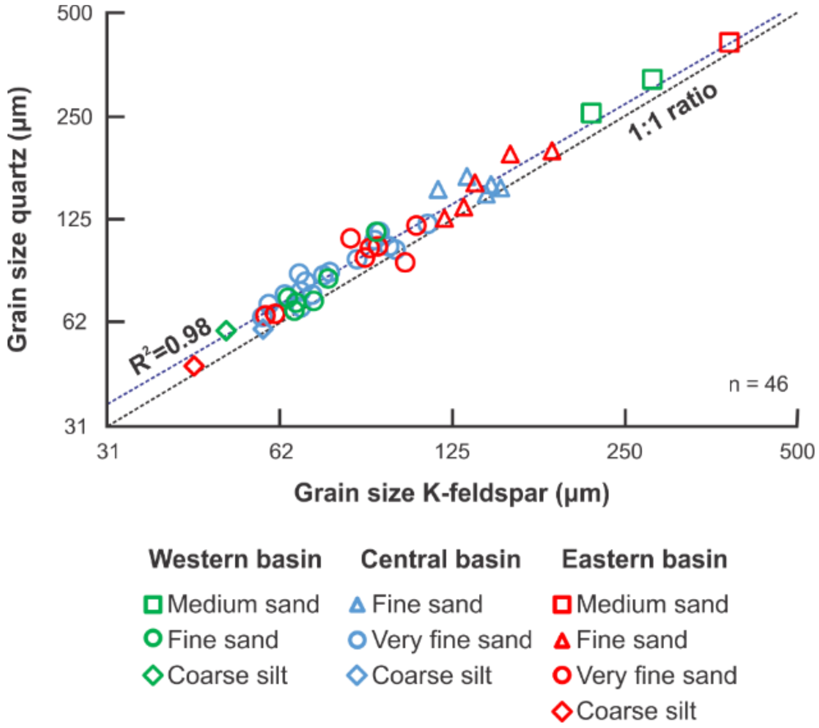

Figure 5.7: Plot of mean grain size quartz vs. mean grain size K-feldspar. The dashed black trendline represents a 1:1 ratio of quartz and K-feldspar grain size, while the dark blue trendline represents the linear regression correlation of quartz and K-feldspar grain sizes.

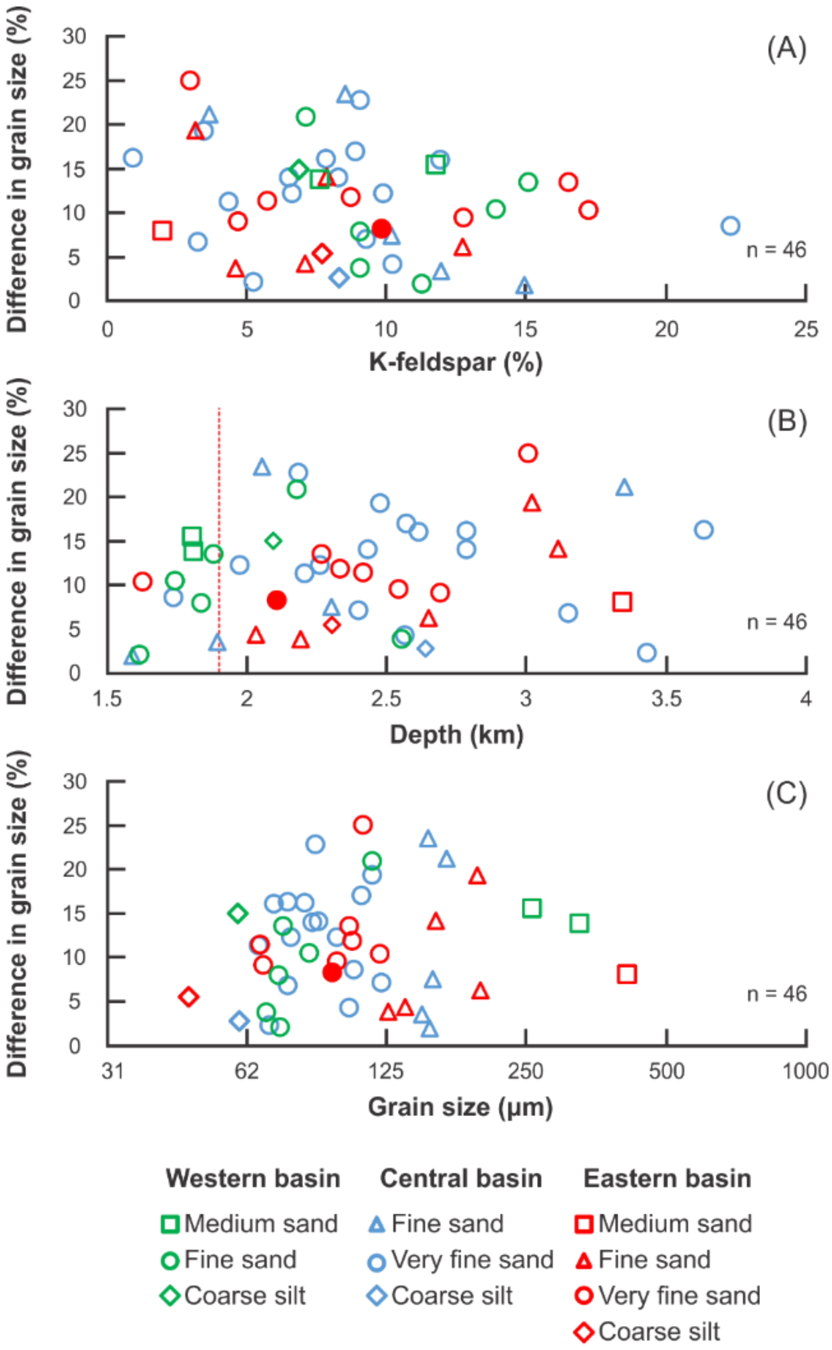

*Solid symbol indicates a K-feldspar grain size which is greater than quartz

Figure 5.8: Plot of difference between quartz and K-feldspar grain size vs. **A)** percent K-feldspar, **B)** sample depth (km), and **C)** mean grain size.

5.4.2 Model methodology and results

To predict areas where secondary porosity as a result of the breakdown of K-feldspar is most likely to occur, the distribution of feldspar within the study area has been modelled using DionisosFlow™. The resulting distribution is then be compared to temperature and structural maps of the basin to predict the distribution of both secondary porosity produced and preserved as a result of the breakdown of K-feldspar.

Feldspar distribution has been modelled using the reference case models of Sangster et al. (2019), which modelled the distribution of sand in the Scotian Basin. These reference case models have been modified to include sediment classes which represent feldspar grains. In order to simulate the distribution of K-feldspar in the study area during deposition, the observed K-feldspar abundances have been interpreted to reconstruct the original feldspar proportion. Lines of best fit for K-feldspar proportion have been generated for all three areas of the basin considering the composition of all sand sized samples (Fig. 5.9). Burial depths less than 1.9 km are considered to have largely unaltered feldspar, therefore, all sample depths above this depth have been translated to 1.9 km depth for the purpose of generating the lines of best fit to represent maximum values of supplied feldspar proportions. A forced intercept of 3.8 km has been used to represent the point of 0% K-feldspar based on observations from Pe-Piper and Yang (2014), who suggested that total K-feldspar dissolution begins to occur at around this depth in the area. The intercept of the trendlines at 1.9 km has been used to estimate the initial K-feldspar input for each of the three areas of the basin. The western basin intercepts at 11.8%, the central basin at 14.5%, and the eastern basin at 15.5% (Fig. 5.9).

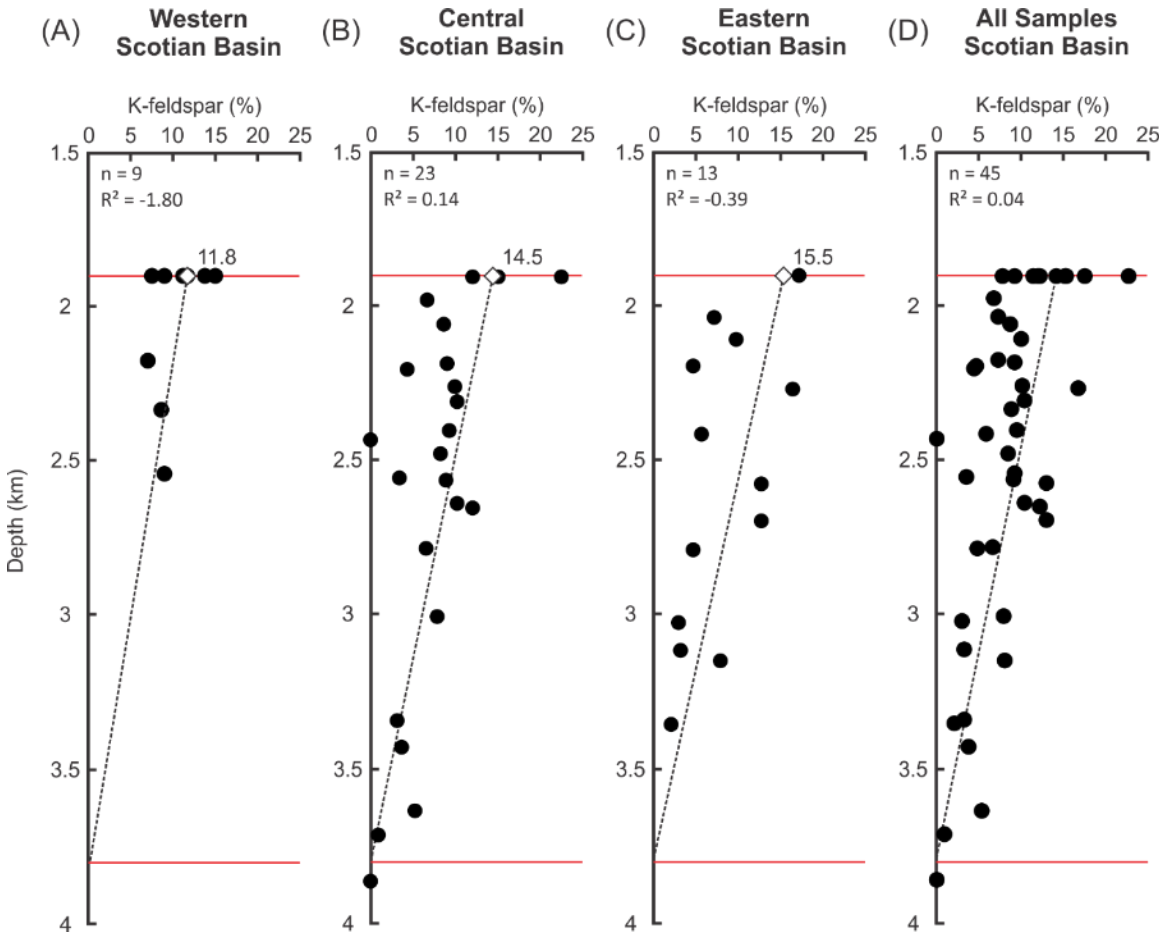

Figure 5.9: Plot of K-feldspar proportion (%) and sample depth (km). Samples are subdivided according to location in the basin. **A)** Western Scotian Basin, **B)** central Scotia Basin, and **C)** eastern Scotian Basin. Samples from depths of less than 1.9 km have been translated to a depth of 1.9 km. A trendline forced through 0% at 3.8 km has been generated and extended to 1.9 km depth to recreate the initial K-feldspar content of each part of the basin.

The sediment grain size in the "reference case models" ranges from clay to coarse sand size. The size distribution of K-feldspar that is used is based on the relationship between quartz and K-feldspar grain size observed in samples shallower than 1.9 km (Table 5.3). No coarse grained sands have been analysed in this study, in order to determine the appropriate grain size to simulate for this sediment fraction, a line of best fit for all samples has been used (Fig. 5.7). Only sand-rich samples have been analyzed as part of this study, as a result, feldspar proportions must be normalized to the sand proportion used in the reference case models, such that an input of 10% coarse sand with a predicted value of 11.8% K-feldspar should have a coarse K-feldspar model input of 1.18%. The resulting input K-feldspar proportions are accommodated in the reference case models by subtracting the K-feldspar input from the clay sized sediment fraction.

Table 5.3: Summary of simulated sediment classes from Sangster et al. (2019) and corresponding K-feldspar grain size values based on grain size analysis.

Grain Size Fraction	Mean Grainsize difference (%)	Grain Size (µm)	
		Qz	Kfs
Clay	-	40	-
Silt	-	60	-
Very fine sand	9	75	68
Fine sand	3	200	195
Medium sand	15	400	341
Coarse sand	-	650	576

Simulation results are presented in terms of (paleo) shelf, slope and basin. The shelf is the region proximal to the sediment input with a gradient of less than 1°, terminating at the shelf break. The slope is defined as having a simulated angle greater than 1°, and passes seawards into the basin, which is the area of less than 1° gradient seawards of the slope, extending to the edge of the study area. Results of simulations of K-feldspar distribution are displayed in two types of maps. The total K-feldspar proportion, relative to all simulated sediments (Fig. 5.10), shows trends of K-feldspar distribution in the study area that must be considered as semi-quantitative since the abundance of K-feldspar in shales has not been determined.

The maps of percentage of K-feldspar in sands (Fig. 5.11) were derived by normalizing the K-feldspar proportion maps to the sand proportion maps of Sangster et al. (2019). As the mean grain size and specific gravity of feldspar grains is a little less than quartz, modelling shows that feldspar is concentrated in more distal and finer grained sediments in the deep water basins. Sands at the edge of the simulated area show K-feldspar concentrations greater than 20% (Fig. 5.11), which is an artefact of the closed system that is modelled.

5.4.2.1 Upper Missisauga Formation

K-feldspar is most abundant on the shelf, ranging from 2–6%, with concentrations generally decreasing from east to west (Fig. 5.10A). The basin contains K-feldspar proportions ranging from 0–2% with the largest accumulations occurring in: corridors basinward of the Annapolis G-24 and Crimson F-81 wells; small basins in the western basin; and in a large accumulation basinward of the Tantallon M-41 well, all of which are areas of sand accumulation. When these proportions are considered as a ratio between sand and K-feldspar, an inverse relationship is observed. Simulations suggest that on the shelf, where sands are abundant, they show a feldspar proportion of 10–13%, which increases to 12–20% in the basin, where sands are less common (Fig. 5.11A). Sands in the east of the study area are generally more K-feldspar rich by 2–3% than those in the central and western areas.

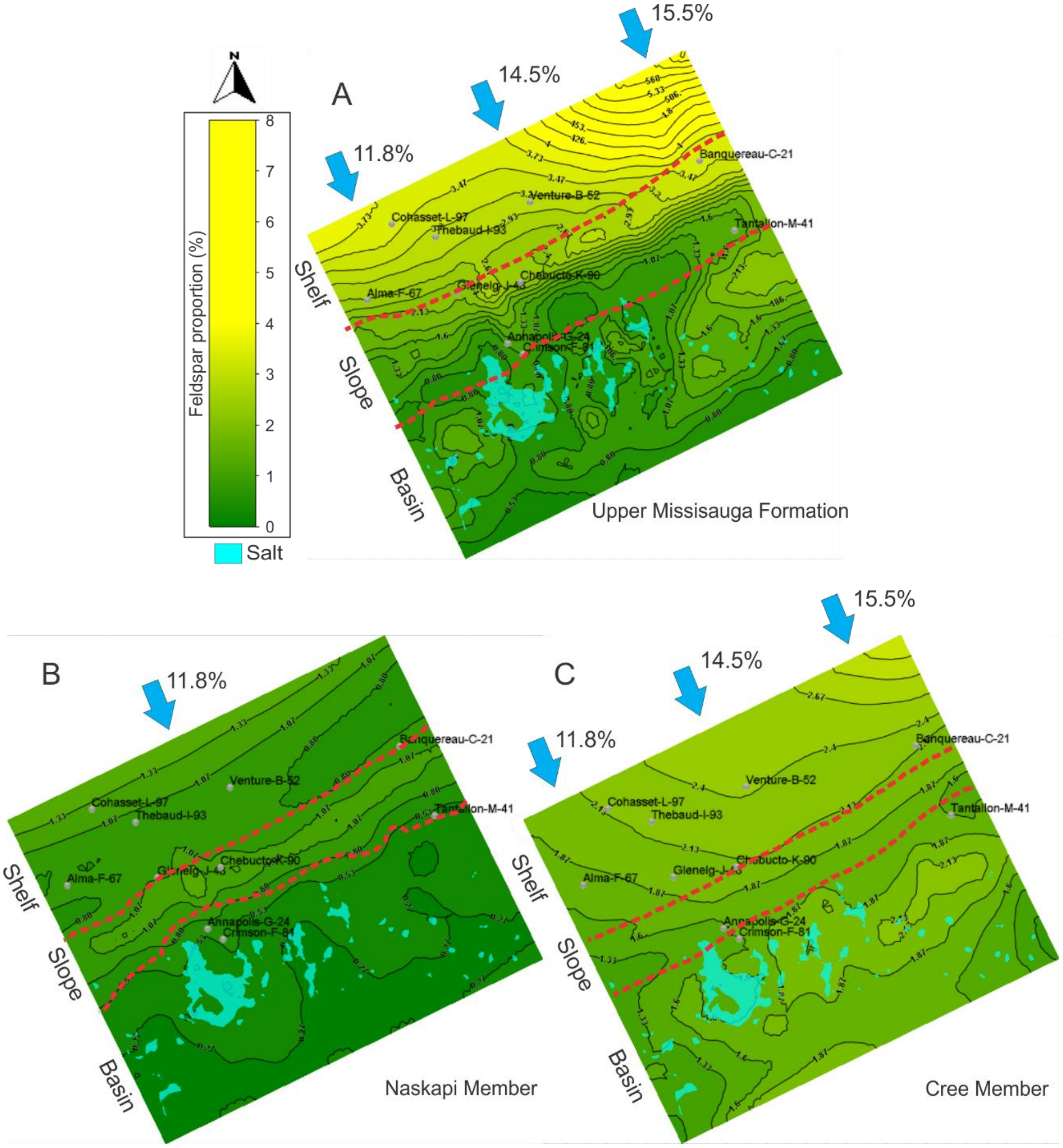

Figure 5.10: Weighted average simulated K-feldspar proportion maps for **A)** Upper Missisauga Formation, **B)** Naskapi Member, and **C)** Cree Member. Blue represents outline of main salt canopies (defined as areas with less than 200 m sediment thickness) and other structures in the distal areas. % inputs refer to input proportion of feldspar.

5.4.2.2 Naskapi Member

Feldspar concentrations in the Naskapi Member are the lowest of the three units observed in this study reflecting the low amount of sand in this unit (Chavez et al., 2018). Concentrations range from 1–2% on the shelf diminishing to 0–1% in the basin (Fig.

5.10B). The largest accumulations are observed on the slope, where K-feldspar proportions are as high as 2%. K-feldspar proportions in sand range from 10–11% on the shelf and 10–20% in the basin (Fig. 5.11B).

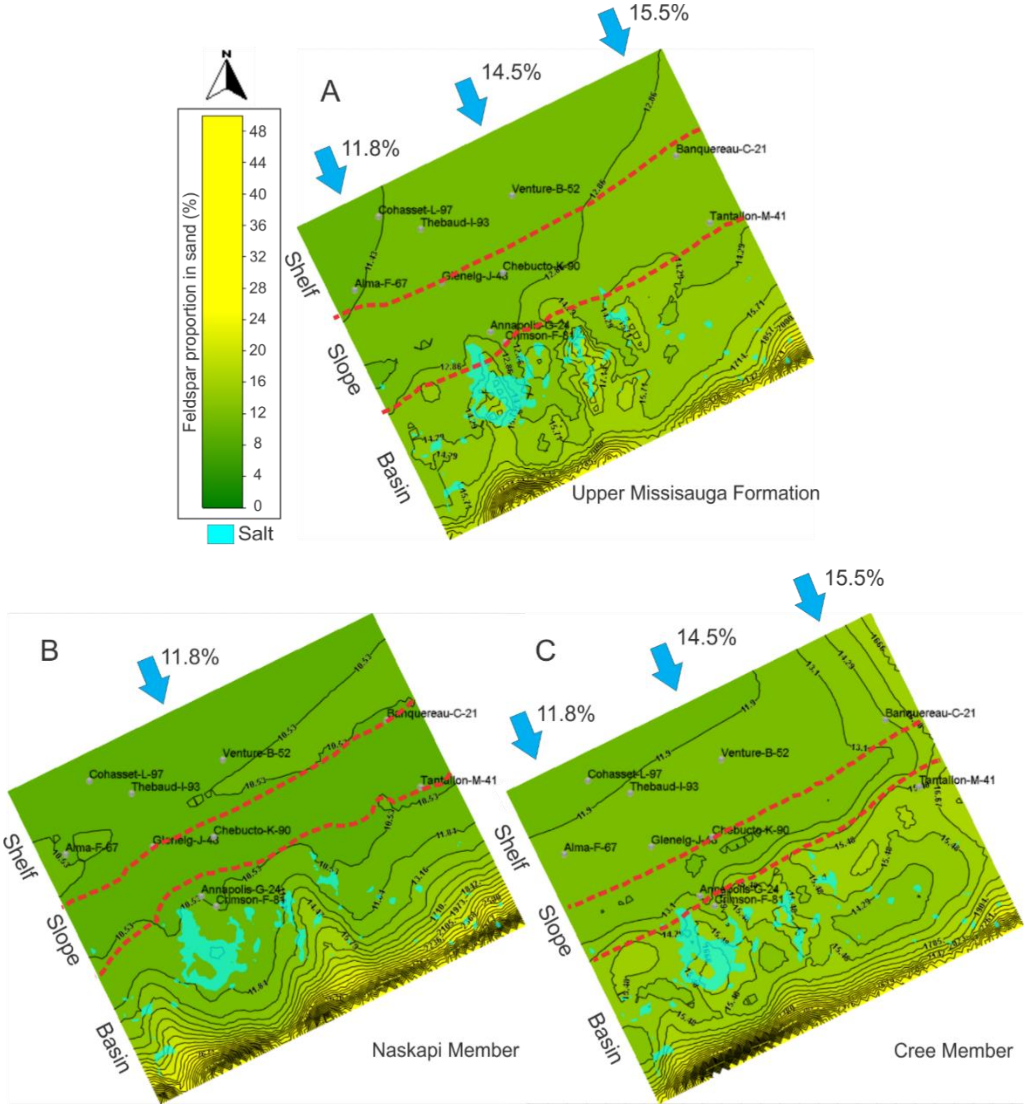

Figure 5.11: K-feldspar proportion normalized to sand proportion maps for **A)** Upper Missisauga Formation, **B)** Naskapi Member, and **C)** Cree Member. Blue represents outline of main salt canopies (defined as areas with less than 200 m sediment thickness) and other structures in the distal areas. % inputs (blue arrows) refer to input proportion of feldspar.

5.4.2.3 Cree Member

K-feldspar proportions in the Cree Member follow a similar trend as in the Upper Missisauga Formation, although proportions are generally lower (Fig. 5.10C). Proportions decrease from east to west on the shelf, ranging from 2–3%. In the basin K-feldspar proportions range from 1–2%. Sands on the shelf show K-feldspar proportion ranging from 11–17%, with the highest proportions on the shelf found in the eastern study area (Fig. 5.11C). K-feldspar content generally increases in the basin, with proportions ranging from 13–17%.

5.5 Discussion

5.5.1 Controls on K-feldspar abundance

5.5.1.1 Influence of provenance

Samples taken from the central and eastern basin show similar mean K-feldspar proportions and follow similar trends with depth, while the western basin shows a greater mean K-feldspar proportion (Fig 5.4). This suggests that there is a provenance related influence on K-feldspar distribution laterally in the basin. However, all areas of the basin follow a similar trend of declining K-feldspar content with depth. Whereas the western basin does not contain any samples analyzed from below 2541 m burial depth, samples above this depth share similar values with the other areas of the basin, suggesting that this part of this basin experienced a similar process to that of the rest of the basin (Table 5.2; Fig. 5.5). Provenance studies conducted in the region (Piper et al., 2012; Pe-Piper et al., 2014; Zhang et al., 2014) suggest that catchment areas remained largely unchanged throughout the Early Cretaceous. Therefore, the observed stratigraphic trends in feldspar proportion are not likely related to changes in sediment provenance. The exception was during the Naskapi Member deposition, when the Sable and Banquereau rivers were diverted as a result of volcanism and uplift along their flow path (Bowman et al., 2012; Chavez et al., 2018; Sangster et al., 2019). During this time the Meguma Terrane was the source of new sediment to the Scotian Basin (Chavez et al., 2018). Naskapi Member samples do not show significant differences in proportion compared to other stratigraphic units (Figs 5.5&5.9).

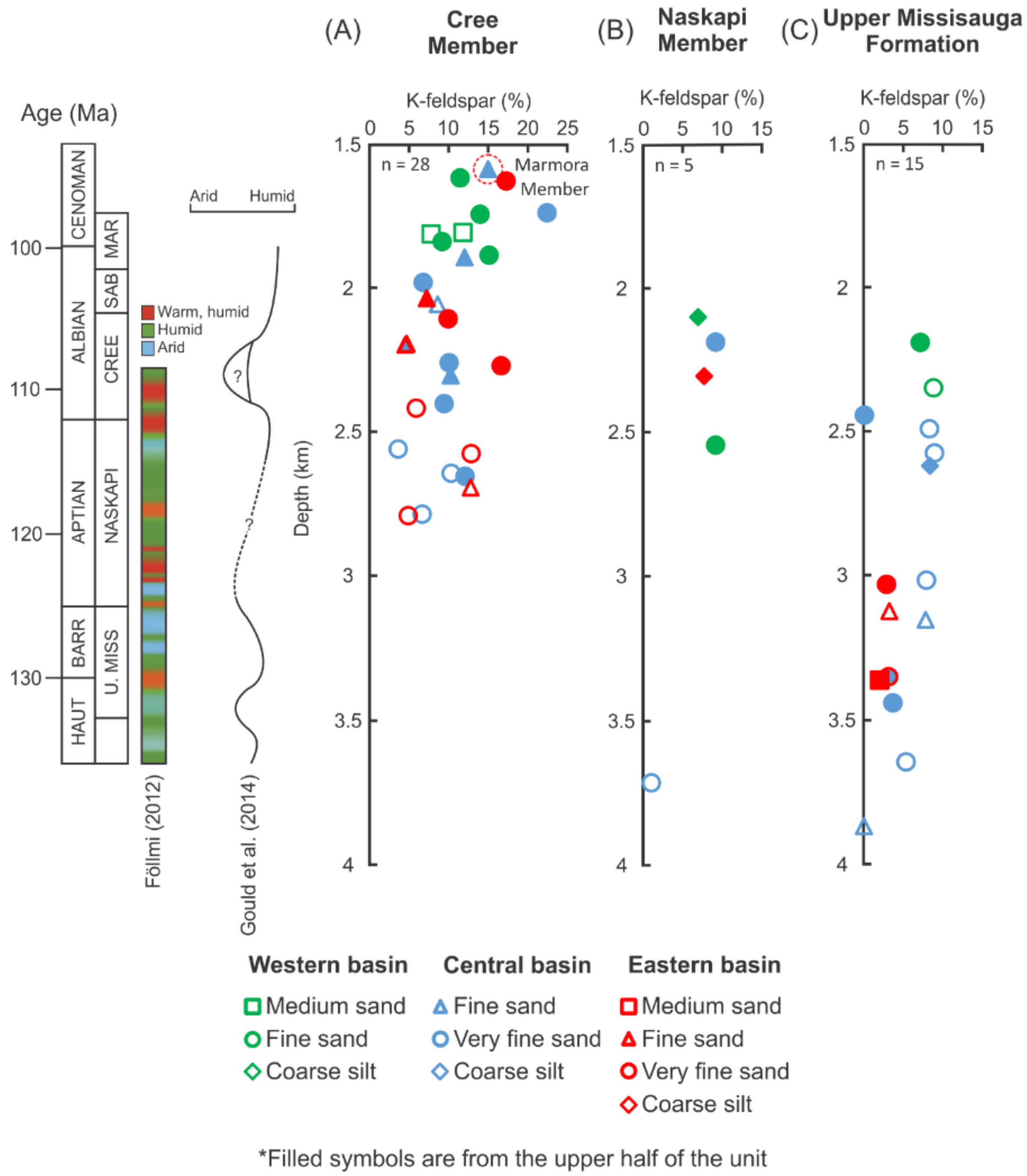

Figure 5.12: Plot of K-feldspar proportion (%) and sample depth (km). Samples are subdivided by unit into **A)** Cree Member, **B)** Naskapi Member, and **C)** Upper Missisauga Formation. Samples have been further subdivided by position within each unit, such that samples from the upper half of each unit are represented by a filled symbol.

5.5.1.2 Influence of climate

Climate is an important factor in determining the types of sediment which are supplied to a region, with more humid climates associated with an increased supply of clays as a result of increased chemical weathering. As a result of its chemical composition, K-feldspar is highly susceptible to chemical weathering, and as a result, should be present in lower quantities in sediments derived from catchment areas with more humid climates (Ruffell and Batten, 1990; Ruffell and Worden, 2000; Gould et al., 2014). Paleoclimate studies of the Scotian Basin based on illite/kaolinite ratios suggest that climate fluctuated on a variety of time scales from arid to humid in the Early Cretaceous (Gould et al., 2014; Chavez et al., 2016). During the Barremian, climate was initially humid, becoming arid by the Aptian and returning to a humid climate by the Albian (Gould et al., 2014; Chavez et al., 2016). The Albian shows a transition from a dominantly arid climate transitioning to humid by the Cenomanian (Gould et al., 2014). Samples have been assigned to either the upper or lower half of each unit to observe if there is a correlation between climate and sediment composition (Fig. 5.12). Samples from the lower half of the Cree Member show a lower mean K-feldspar content than the upper half (Fig. 5.12A), however, the upper half of this formation is interpreted to have a more humid climate than the lower half (Gould et al., 2014). The same inverse relation is observed in the Upper Missisauga Formation (Fig. 5.12C). Only a single sample was sourced from the arid interval of the Naskapi Member, however the same inverse relationship is observed (Fig. 5.12B). These results suggest that if climate influences the proportion of K-feldspar, its influence is masked by other factors.

5.5.1.3 Influence of burial and diagenesis

Given that there does not appear to be evidence of a major shift in the source areas which supplied the Scotian Basin, except in the Naskapi Member, and the counter-intuitive relationship between inferred climatic shifts in the source areas and the measured K-feldspar proportion, the decrease in K-feldspar proportion with depth is likely related to diagenetic processes. The major processes responsible for the breakdown of K-feldspars during burial are related to the interaction of grains with organic acids and carbon dioxide, and to water-rock interactions (Taylor et al., 2010). The production of acids and carbon dioxide are related to the maturation of organic material during burial. Carbon dioxide in fluid inclusions from the Venture field (Karim et al., 2011) implies up-dip supply of carbon dioxide from deeper parts in the basin. However, given the large scale at which feldspar dissolution is observed, it is unlikely that sufficient acids could be produced in a natural system to generate all of the observed dissolution (Taylor et al., 2010). Studies conducted on the breakdown of K-feldspar and other aluminosilicate minerals suggest that while decomposition is greatest under strongly acidic and strongly alkaline conditions, such extremes are not required to decompose these minerals (Giles and de Boer, 1990). Rather, the reaction is controlled by temperature which increases with burial such that the rate of K-feldspar breakdown increases exponentially with increased heat (Giles and de Boer, 1990). The onset of K-feldspar dissolution has been reported to occur at temperatures as low as 57°C to as high as 125°C based on modern geothermal gradients (Wilkinson et al., 2001). In the Scotian Basin, the modern geothermal gradient is 25°C/km (Issler, 1984). However, a geothermal as high as 55°C/km, based on homogenization temperatures in primary fluid inclusions in quartz overgrowths and strongly negative $\delta^{13}C$ values in carbonate cements, was present during the Aptian-Albian times (Karim et al., 2012). This elevated geothermal gradient was related to enhanced heat flow to the basin during the Aptian-Albian (Bowman et al., 2012; Karim et al., 2012).

Dissolution of K-feldspar, where no by-products are precipitated, can be expressed using the following reaction from Giles and de Boer (1990):

$$KAlSi_3O_8 + 4H^+ \rightarrow Al^{3+} + 3SiO_{2\,(aq)} + K^+ + 2H_2O$$

When pore waters become saturated in Al^{3+} and $SiO_{2\,(aq)}$, normally kaolinite and quartz precipitate (Giles and de Boer, 1990; Bjørlykke and Jahren, 2012). Illite precipitates in conditions of high temperatures (>125°C) and high K/H activity ratios (aK^+/aH^+) (Bjørlykke, 1998; Lanson et al., 2002; Franks and Zwingmann, 2010). Formation of these clay mineral by-products can be reduced or prevented if dissolution occurs in an open system in which porewaters are removed from the system (Yuan et al., 2014).

K-feldspar grains commonly undergo albitization, in which grains are replaced by albite via a 1:1 exchange of Na^+ for K^+ (Walker, 1984). This process has been shown to be highly dependant on the removal of K^+ from pore waters in addition to a supply of Na^+ (Aagaard et al., 1990). The most effective means of K^+ removal from solution is related to the illitization of clays, such as smectite at temperatures between 70 and 80°C (Aagaard et al., 1990), and kaolinite from 100–130°C (Saigal et al., 1988). In these cases, Na^+ is thought to have been supplied from the illitization of smectite (Saigal et al., 1988), the dissolution of intraformational sodium-rich plagioclase (Walker, 1988), or circulating saline brines (González-Acebrón et al., 2010). In the Scotian Basin, smectite to illite conversion begins at 1.5–2 km and is complete by 4 km (Pe-Piper, 2016), and circulating saline brines, derived from the Argo salt formation, predominate in the Scotian Basin (Karim et al., 2012; Pe-Piper et al., 2015). At temperature below 145°C, the speed at which albite forms in response to the dissolution of K-feldspar is slower than the rate of dissolution (Saigal et al., 1988), and as a result minor secondary porosity is produced.

The breakdown of K-feldspar grains has been shown to occur at a variety of depths, and three general styles have been reported in the literature. **1)** Systems which generate dominantly clay minerals, such kaolinite and illite, have been shown to form at depths as shallow as 1.7 km in Miocene sandstones of the Far East (Giles and de Boer, 1990), 1.5–4.5 km in the Bohai Bay of East China (Yuan et al., 2015); and 3.6–3.7 km in the Haltenbanken area of Norway (Chuhan et al., 2001). **2)** Systems with clay minerals and substantial secondary porosity, form at 2.5–4 km in the Bohai Bay of East China (Yuan et al., 2015); and from 3–4.5 km in the central graben of the North Sea (Haszeldine et al., 1999). **3)** Albitization of K-feldspar has been shown to occur at depths between 2.1 and 3.2 km in the Cameros Basin Spain (Gonzales-Acebron et al., 2010); offshore Norway, initially along planes of weakness from 2.2–3 km and complete pseudomorphing of K-feldspar grains below 3.5 km (Saigal et al, 1988); and at depths greater than 3.3 km in the Fountain Formation, of Colorado USA (Walker, 1984). The wide range of depths which are present in these systems suggest that there is no systematic method, based on burial depth, which can be used to predict the breakdown products of feldspar dissolution. The presence of clay minerals, albite, and secondary porosity are the result of local variables such as pore water chemistry, and mechanisms for fluid removal related to regional geological processes.

In the Scotian Basin, evidence of albitization is first found at approximately 1.9 km burial depth, persisting until 3 km, with complete dissolution of K-feldspar occurring at 3.8–4.5 km (Pe-Piper and Yang, 2014). K-feldspar concentrations in this study appear to decrease at burial depths less than 1.9 km trending towards 0% K-feldspar below 3.8 km (Fig. 5.5). This suggests that K-feldspar grains in the Scotian Basin have experienced extensive dissolution below 1.9 km burial depth, with samples above this depth experiencing minimal alteration and dissolution.

Most samples analyzed in this study are taken from wells located on the shelf, with shallow water depths of generally less than 100 m. The ability to predict K-feldspar stability with burial is not greatly influenced by the datum used to describe their depth in these wells. In order to confirm that a below-sea-floor datum is a more accurate datum to predict K-feldspar dissolution, samples from the Newburn H-23 well, which has a water depth of 977m, have been considered. K-feldspar proportions, based on conventional point counting (Sangster, 2016), suggest that ~3% K-feldspar are present at measured (RT) depths of 4.3–4.4 km, dropping to 0% below 4.4 km. These concentrations suggest that K-feldspar commonly persists at depths greater than 3.8 km. However, when sample depth below sea floor bottom is considered, these samples are located at approximately 3.4 km depth. These values follow trends present in the shelf wells (Table 5.2), suggesting that a below-sea-floor datum is appropriate to predict feldspar distribution in the basin.

Samples analyzed in this study are dominantly polished smear slides, and as a result, the authigenic clay content could not be determined as the original textures have not been preserved. The extent to which secondary clay minerals vary with depth therefore cannot be commented on.

5.5.1.4 Variation with grain size

Given the tendency of feldspars to be comminuted at a more rapid rate than quartz during transport, both as a result of physical properties such as relatively lesser hardness and abundant cleavage, and chemical properties, namely a greater susceptibility to chemical weathering, there is the potential for K-feldspar to concentrate in finer sediment fractions (Odom et al., 1976). Plots of mean grain size and mineral proportions determined by Blatt et al. (1972) suggest that feldspar relative abundance is greatest in the fine sand fraction. Additional research shows that sediments deposited in highly agitated environments, or which have been derived from pre-existing sedimentary sources, tend to have a grain-size-dependant feldspar proportion (Odom et al., 1976). However, other authors such as Nesbitt and Young (1996), have found that grain size has little impact on feldspar proportion.

A comparison of mean grain size of quartz and the proportion of K-feldspar (Fig. 5.6) suggests that the very fine sand fraction contains the highest K-feldspar proportion in the study area. However, if only samples from sample depths of less than 1.9 km are considered, at which depth minimal dissolution or alteration has occurred in the K-feldspar grains (Pe-Piper and Yang, 2014), the mean proportions are similar in all sediment classes, despite the very fine sand fraction still showing the greatest proportions of K-feldspar (Fig. 5.6). This suggests that K-feldspar proportion is not related to mean grain size in the study area.

5.5.1.5 Grain size shift

Grain-size measurements of samples collected as part of this study show that all but one sample have a larger mean quartz grain size than K-feldspar (Fig. 5.7), with K-feldspar grains being an average of 11% smaller than the mean quartz grain size (Fig. 5.8A). Settling equivalency analysis based on Stokes law, considering grain size, shape, and density, suggests that minerals of lesser density tend to be associated with smaller grains of higher density minerals (Garzanti et al., 2008). Discrepancies may be related to limited availability of grain sizes (due to recycling, abrasion due to easy cleavage). Sandstones have been documented to have feldspar grain sizes which are smaller than their associated quartz grain sizes, with silt sized feldspar grains in samples containing fine-medium grained quartz (Odom et al., 1976). This process is thought to be related to initially fine-grained feldspar in the source area in combination with continued abrasion during transport.

K-feldspar grains have been shown to have been sourced largely from the Grenville Province (Tyrrell et al., 2014; Blowick et al., 2018), which is located over 600 km from the Scotian Basin. This great transport distance may have provided sufficient mechanical abrasion during transport to comminute feldspar grains. Additionally, while the grain size difference does not show a strong trend with depth (Fig. 5.8A), a trend of increased difference with decreasing feldspar proportion is observed (Fig. 5.8A). This increase suggests that K-feldspar grain size has been modified by diagenesis during burial. However, samples from burial depths less than 1.9 km still show a mean grain size shift of ~10%, suggesting that transport processes were likely at play as well.

5.5.2 K-feldspar distribution model

5.5.2.1 K-feldspar distribution

K-feldspar trends observed in these simulations generally follow trends observed in the reference case models (Sangster et al., 2019), with feldspar dominantly trapped on the shelf with a general decrease from east to west in the Upper Missisauga Formation and Cree Member, and trapped dominantly along the slope in the Naskapi Member. Transport to the basin occurred along salt-tectonics-related corridors and deposited in minibasins along the slope and basin. However, as a result of the smaller grain sizes used in addition to the lower density of K-feldspar, these grains are transported further into the basin than their coarser quartz sand equivalents. As a result, while total sediments are enriched in K-feldspar on the shelf compared to the basin (Fig. 5.10), K-feldspar proportions are greater in sands in the basin, typically by 2–3%, but can be as much as 10% greater (Fig. 5.11) compared to sands on the shelf. This suggests that sand-rich intervals at greater paleodepths in the basin have the greatest potential contribution to reservoir quality through the formation of secondary porosity. However, the largest concentrations of K-feldspar in the study area are in distal regions with lower sand content, such as around salt withdrawal corridors, basinward of sand rich mini-basins, and near salt bodies. As a result, while the basinal sands are associated with generally higher K-feldspar proportions, they form smaller reservoir intervals overall than on the shelf.

The presence of high concentrations of feldspar relative to sand (Fig. 5.11) at the edge of the simulated area suggests that, much like total sands in the basin (Sangster et al., 2019), feldspar has a high potential to by-pass the modelled area into deeper parts of the basin. Sands transported to water depths >3000 m seaward of the modelled area may have viable secondary porosity.

5.5.2.2 Evaluation of risks on reservoir quality

Risk maps indicate regions of a basin which are most likely to have high quality petroleum play elements: reservoir, source, maturity, and seal (Grant et al., 1996). The risk of each element is evaluated individually using common risk segment (CRS) maps. This study evaluates the risk on reservoir quality based on the dissolution of K-feldspar during diagenesis and the distribution of sand rich intervals which form reservoir intervals. Areas of low risk indicate the highest probability of encountering high quality reservoir.

5.5.2.2.1 Predicting the generation of secondary porosity from feldspar dissolution

K-feldspar in the central Scotian Basin has been shown to breakdown with increased depth (Fig. 5.5). Due to the strong association of depth with temperature, burial depths of the sample collected in this study have been converted to temperature on the basis of a modern geothermal gradient of 26.6°C/km burial depth, with a sea bottom temperature of 11.8°C (Issler, 1984). This conversion suggests that K-feldspar dissolution begins to occur when exposed to temperatures of 62.3°C, and is complete at greater than 112.9°C. This process occurs at a rate of approximately 2% total volume of K-feldspar/°C. In order to quantify the breakdown of K-feldspar in sand rich intervals, this rate is applied to feldspar distribution maps (Fig. 5.11) using thermal modelling conducted in the study area (OERA, 2016).

The generation of secondary porosity increases with age (Fig. 5.13) and is most prevalent along the slope of the study area. In the Upper Missisauga Formation (Fig. 5.13A) shelf values range from 5–13% secondary porosity increasing towards the slope, with large regions of secondary porosity located in the eastern and central slope (>12%), and at the toe of the slope leading into the basin along salt withdrawal corridors. There is a large region of secondary porosity located at the edge of the study area, where feldspar has been suggested to accumulate (Fig. 5.11). In the basin, where sand bodies are predicted for the Upper Missisauga Formation, sand bodies in the eastern and central study area show 5–10% secondary porosity, the sand body with the largest secondary porosity is located in the western basin, with values greater than 13% in the shelfward half of the body (Fig. 5.13A). In the Naskapi Member, where sand is less prevalent, secondary porosity follows a similar trend as the Upper Missisauga Formation, although they are 40–50% lower on the shelf, 10–40% lower on the slope, and 50–90% lower in the basin (Fig. 5.13B). In the Cree Member secondary porosity generation on the shelf ranges from 1–12% with the largest generation occurring in the western shelf at the transition to the slope (Fig 5.13C). Trends in the slope and basin are similar to the Upper Missisauga Formation, with values ranging from 2–13% and 1–13% respectively. Sand bodies predicted in the basin show generally lower secondary porosity where thermal modelling is available, with the greatest secondary porosity predicted in the large body located in the eastern-central basin at <12%.

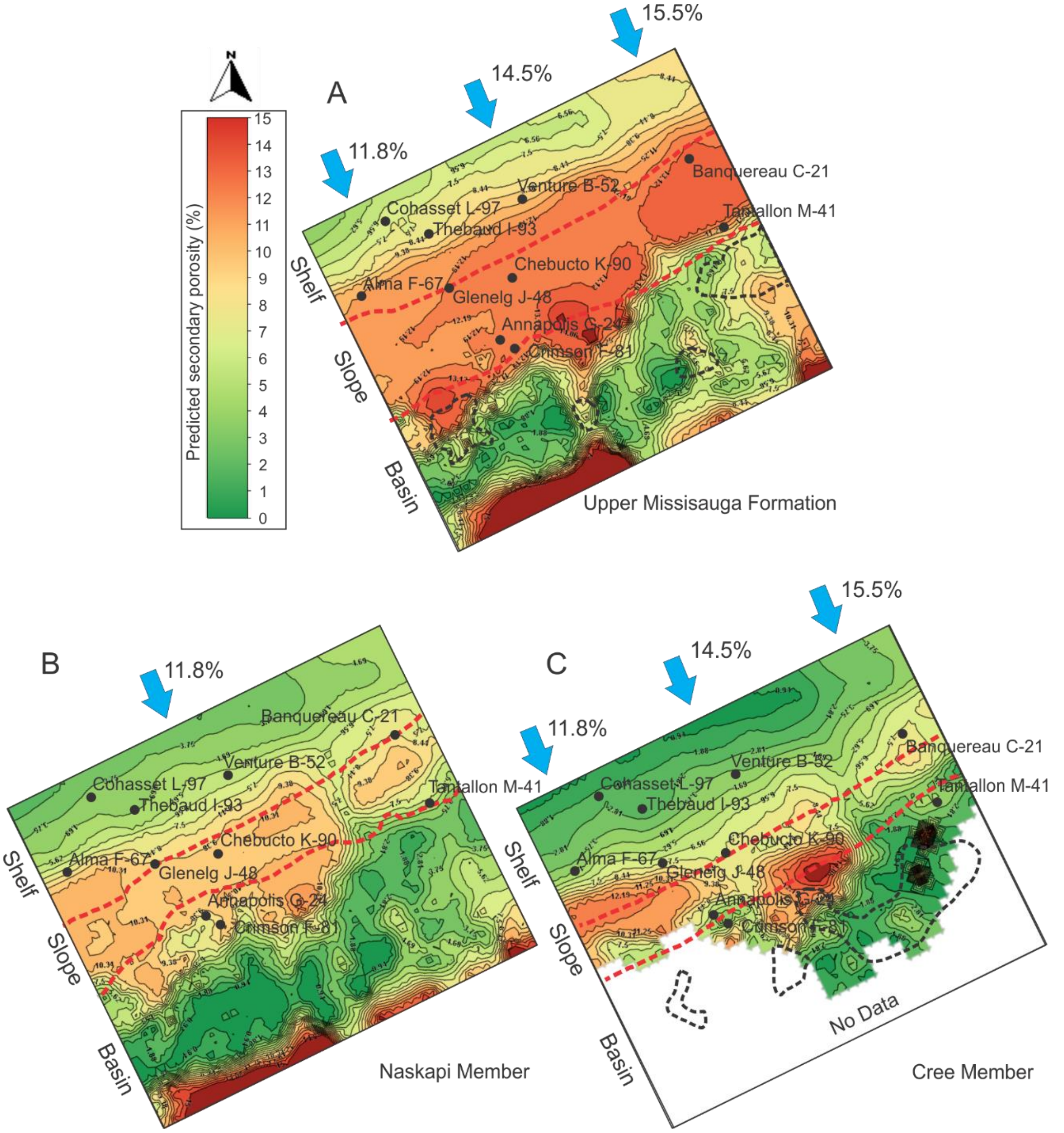

Figure 5.13: Predictive maps of secondary porosity from the dissolution of K-feldspar with temperature, based on a comparison of feldspar distribution (Fig. 5.11) and thermal modelling (OERA, 2016) for **A)** Upper Missisauga Formation, **B)** Naskapi Member, and **C)** Cree Member. Dashed black lines indicate sand rich bodies predicted in Sangster et al. (2019). % inputs (blue arrows) refer to input proportion of feldspar.

5.5.2.2.2 Open vs closed system

While the breakdown of K-feldspar is largely related to burial depth, the preservation of the generated secondary porosity is controlled by the ability of breakdown products to be removed from the system. Closed systems, in which fluids are unable to circulate, quickly become saturated in K^+ and Al^{3+}, resulting in the authigenesis of clays and limited formation of secondary porosity. Conversely, open systems allow for the removal of these products and the preservation of secondary porosity and permeability, as has been demonstrated recently by Yuan et al. (2015) in the Bohai Basin, East China.

Fault mapping of the study area (OETR, 2011) has been used to predict areas of the basin which likely acted as an open system, allowing for circulating basinal fluids to preserve secondary porosity (Fig. 5.14). The mobilization of the Upper Triassic-Lower Jurassic Argo salt formation resulted in abundant faulting in the central Scotian Basin (Deptuck et al., 2009; Kendell, 2012), which allowed for saline formation waters to be transported along detachment faults, down-to-basin listric faults, and permeable sandstones (Pe-Piper et al., 2015). As a result, faulting within the basin has a high potential to remove the by-products of K-feldspar dissolution and thus to preserve secondary porosity. Faults in the study area generally cut through the K101 and K130 surfaces down to the underlying salt or salt welds (OETR, 2011). Additionally, studies of the lithofacies of the Scotian Basin have concluded that lithofacies associated with fluvial-esturine channels and river mouth turbidites showed the greatest permeability (Zhang et al., 2015), and may have served as pathways for fluid circulation on the shelf.

Faults in the central basin (Fig. 5.14) are more abundant than in the eastern basin (OETR, 2011; Fig. 5.14) and lithofacies associated with high permeability reservoirs are also generally thicker in the central basin than in the eastern basin (Gould et al., 2011). Additionally, samples with high permeability are more common in the central basin for both the Cree Member and Upper Missisauga Formation (Zhang et al., 2015).

On the basis of presence of faulting, lithofacies, and measured permeability, which contribute to the formation of an open system, the region of high faulting present in the central basin (Fig. 5.14; I) is more likely to preserve secondary porosity, and is therefore the area with the lowest risk in the study area for this factor. Preserved secondary porosity in the region is predicted to range from 7–13% in the Upper Missisauga Formation and 5–12% in the Cree Member (Fig. 5.13A and C), however, given the high temperature of basinal fluids which are likely to have been transported along the faults present in this region, complete dissolution of feldspar may have occurred resulting in 13% secondary porosity being generated and preserved. The next lowest risk is associated with the faulted region of the eastern basin (Fig. 5.14; II). Where faulting is less frequent in the east, thinner high permeability reservoir units are also present limiting additional removal of the breakdown products of feldspar dissolution. A moderate risk is therefore assigned to this zone. Secondary porosity in this region is predicted to range from 10–13% in the Upper Missisauga Formation and 5–10% in the Cree Member (Fig. 5.13A and C), with the potential for approximately 13% secondary porosity preservation as a result of enhanced heat flow related to circulating fluids along faulting. The remainder of the study area, where closed system conditions prevail, is considered to be a high risk for the preservation of secondary porosity generated from feldspar dissolution.

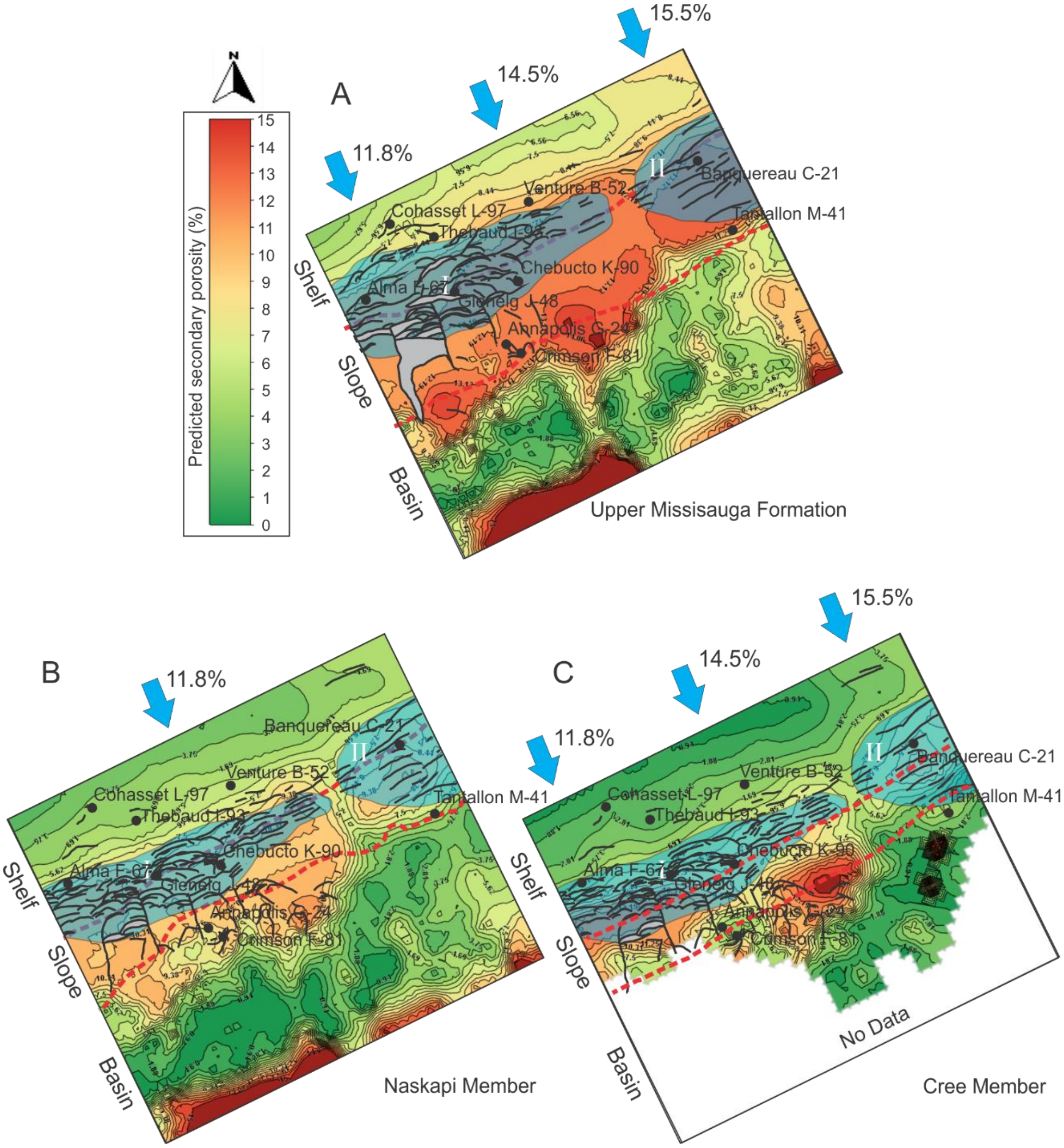

Figure 5.14: Risk fields overlain on fault maps (OETR, 2011) and maps of predicted secondary porosity (Fig. 5.13) for **A)** Upper Missisauga Formation, **B)** Naskapi Member, and **C)** Cree Member. I denotes the region with the lowest risk in the study area, followed by II with a moderate risk, and the remainder of the basin with the greatest risk. Dashed black lines indicate sand rich bodies identified in Sangster et al. (2019). % inputs (blue arrows) refer to input proportion of feldspar.

5.5.2.2.3 Common risk segment maps based on the distribution of sand, K-feldspar, and secondary porosity

To determine zones of the study area which present a reduced risk to exploration, maps of sand distribution from previous modelling (Sangster et al., 2019), predicted secondary porosity generation from the dissolution of feldspar (Fig. 5.11), and likely secondary porosity preservation (Fig. 5.13) have been used. Due to the small sand content of the Naskapi Member, and therefore low reservoir potential, risk maps have only been produced for the Cree Member (Fig. 5.15) and the Upper Missisauga Formation (Fig. 5.16). CRS maps are produced by assigning risk to each of the component maps on the basis of criteria presented in Table 5.4. A point value of three is assigned to regions of low risk, two points to moderate risk, and one to high risk regions. The CRS map is generated by adding together the point values of all the maps and assigning risk on the basis of the totals, with low risk assigned to values of 8–9, moderate to 6–8, and high risk to 3–6 (Figs. 5.15D and 5.16D).

Table 5.4: Criteria for risk level of component maps.

Risk type	Risk level		
	High	Moderate	Low
Sand distribution (Cree Member)	<10%	10-16%	>16%
Sand distribution (Upper Missisauga Formation)	<9%	9-18%	>18%
Secondary porosity	<5%	5-10%	>10%
Preservation of secondary porosity	other	II	I
Total risk	3-6 points	6-8 points	8-9 points

*Sand distribution from Sangster et al. (2019); Secondary porosity values from Fig. 5.13; Preservation of secondary porosity from Fig. 5.14. Results shown in Figs. 5.15 and 5.16

Regions of low risk appear to be present in the Cree Member in the central and western study area along the shelf edge and slope (Fig. 5.15D), with moderate risk associated with the shelf edge and upper slope running from east to west. In the basin, the lowest predicted risk is at the toe of the slope in the central study area with a moderate risk. The Upper Missisauga Formation shows greater areas of low risk, which are located at the shelf edge and upper slope (Fig. 5.16D). The shelf shows greater areas of moderate risk, with some minor regions of moderate risk present in the basin, largely as a result of increased generation of secondary porosity during this time (Fig. 5.16B).

Sand deposits on the shelf and slope have a lower risk than those in the basin identified in Sangster et al. (2019), particularly in the Upper Missisauga Formation which experienced greater temperatures on the shelf. Similarly, even though sands which are rich in K-feldspar may have been transported into the deep basin, they are likely poor in preserved secondary porosity as a result of lacking a system capable of removing the breakdown products from the dissolution of K-feldspar, and as a result present a high risk to exploration. As a result risk is lowest along the shelf edge and upper slope, particularly in the central and western study area. The lowest risk in the basin is located near the slope to basin transition (Figs. 5.15 and 5.16).

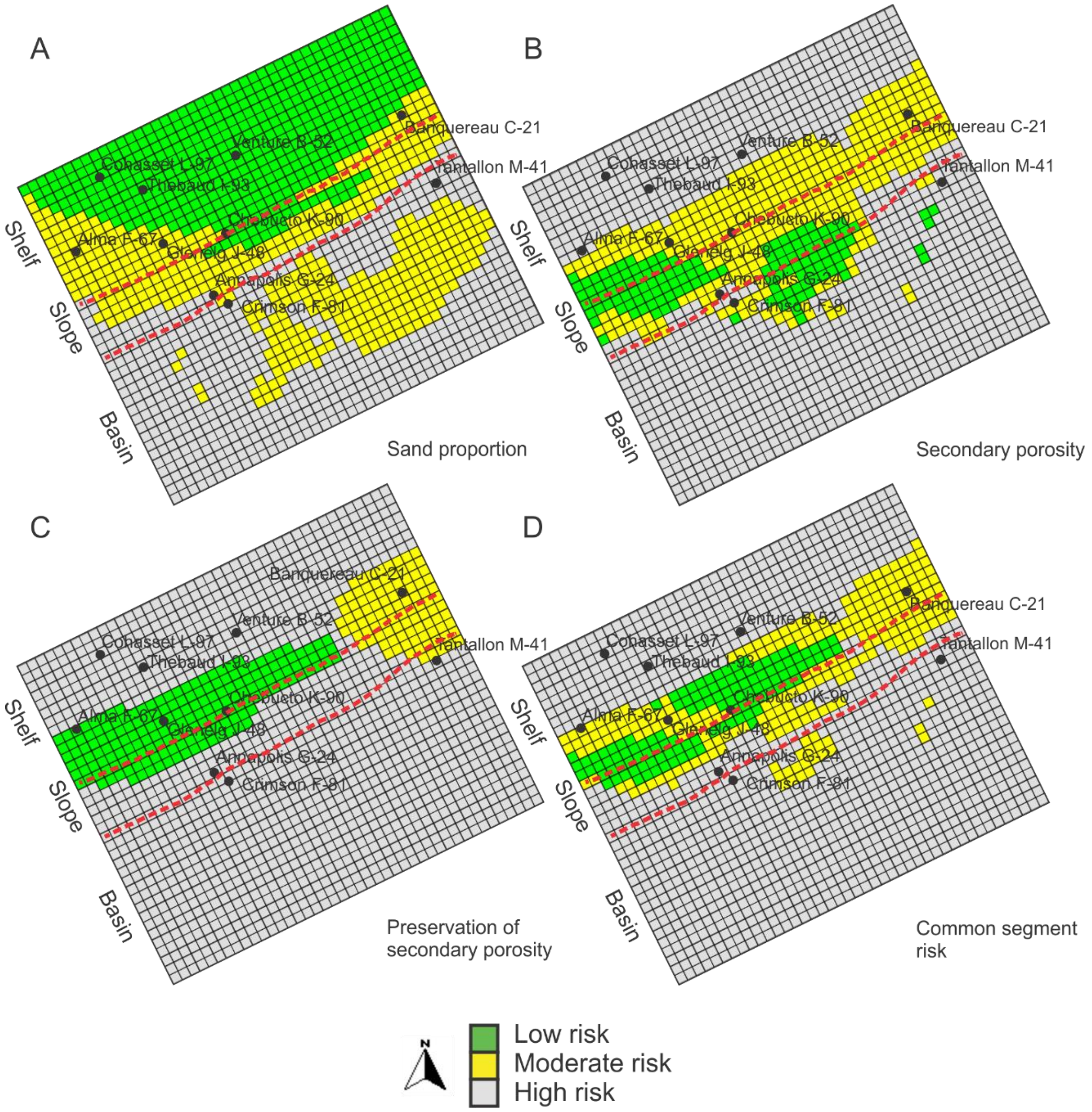

Figure 5.15: Risk maps for the Cree Member, showing component maps for **A)** sand distribution (Sangster et al., 2019), **B)** secondary porosity, **C)** preservation of secondary porosity, and **D)** common segment risk maps.

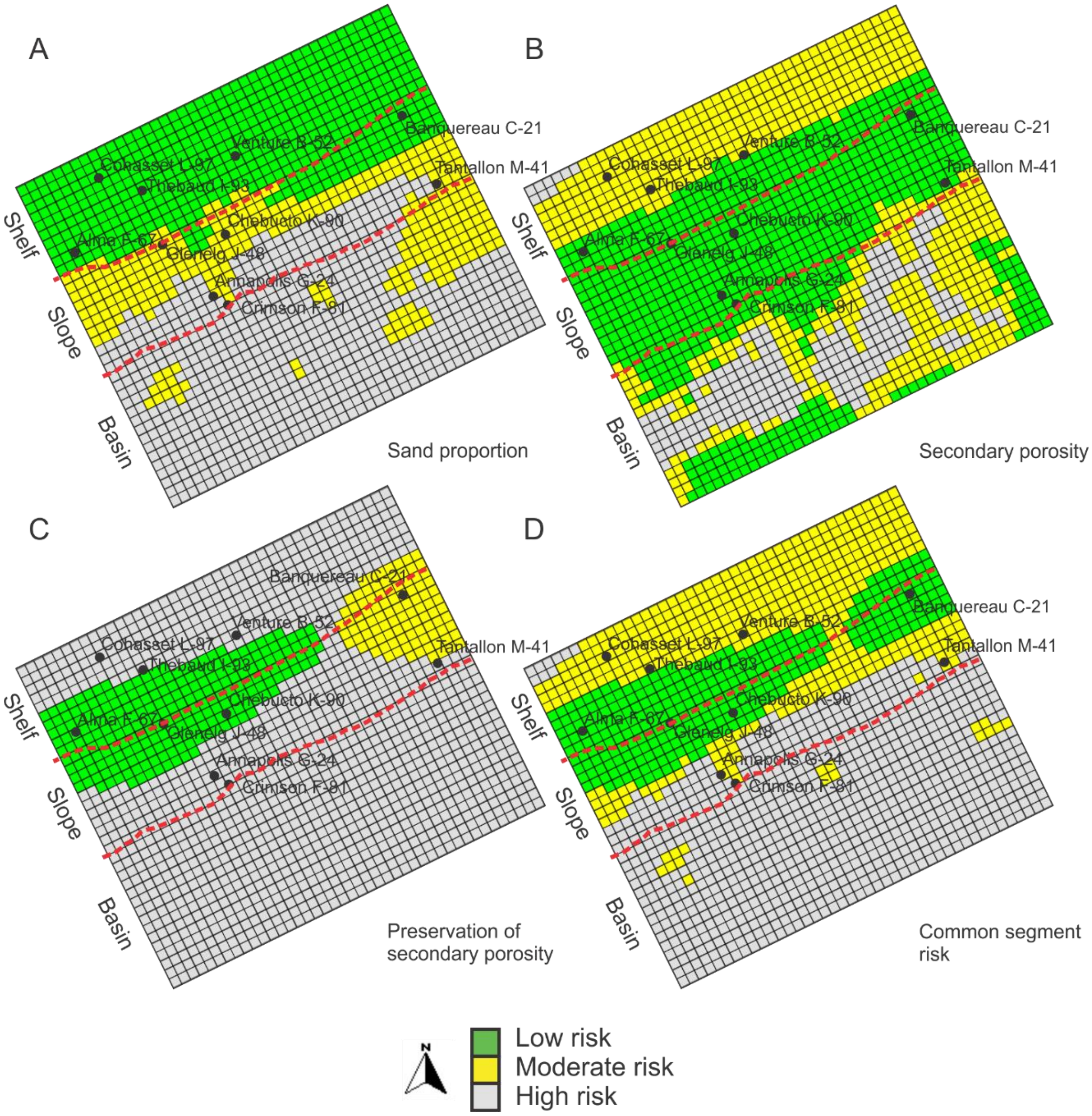

Figure 5.16: Risk maps for the Upper Missisauga Formation, showing component maps for **A)** sand distribution (Sangster et al., 2019), **B)** secondary porosity, **C)** preservation of secondary porosity, and **D)** common segment risk maps.

5.6 Conclusions

1. K-feldspar proportions show a decline with depth from the Cree Member to the Upper Missisauga Formation. Given the lack of a change in sediment source and no evidence for influence of climate, the decrease in feldspar is therefore primarily related to dissolution with burial and the increased temperatures and interactions with basinal fluids present during diagenesis. Dissolution of K-feldspar has been shown to occur at burial depths greater than 1.9 km sub sea floor, and are completed below 3.8 km sub sea floor.
2. Grain-size measurements show that K-feldspar grains are on average smaller than the mean quartz grain size in any given sample, likely as a result of great transport distances and modification as a result of diagenesis during burial.
3. Samples from the central and eastern basin show similar mean K-feldspar proportions and follow similar trends with depth, while the western basin shows a greater mean K-feldspar proportion. However, reconstruction of initial feldspar proportions suggests that the greatest feldspar concentrations are observed in the eastern basin at 15.5% followed by the central basin at 14.5% and with the lowest proportions present in the western basin at 11.8%.
4. Simulations of K-feldspar distribution show a similar trend to those observed in previous modelling of sand distribution. However, the largest concentrations of K-feldspar in the study area are in distal regions with lower sand content. This suggests that feldspar has a high potential to by-pass the modelled area into deeper parts of the basin.

5. Abundant faults and thick sands provide an open system in which the breakdown products from K-feldspar dissolution are removed allowing for preservation of secondary porosity. The central basin has most abundant faulting and thick sand beds and thus represents the lowest risk for lack of secondary porosity. Secondary porosity is estimated as 7–13% in the Upper Missisauga Formation and 5–12% in the Cree Member. The eastern study area represents a moderate risk for lack of secondary porosity.
6. Sand deposits on the shelf and slope have a lower risk than those in the basin, particularly in the Upper Missisauga Formation. With the lowest risk along the shelf edge and upper slope, particularly in the central and western study area. The lowest risk in the basin is classified as moderate, and located near the slope to basin transition.
7. K-feldspar rich sands transported into the deep basin likely contain limited secondary porosity, as a result of lacking a system capable of removing the breakdown products from the dissolution of K-feldspar.

Chapter 6: Discussion

Presented below is a summary of the most significant issues discussed in the previous chapters 4 and 5. These chapters are: a published paper (Chapter 4), and a soon to be submitted paper (Chapter 5).

6.1 Accuracy of provenance model

Provenance studies conducted in the region (Piper et al., 2012; Pe-Piper et al., 2014; Zhang et al., 2014) suggest that catchment areas remained unchanged throughout the Early Cretaceous. The exception was during the Naskapi Member, when the Sable and Banquereau rivers were probably diverted as a result of volcanism and uplift along their flow path (Bowman et al., 2012; Chavez et al., 2018; Sangster et al., 2019). During this time the Meguma Terrane was the source of new sediment to the Scotian Basin (Chavez et al., 2018).

The high degree of both thickness and facies calibration present on a basin wide scale suggests that provenance pathways proposed in the literature for the Early Cretaceous are broadly correct. In particular, model results support the hypothesis of sediment diversion during the Aptian on the basis of the sediment budget.

Simulation of the Naskapi Member used only a single, small volume, muddy source which supplied 6825 km^3 of sediments during the Aptian. This volume of sediment is significantly lower than that of the Barremian at 17,250 km^3 of sediments and the Albian, at 22,000 km^3. Given that there was probably no significant change in the catchment areas of the Sable and Banquereau rivers during the Early Cretaceous (Hendriks et al., 1993; Grist et al., 1995; Dickie et al., 2011), a large volume of sediments, approximately 26,000 km^3, if the lower rate of the Albian is applied, were deposited outside of the Scotian Basin during the deposition of the Naskapi Member. Sediment volumes of this magnitude would require an actively subsiding basin in order to trap the sediments up-dip from the central Scotian Basin. However, the major sedimentary basins which lay along the proposed sediment supply path of the Sable River are Paleozoic in age, and experienced significant uplift and erosion during the Mesozoic (Keen and Piper, 1990). The most proximal Early Cretaceous aged sediments in the Scotian Basin are found in the Orpheus Graben. However, Aptian sediments in this basin are shale prone, similar to those of the central Scotian Basin (Jansa and Pe-Piper, 1985). Minor Lower Cretaceous deposits of the Chaswood Formation have been identified in mainland Nova Scotian and Cape Breton (Falcon-Lang et al., 2007). These deposits are the proximal, onshore age equivalents of the Missisauga and Logan Canyon formations, and are preserved in several small fault bounded basins. However, these basins are small and account for less than 2 km^3 of Aptian sediment (as preserved). Given the high degree of model calibration, high sediment supply volumes, and lack of sufficiently large and active basins along the path of the Sable River during the Aptian, the scenario of the Sable and Banquereau rivers being diverted during this time is a more likely scenario. Diversion of the Sable and Banquerau rivers westwards into what is now the St. Lawrence River valley has been suggested (Chavez et al., 2018).

6.2 Climate, uplift, and sediment yield

Sediment budget calculations from modelling provide further information on the hinterland. While the style of sedimentation for the Upper Missisauga Formation and

Cree Member are very similar in terms of sediment distribution and source, these two units also have a very similar average thickness based on well picks despite a 6 Ma difference in depositional period. The similarity in thickness between these two units requires a lesser rate of input of sediment to the Cree Member, in the form of approximately half of the Upper Missisauga Formation supply from the Banquereau and Sable rivers, and approximately a quarter less from the Meguma Terrane.

Climate, lithology, and relief are generally considered to be the most important factors in controlling terrigenous sediment supply (Wolman and Gerson, 1978). Climate is an important factor in determining the types of sediment which are supplied to a region, with more humid climates being associated with an increased supply of clays as a result of increased chemical weathering. These conditions promote the breakdown of K-feldspar, and as a result, should be present in lower quantities in sediments derived from catchment areas with more humid climates (Ruffell and Batten, 1990; Ruffell and Worden, 2000; Gould et al., 2014). Paleoclimate studies of the Scotian Basin based on illite/kaolinite ratios suggest that climate fluctuated on a variety of time scales from arid to humid in the Early Cretaceous (Gould et al., 2014; Chavez et al., 2016). However, feldspar abundances show an inverse relationship with climate in analyzed samples, suggesting that if climate influences the proportion of K-feldspar, its influence is masked by other factors.

Paleoclimate reconstruction of the Scotian Basin are based on Th/K ratios of wireline spectral gamma logs taken from five outer Scotian Basin wells (Gould et al., 2014). These wireline logs, while continuous, have been used to reconstruct the paleoclimate of the Scotian Basin. However, they are of poorer resolution than core based logs and in addition include a potential source of error related to the presence of K rich volcanic detritus and changes in detrital input in the early Albian have been noted (Gould et al., 2014). As a result, paleoclimate reconstructions based on these results show relatively low resolution with regard to climate fluctuation when compared to paleoclimate reconstruction based on outcrop studies in western Europe (Ruffell et al., 2002; Fölmi, 2012). The paleoclimate of the Scotian Basin may therefore have been more complicated than what has been presented, and a more detailed analysis may reveal a larger impact of climate on both K-feldspar composition and sediment supply.

During the Early Cretaceous, rifting and ocean spreading (Louden et al., 2004) led to uplift of the Labrador Rift (Tappe et al., 2007) and reactivation of old fault lineaments in the Appalachians (Pe-Piper and Piper, 2012). Uplift in the Maritimes Basin (Grist et al., 1995) and Long Range Inlier of western Newfoundland (Hendriks et al., 1993) is suggested based on apatite fission track modelling during the Early Cretaceous. These areas provided sediments to the major rivers supplying sediment to the Scotian Basin during the Early Cretaceous. Additionally, uplift and tilting of the Meguma Terrain (Reynolds et al., 2012), occurred during the Aptian, diverting the Sable and Banquereau rivers. Provenance studies do not suggest that there were any large scale changes in the catchment areas supplying the region or decreased uplift during the Early Cretaceous (Zhang et al., 2014). Given that diversion of the Sable and Banquereau rivers had been established during the Aptian, and that other potential influences on sediment supply are not likely to have had a major effect, it is probable that these rivers also experienced episodic diversion during the deposition of the Cree Member.

Reference case models have been simulated assuming zero porosity for all sediment inputs and deposits. As a result, maximum sediment compaction has been considered as a part of this study. As a result, sediment input volumes predicted in the reference case models are greater than those present at the time of deposition, since simulated sediment thickness is calibrated to modern day sediment thicknesses which still contain preserved porosity. Sediment compaction is more significant at greater depth (Perrier and Quiblier, 1974), as a result the sediment supply (annual river load) to the Cree Member is more oversestimated than for the deeper Upper Missisauga Formation by approximitly 6% (if an average depth of 2 km is assumed for the Cree Member and 3 km for the Upper Misssiaga Formation) (Perrier and Quiblier, 1974). The Naskapi Member, which is composed dominantly of shales, would have experienced greater compaction than the other intervals in this study, although not more than in most deep water areas, due to the increased compaction which muds and clays experience compared to sands (Perrier and Quiblier, 1974), therefore, the sediment volume overestimation is likely not as great as in the sand dominated units. The differential compaction which would be experienced by the Cree Member and Upper Missisauga Formation in a natural system would likely strengthen arguments presented regarding the diversion of major rivers during the Albian, because it increases the difference in sediment volumes between the Upper Missisauga Formation and Cree Member by requiring less sediment volume to be supplied to the already lower sediment input volumes of the Cree Member. In addition to simulations not taking into account compaction, lithostratigraphic picks have been used in thickness calibration. As a result, the boundaries between units which are marked by unconformities, such as the top Upper Missisauga Formation and top Cree Member (Weston et al., 2012; OERA, 2016), do not take into account eroded sediments and may lead to underestimations of sediment volumes supplied to the basin for the Upper Missisauga Formation and Cree Member.

6.3 Shelf to deep water sand partitioning

As a result of the lack of data available from the deep basin, a key exploration risk in this region of the Scotian Basin is related to the extent to which sands have potentially bypassed the shelf. Simulation results show that, in the Upper Missisauga Formation and Cree Member, sand is trapped dominantly on the shelf, but also some was transported into the deep basin along salt-tectonics-related corridors and deposited in minibasins along the slope and basin. During deposition of the Naskapi Member, sands were trapped dominantly on the shelf with very limited transport into the basin. Simulated sand-rich sediment accumulation on the shelf follows a trend similar to that predicted by previous net to gross sand maps (OETR, 2011), with more sands in the eastern shelf decreasing to the west and decreasing significantly at the shelf edge in both the Upper Missisauga Formation and Cree Member.

The distribution of simulated sand bodies is consistent with seismic interpretations of deep basin sediments (Smith and Kendell, 2011) and core analysis of the Tantallon M-41 well (Piper et al., 2010) and Alma field (Piper et al., 2004). This supports their predictions of sand transport into the deep basin, likely as a result of turbidity current flows or other gravity flows partially bypassing the slope. The largest concentrations of sand resulting from this style of deposition appears to be in the eastern basin seaward of the Tantallon M-41 well. Sand was also transported along salt-tectonics-related corridors, particularly in the western edge of the simulated area, accumulating seaward of the Alma F-67, Annapolis G-24, and Crimson F-81 wells.

To determine the extent to which sands are transported to the deep basin floor, simulations were conducted using an extended map area with a 2 km deep row of cells at the seaward edge of the model. These simulations resulted in 5–22 % of the sand reaching the slope and basin accumulated at the edge of the model in the Upper Missisauga Formation and Cree Member, suggesting that sands are capable of being transported beyond the study area.

Sensitivity maps produced from CougarFlow™ analysis suggest that there are areas of low variance in the basin of the Upper Missisauga Formation and Cree Member, corresponding to areas where elevated sand concentration is predicted. The area basinward of the Tantallon M-41 well in particular shows low variance in the Upper Missisauga Formation. This suggests that predictions of sand accumulation in this area are robust.

6.4 Controls on feldspar dissolution

Given that there does not appear to be evidence of a major shift in the source areas which supplied sediment to the Scotian Basin, except during the deposition of the Naskapi Member, and the counter-intuitive relationship between inferred climatic shifts in the source areas and the measured K-feldspar content, the decrease in K-feldspar content with depth is likely related primarily to diagenetic processes. Previous studies show that the rate of K-feldspar breakdown increases exponentially with increased heat (Giles and de Boer, 1990). The wide range of depths and temperatures at which feldspar breaks down in different basins (Wilkinson et al., 2001) suggest that there is no systematic method, based only on burial depth, which can be used to predict the breakdown products of feldspar dissolution. The presence of clay minerals, albite, and secondary porosity are the result of local variables such as pore water chemistry, and mechanisms for fluid removal related to regional geological processes. Formation of clay mineral by-products can be reduced or prevented if dissolution occurs in an open system in which porewaters are removed from the system (Yuan et al., 2014). In the Scotian Basin, evidence of alteration of K-feldspar is present in the form of albitization, and is first documented at approximately 1.9 km burial depth, persisting until 3 km, with complete dissolution of K-feldspar occurring at 3.8–4.5 km (Pe-Piper and Yang, 2014). These observations are based on wells located in the central and eastern basin, and therefore likely experienced varying conditions of both temperature and faulting. K-feldspar concentrations in this study appear to decrease at burial depths greater than 1.9 km trending towards 0% K-feldspar below 3.8 km. This suggests that the K-feldspar grains in the Scotian Basin experienced extensive dissolution deeper than 1.9 km burial depth, as a result of interactions with basinal fluids at increased temperatures. Samples shallower than this depth experienced minimal alteration and dissolution.

The Scotian Basin has experienced a complex thermal history (Bowman et al., 2012; Karim et al., 2012). It has been widely effected by a thermal event during the

Aptian-Albian (Bowman et al., 2012), which is recorded by high entrapment temperatures in primary fluid inclusions in quartz overgrowths and carbonate cements, and strongly negative $\delta^{13}C$ values in carbonate cements (Karim et al., 2012), suggesting a paleo-geothermal gradient of as high as 50°C/km (Pe-Piper et al., 2017). The modern geothermal gradient of 26.6°C/km burial depth (Issler, 1984) that has been applied to estimate secondary porosity is thus likely to be only a crude guide to K-feldspar dissolution. Such dissolution occurs at a rate of approximately 2% total volume of K-feldspar/°C once deeper than the threshhold of 1.9 km, so that doubling the geothermal gradient would result in total dissolution at 3 km depth.

6.5 Evaluation of the risk associated with feldspar dissolution

K-feldspar grains are often comminuted during transport as a result of their cleavage and softness compared to quartz. Grain-size measurements of samples collected as part of this study show that all but one sample have a larger mean quartz grain size than K-feldspar (Fig. 5.7), with K-feldspar grains being an average of 11% smaller than the mean quartz grain size (Fig. 5.8A). K-feldspar grains have been shown to have been sourced largely from the Grenville Province (Tyrrell et al., 2014; Blowick et al., 2018), which is located over 600 km from the Scotian Basin. This great transport distance may have provided sufficient mechanical abrasion during transport to comminute feldspar grains. However, a trend of increased difference in grain size with decreasing feldspar proportion has been observed (Fig. 5.8A), suggesting that K-feldspar grain size has been modified by diagenesis during burial. However, samples at burial depths less than 1.9 km still show a mean grain size shift of ~10%, suggesting that transport processes were likely at play as well.

As a result of the smaller grain sizes of feldspar compared to quartz and the lower density of K-feldspar, these grains are transported further into the basin than their coarser quartz sand equivalents and at the edge of the simulated area, representing by-passing. As a result, while total sediments are enriched in K-feldspar on the shelf (Fig. 5.10), sands in the basin have greater concentrations of feldspars. This suggests that sand rich intervals in the basin have the greatest potential contribution to reservoir quality through the formation of secondary porosity. However, the largest concentrations of K-feldspar in the study area are in distal regions with lower sand content. As a result, while the basinal sands are associated with generally higher K-feldspar proportions, they form smaller potential reservoir intervals than on the shelf.

While the breakdown of K-feldspar is largely related to burial depth, the preservation of the generated secondary porosity is controlled by the ability of breakdown products to be removed from the system. Closed systems, in which fluids are unable to circulate, quickly become saturated in K^+ and Al^{3+}, resulting in the authigenesis of clays and limited formation of secondary porosity. Conversely, open systems allow for the removal of these products and the preservation of secondary porosity and permeability, as has been demonstrated recently by Yuan et al. (2015) in the Bohai Basin, East China.

Basin-margin faults are more abundant in the central Scotian Basin (Fig. 5.13) than in the eastern basin (OETR, 2011; Fig. 5.13). Sandstones in the central basin are thus more likely to preserve secondary porosity. This prediction can be tested against the plug porosity-permeability data of Gould et al. (2011). High permeability samples are more common in the central basin for both the Cree Member and Upper Missisauga Formation. Lithofacies associated with high permeability reservoirs are also generally thicker in the central basin than in the eastern portion (Gould et al., 2011). Lower permeability samples in both areas tend to occur in thinner and more discontinuous sandstone facies (Zhang et al., 2015), which are less likely to allow efficient advection of dissolution products.

When risks associated with sand distribution, secondary porosity generations, and secondary porosity preservation are considered, the area of the shelf edge and upper slope are associated with reduced risk in both the Upper Missisauga Formation, and Cree Member. However, as a result of increased temperatures in the Upper Missisauga Formation regions of low risk are more prevalent.

6.6 Successes and failures of methodology

6.6.1 Modelling approach

The Scotian Basin has been strongly influenced by salt tectonics, which has been a major complication for exploration in the area. “Source to sink” studies and numerical modelling software have been used to better assess the evolution of sedimentary basins and predict the location of sandstone reservoirs in other regions. However, due to the complications associated with modelling and seismic interpretation in salt basins, the majority of published modelling research has been conducted in regions without effects from salt tectonism. This study employs a simplified approach in which only the vertical movement of the salt bodies was considered, using subsidence variations to recreate sediment distribution patterns. This simulates the net tendencies of sediment accumulation as a result of salt mobilization, not the movement of the salt itself, and can be applied to other basins where salt mobility is not well constrained.

Seismic surfaces are available for the top and base of the study interval. These surfaces are used to calibrate sediment volume inputs. In order to generate models which could test scenarios in all three units of interest, intermediate surfaces were generated as a ratio of the total thickness. This approach allows for a high level of calibration at a regional level, however, it generates high errors at calibration wells which must be calibrated to control sediment distributions. The error is associated with correcting the difference in thickness interpolated between the surfaces and well picks. Thickness calibration error could be reduced using intermediate seismic picks, allowing for a better calibration and a better approximation of the sedimentary system of the central Scotian Basin.

The bathymetric map generated as the starting point for simulations is based on paleo-water depth estimates in a small number of wells and seismic interpretations of the position of the shelf edge. Gradients in analogous slope systems were used. The sensitivity of the initial bathymetry has not been evaluated in CougarFlow, however, given the large cell size used during simulations and the variation of basin subsidence to control sediment accommodation, minor changes in the initial bathymetry likely has a minor effect on the simulated results.

The resolution of the model at 5 x 5 km cells allows for simulation of overall sediment distributions, however it is too coarse to account for fine channels, and autocylic variations in sand and mud deposition. Increasing the resolution of the model may result in an improved ability to capture fine scale features.

Diffusion coefficients have been generated on the basis of sediment supply, water discharge, sediment grain size, bathymetry, and slope gradient. As a result of the study area only extending as far onshore as shallow marine conditions, calculated diffusion coefficients for the continental realm cause a build-up of sediment at the edge of the model where sediments enter the system. In order to counteract this effect, continental diffusion coefficients have been increased by an order of magnitude to allow for sediments to be distributed across the shelf, and into the basin.

The frequency of high energy events used in the reference case models is based on observations from Haywood et al. (2004) regarding seasonal variations in water discharge from the continent. However, these observations are based on climate modelling in the Weald Basin, which although similar to the Scotian Basin during the Early Cretaceous, is not calibrated to high energy events present in the Scotian Basin. To improve the accuracy of these events in the reference case models, more specific climate modelling to the Scotian Basin could be applied.

Eustatic sea-level variation was not considered in CougarFlow analysis of the final reference case models. However, a test was conducted on the Upper Missisauga Formation to determine whether a significant change in eaustatic sea-level would have an impact on sediment thickness. Analysis was conducted by comparing simulation runs using the eustatic sea-level curves presented by Miller et al. (2005), Haq et al. (1987), and Van der Meer et al. (2017). The resulting standard deviation maps show the greatest variation along the slope and near the sediment input points in the model, following the same trends as sensitivity analysis conducted as part of this study. Generally, less than 5% variation in resulting sediment thickness was observed, as a result, different eustatic sea-level curves were not tested as a part of the final CougarFlow analysis.

Analysis of continental slopes and base-of-slope systems by Prather et al. (2017) demonstrated that slope systems generally increase in sand content from the upper to lower slope, with the highest sand concentrations located in basin floor deposits. The cause of low sand content in the upper slope is related to the deposition of hemipelagic sediments and clays supplied by gravity flows and fallout from suspended plumes, both of which are supplied by shelf edge deltas (Prather et al., 2017). These hemipelagic sediments form mud belts at the top of the slope, and taper out down the slope. Simulations conducted as part of this study suggest the opposite relationship on the slope, although the large basin floor deposits are observed (Fig. 4.10). Reference case models appear to follow trends present in lithofacies interpretation of the Scotian Basin, with interbedded prodeltaic sands and muds present in the shelf edge to upper slope transitioning to interbedded shales and sands on the slope (OETR 2011). However, hemipelagic sedimentation, which is simulated using a growth rate similar to carbonates, has not been considered as part of this study. As a result, alteration of simulation parameters to deposit more clay sized sediments at the upper slope may result in a reduction in the sand content, which would conform to observed sediment partitioning on the slope in Prather et al. (2017).

6.6.2 Feldspar analysis

Samples collected as part of this study are dominantly smear slides produced from sidewall core rubble. This sampling approach allowed for extensive sampling throughout the study area, allowing for a detailed understanding of the influences of diagenesis on K-feldspar proportion in the central Scotian Basin through time. However, as these samples have been produced from loose sediment, the extent to which K-feldspar has contributed secondary porosity during diagenesis cannot be quantified. This is due to the destruction of texture present within the sample, which prevents calculation of porosity in thin section, as well as distinguishing between detrital and authigenic clays which may have formed as by-products of K-feldspar dissolution in each sample.

K-feldspar distribution has been simulated on the basis of reconstructed K-feldspar inputs from the three major source rivers during the Early Cretaceous. Reconstructions are based on a line of best fit running from 3.8 km to 1.9 km burial depth, resulting in the lowest input from the Meguma Terrain. However, samples from the western basin are generally taken from burial depths of less than 1.9 km with no samples below 2.6 km burial depth, additionally the western basin has had only nine samples analyzed. As a result estimates for the western basin may not be as representative. Additionally, samples collected from this study are dominantly from the fine and very-fine grain size fractions, with only three samples analyzed from the medium sized fraction and none from the coarse fraction. Both Odom (1976) and Blatt et al. (1972) suggest that feldspar proportions are likely to be greater in finer sand fractions, and while samples collected from shallower than 1.9 km burial depth do not appear to show major differences in feldspar proportion in this study, the low number of samples from the coarser sand fraction to fully evaluate this partitioning may lead to a slight over estimation of feldspar proportions from all sources.

6.7 Methodological contributions

This study builds upon previous work conducted on measuring mineral composition of sandstones by Zhang et al. (2015), in which minerals are differentiated on the basis of EDS chemical analysis and by using their gray-scale brightness in BSE images, which is controlled by their mean atomic number (Tovey and Krinsley, 1992). An additional step of taking “quick” X-ray maps to reduce the number of analyses required to identify minerals decreases the amount of time required to analyze each sample. Additionally, the PowerTrace^{TM} tool in CorelDraw^{TM} was used to eliminate noise, and easily apply false colour to images for quick selection for further statistical analysis. MultiSpec^{TM} image analysis software was used in this study rather than ImageJ^{TM} as it easily allows for analysis of coloured images. This methodology provides an efficient procedure for point counting on the basis of SEM BSE images which are more reliable than standard point counting analysis on a petrographic microscope, particularly in differentiating K-feldspar, plagioclase, and quartz in sedimentary samples.

6.8 Reduced risk

The Offshore Energy Research Association (OERA) Geoscience Research Priorities considers “Reservoir Quality” to be a high priority, with particular emphasis on the Sable and north east regions of the Scotian Basin. While this area has been the subject of much research and exploration, the distribution and quality of reservoir sandstone units is poorly understood, particularly in the deep basin, where few wells have been drilled, and exploration is further complicated by the widespread salt tectonism as well as the strong influence of diagenesis on reservoir quality. Exploration risk has been reduced in this study by predicting the presence of sand bodies in the basin, in addition to predicting sediment by-pass to the deep basin floor using forward stratigraphic modelling software.

Risks associated with the influence of diagenesis on reservoir quality have been reduced by predicting the distribution of K-feldspar, which is strongly influenced by diagenesis after deposition. With depth and increasing temperature, K-feldspar has been shown to break down and produce numerous authigenic phases, including authigenic K-feldspar, albite, kaolinite, and illite. However, in systems with abundant faults and fractures or beds with high permeability, these phases can be removed from the system and secondary porosity is generated. By comparing the Scotian Basin to other basins where open systems are observed, low risk regions of the basin have been identified, specifically in two regions of the study area where abundant faulting and highly permeable intervals are present. Additionally the potential secondary porosity present can be predicted by comparing the simulated distribution of K-feldspar in the basin with thermal history maps, and the rate of K-feldspar dissolution interpreted in the Scotian Basin.

Chapter 7: Conclusions

1. Reference case models have been calibrated to capture the major trends of sediment distribution for the Upper Missisauga Formation (Hauterivian-Barremian), Naskapi Member (Aptian), and Cree Member (Albian). The high degree of both thickness and facies calibration present on a basin wide scale suggests that provenance pathways proposed in the literature for the Early Cretaceous are correct. Sediment supply variations suggest that the Naskapi Member likely formed as the result of tectonic diversion of the Sable River and Banquereau rivers, and the decrease in sediment supply to the Cree Member compared to the Upper Missisauga Formation, despite a lack in changes to the catchment areas, also suggest episodic diversion of these rivers during the Albian.
2. Sand distribution maps and sensitivity analyses suggest that sand is distributed dominantly on the shelf in the Upper Missisauga Formation and Cree Member, and along the slope in the Naskapi Member. Transport to the basin occurred in salt-withdrawal-related corridors caused by turbidity current flows. This study predicts that there likely are accumulations of sandy sediments seaward of the Alma F-67, Annapolis G-24, and Crimson F-81 wells, with a large deposit seaward of the Tantallon M-41 well in both the Upper Missisauga Formation and Cree Member. Extended area simulations show sand transport beyond the study area, suggesting that there is potential for exploration in the deep basin.
3. K-feldspar proportions show a decline with depth from the Cree Member to the Upper Missisauga Formation. Provenance studies conducted in the region suggest

that catchment areas remained unchanged throughout the Early Cretaceous. Therefore, the observed trends in feldspar proportion are not likely related to changes in sediment provenance. Comparisons of feldspar proportions and climate show that intervals with more humid conditions show greater K-feldspar proportions, suggesting that if climate influences the proportion of K-feldspar, its influence is masked by other factors. The decrease in feldspar proportion is therefore related mainly to dissolution with burial and the increased temperatures and interactions with basinal fluids present during diagenesis. Dissolution of K-feldspar has been shown to occur at burial depths greater than 1.9 km sub sea floor, and is complete below 3.8 km sub sea floor.

4. Reconstruction of initial feldspar proportion suggest that the greatest feldspar concentrations are observed in the eastern basin at 15.5% followed by the central basin at 14.5% and with the lowest proportions present in the western basin at 11.8%.
5. Simulations of K-feldspar distribution show a similar trend to those observed previous modelling of sand distribution. However, the largest concentrations of K-feldspar are in distal regions with lower sand content, such as around salt withdrawal corridors, basinward of sand rich mini-basins, and the flanks of salt bodies. This distribution suggests that feldspar has a high potential to bypass the modelled area into deeper parts of the basin.
6. Abundant faults and thick sands provide an open system in which the breakdown products from K-feldspar dissolution are removed allowing for preservation of

secondary porosity. The central basin has most abundant faulting and thick sand beds and thus represents the lowest risk for lack of secondary porosity. Secondary porosity is estimated as 7–13% in the Upper Missisauga Formation and 5–12% in the Cree Member. The eastern study area represents a moderate risk for lack of secondary porosity.

7. The application of forward stratigraphic modelling presented in this thesis provides a framework for evaluating proposed provenance pathways, reservoir distribution, and reservoir quality, which can be applied to other basins on a global scale. The confidence in the reference case model calibration on the shelf and slope allows for predictions of sediment distribution in the underexplored deep basin. A simplified approach to modelling of salt bodies on the basis of preserved sediment thickness and subsidence has also been presented, and has the potential to be applied to other basins where salt tectonics were actively controlling sediment distribution, such as in the Gulf of Mexico.

References

Aagaard, P., Egeberg, P. K., Saigal, G. C., Morad, S., & Bjorlykke, K. (1990). Diagenetic albitization of detrital K-feldspars in Jurassic, Lower Cretaceous and Tertiary clastic reservoir rocks from offshore Norway; II, Formation water chemistry and kinetic considerations. Journal of Sedimentary Research, v. 60, p. 575–581.

Agrawal, D., Dwivedi, S., Barrois, A., Koeck, C., El-Wazir, Z., Al-Madani, N., & Aillud, G. (2015). Impact of Environmental Parameters on Forward Stratigraphic Modelling from Uncertainty Analysis; Lower Cretaceous, Abu Dhabi. In SPE Reservoir Characterisation and Simulation Conference and Exhibition, Abu Dhabi, UAE, Society of Petroleum Engineers, 12 pp.

Albertz, M., Beaumont, C., Shimeld, J. W., Ings, S. J., & Gradmann, S. (2010). An investigation of salt tectonic structural styles in the Scotian Basin, offshore Atlantic Canada: 1. Comparison of observations with geometrically simple numerical models. Tectonics, v. 29, TC4017. https://doi.org/10.1029/2009TC002539

Allen, P. A. (2008). From landscapes into geological history. Nature, v. 451, p. 274–276. https://doi.org/10.1038/nature06586

Ascoli, P. (2010). Report on the Mesozoic foraminiferal and ostracod biostratigraphy and depositional environments of Shell, PCI et al. Alma K-85, from 795 to 3602 m (T.D.). Report No. M.R.G.-PAL.02-2010PA, 9 pp.

Ascoli, P. (2011). Report on the Mesozoic foraminiferal and ostracod biostratigraphy and depositional environments of Petro-Canada et al. Banquereau C-21, from 1600 to 4991 m (T.D.). Report No. M.R.G.-PAL.04-2011PA, 9 pp.

Beck, M. E. J., & Housen, B. A. (2003). Absolute velocity of North America during the Mesozoic from paleomagnetic data. Tectonophysics, v. 377, p. 33–54. https://doi.org/10.1016/j.tecto.2003.08.018

Bauluz, B., Mayayo, M. J., Yuste, A., & González-López, J. M. (2008). Genesis of kaolinite from Albian sedimentary deposits of the Iberian Range (NE Spain): Analysis by XRD, SEM and TEM: Clay Minerals, v. 43, p. 459–475, https://doi:10.1180/claymin.2008.043.3.10

Bjørlykke, K. (1998). Clay mineral diagenesis in sedimentary basins—A key to the prediction of rock properties. Examples from the North Sea Basin: Clay Minerals, v. 33, p. 15–34, https://doi:10.1180/000985598545390

Bjørlykke, K., & Jahren, J. (2012). Open or closed geochemical systems during diagenesis in sedimentary basins: Constraints on mass transfer during diagenesis and the prediction of porosity in sandstone and carbonate reservoirs: AAPG Bulletin, v. 96, p. 2193–2214, https://doi:10.1306/04301211139

Blatt, H., Middleton, G., & Murray, R. (1972) Origin of sedimentary rocks. Englewood Cliffs, NJ: Prentice-Hall incorporated.

Bowman, S. J., Pe-Piper, G., Piper, D. J. W., Fensome, R. A., & King, E. L. (2012). Early Cretaceous volcanism in the Scotian Basin. Canadian Journal of Earth Sciences, v. 49, p. 1523–1539.

Brown Jr., L. F., & Loucks, R. G. (2009). Chronostratigraphy of Cenozoic depositional sequences and systems tracts: A Wheeler chart of the northwest margin of the Gulf of Mexico Basin. The University of Texas at Austin, Bureau of Economic Geology Report of Investigations, v. 273, 28 pp.

Chavez, I., Piper, D. J. W., & Pe-Piper, G. (2018). Correlation of the Aptian Naskapi Member of the Scotian Basin and its regional implications. Canadian Journal of Earth Sciences, v. 55, p. 514–535. https://doi.org/10.1139/cjes-2017-0205

Chavez, I., Piper, D. J. W., Pe-Piper, G., Zhang, Y. (2016). North Atlantic climatic events recorded in Aptian Naskapi Member cores, Scotian Basin. Cretaceous Research, v. 60, p. 297–307.

Chorowicz, J. (2005). The east African rift system. Journal of African Earth Sciences, v. 43, p. 379–410. https://doi.org/10.1016/j.jafrearsci.2005.07.019

Chuhan, F. A., Bjørlykke, K., & Lowrey, C. J. (2001). Closed-system burial diagenesis in reservoir sandstones: Examples from the Garn Formation at Haltenbanken area, offshore mid-Norway. Journal of Sedimentary Research, v. 71, p. 15–26.

Corel (2016). CorelDraw X7 and X3. Retrieved from https://www.coreldraw.com/en/ accessed 7/13/2019.

Cummings, D. I., & Arnott, R. W. C. (2005). Growth-faulted shelfmargin deltas: A new (but old) play type, offshore Nova Scotia. Bulletin of Canadian Petroleum Geology, v. 53, p. 211–236. https://doi.org/10.2113/53.3.211

Cummings, D. I., Hart, B. S., & Arnott, R. W. C. (2006). Sedimentology and stratigraphy of a thick, areally extensive fluvial–marine transition, Missisauga Formation, offshore Nova Scotia, and its correlation with shelf margin and slope strata. Bulletin of Canadian Petroleum Geology, v. 54, p. 152–174. https://doi.org/10.2113/gscpgbull.54.2.152

Dai, A., & Trenberth, K. E. (2002). Estimates of freshwater discharge from continents: Latitudinal and seasonal variations. Journal of Hydrometeorology, v. 3, p. 660–687. https://doi.org/10.1175/1525-7541(2002)003<0660:EOFDFC>2.0.CO;2

Delaplace, P., Renard, G., Delamaide, E., Euzen, T., Roggero, F., & Kopecny, P. (2013). Reservoir simulations of a polymer flood pilot in the pelican lake heavy oil field (Canada): A step forward. In SPE Reservoir Characterization and Simulation Conference and Exhibition, Abu Dhabi, UAE, Society of Petroleum Engineers, 14 pp.

Deptuck, M. E. (2008). Call for Bids – Sub-regional geology and exploration potential for Parcels 1 and 2, Central Scotian Slope. CNSOPB Call for Bids. Geoscience Package, NS08-2, 49 pp.

Deptuck, M. E., Kendell, K., & Smith, B. (2009). Complex deepwater fold belts in the SW Sable Subbasin, offshore Nova Scotia: Canadian Society of Petroleum Geologists/Canadian Society of Exploration Geophysicists/Canadian Well Logging Society Convention, Calgary, Alberta, May 4–8, 2014, 4 p.

Deptuck, M. E., Kendell, K., Brown, D. E., & Smith, B. M. (2014). Seismic stratigraphic framework and structural evolution of the eastern Scotian Slope: geological context for the NS14-1 Call for Bids area, offshore Nova Scotia. CNSOPB Open File Report, 2014–001MF, 58 pp.

Deptuck, M. E., Brown, D. E., & Altheim, B. (2015). Call for Bids NS15-1 – Exploration history, geologic setting, and exploration potential: Western and Central regions. CNSOPB Open File Report, 2015–001MF, 49 pp.

Deville, E., Mascle, A., Callec, Y., Huyghe, P., Lallemant, S., Lerat, O., Mathieu, X., De Carillo, C. P., Patriat, M., & Pichot, T. (2015). Tectonics and sedimentation interactions in the east Caribbean subduction zone: an overview from the Orinoco delta and the Barbados accretionary prism. Marine and Petroleum Geology, v. 64, p. 76–103.

Dickie, K., Keen, C. E., Williams, G. L., & Dehler, S. A. (2011). Tectonostratigraphic evolution of the Labrador margin, Atlantic Canada. Marine and Petroleum Geology, v. 28, p. 1663–1675. https://doi.org/10.1016/j.marpetgeo.2011.05.009

Ehrenberg, S. N., Nadeau, P. H., & Steen, Ø. (2008). A megascale view of reservoir quality in producing sandstones from the offshore Gulf of Mexico: AAPG Bulletin, v. 92, p. 145–164, https://doi:10.1306/09280707062

Falcon-Lang, H. J., Fensome, R. A., Gibling, M. R., Malcolm, J., Fletcher, K. R., & Holleman, M. (2007). Karst-related outliers of the Cretaceous Chaswood Formation of maritime Canada. Canadian Journal of Earth Sciences, v. 44, p. 619–642. https://doi.org/10.1139/e06-119

Franks, S. G., & Zwingmann, H. (2010). Origin and timing of late diagenetic illite in the Permian–Carboniferous Unayzah sandstone reservoirs of Saudi Arabia: AAPG Bulletin, v. 94, p. 1133–1159, https://doi:10.1306/04211009142

Garzanti, E., Andò, S., & Vezzoli, G. (2008). Settling equivalence of detrital minerals and grain-size dependence of sediment composition. Earth and Planetary Science Letters, v. 273, p. 138–151.

Giles, M. R., & De Boer, R. B. (1990). Origin and significance of redistributional secondary porosity. Marine and Petroleum Geology, v. 7, p. 378–397.

Gradstein, F. M., Ogg, J., & Smith, S. G. (2005). A geological time scale 2004. Cambridge University Press, Cambridge. 589 pp.

González-Acebrón, L., Arribas, J., & Mas, R. (2010). Role of sandstone provenance in the diagenetic albitization of feldspars: A case study of the Jurassic Tera Group sandstones (Cameros Basin, NE Spain). Sedimentary Geology, v. 229, p. 53–63.

Gould, K., Pe-Piper, G., & Piper, D. J. W. (2010). Relationship of diagenetic chlorite rims to depositional facies in Lower Cretaceous reservoir sandstones of the Scotian Basin. Sedimentology, v. 57, p. 587–610. https://doi.org/10.1111/j.1365-3091.2009.01106.x

Gould, K. M., Karim, A., Piper, D. J. W., & Pe-Piper, G. (2011). Lithofacies and diagenesis of selected conventional core from Jurassic and Early Cretaceous terrigenous clastic rocks, Scotian Basin. Geological Survey of Canada, Open File 6945, 272 pp. https://doi:10.4095/289629

Gould, K. M., Piper, D. J. W., & Pe-Piper, G. (2012). Lateral variation in sandstone lithofacies from conventional core, Scotian Basin: Implications for reservoir quality and connectivity. Canadian Journal of Earth Sciences, v. 49, p. 1478–1503.

Gould, K. M., Piper, D. J. W., Pe-Piper, G., & MacRae, R. A. (2014). Facies, provenance and paleoclimate interpretation using spectral gamma logs: Application to the Lower

Cretaceous of the Scotian Basin. Marine and Petroleum Geology, v. 57, p. 445–454. https://doi.org/10.1016/j.marpetgeo.2014.06.008

Granjeon, D. (1996). Modelisation stratigraphique deterministe—conception et applications d'un modele diffusif 3D multi-lithologique. Rennes, France: Geosciences Rennes, Universite de Rennes 1.

Granjeon, D. (2014) 3D forward modelling of the impact of sediment transport and base level cycles on continental margins and incised valleys. International Association of Sedimentology Special Publication, p. 46, v. 453–472.

Granjeon, D., & Joseph, P. (1999). Concepts and applications of a 3-D multiple lithology, diffusive model in stratigraphic modelling. Society for Sedimentary Geology Special Publications, v. 62, p. 197–210.

Grant S., Milton N., & Thompson M. (1996). Play fairway analysis and risk mapping: an example using the Middle Jurassic Brent group in the northern North Sea. In Norwegian Petroleum Society Special Publications, v. 6, p. 167–181. Elsevier.

Grist, A., Reynolds, P., Zentilli, M., & Beaumont, C. (1992). The Scotian Basin offshore Nova Scotia: Thermal history and provenance of sandstones from apatite fission track and ^{40}Ar/^{39}Ar data. Canadian Journal of Earth Sciences, v. 29, p. 909–924.

Hacquebard, P.A. (1984). Composition, rank and depth of burial of two Nova Scotia lignite deposits. Geological Survey of Canada Paper, v. 84, p. 11–15.

Haq, B. U., Hardenbol, J. A., & Vail, P. R. (1987). Chronology of fluctuating sea levels since the Triassic. Science, v. 235, p. 1156–1167.

Haszeldine, R. S., Wilkinson, M., Darby, D., Macaulay, C. I., Couples, G. D., Fallick, A. E., Fleming, C. G., Stewart, R. N., & McAulay, G. (1999). Diagenetic porosity creation in an overpressured graben. In Geological Society, London, Petroleum Geology Conference series 1999 Jan 1, v. 5, p. 1339–1350. Geological Society of London.

Hawie, N., Barrois, A., Marfisi, E., Murat, B., Hall, J., El-Wazir, Z., Al-Madani, N., Aillud, G. (2015). Forward stratigraphic modelling, deterministic approach to improve carbonate heterogeneity prediction; Lower Cretaceous, Abu Dhabi. In Abu Dhabi International Petroleum Exhibition and Conference, Abu Dhabi, UAE, Society of Petroleum Engineers, 15 pp.

Hawie, N., Covault, J. A., Dunlap, D., & Sylvester, Z. (2018). Slope-fan depositional architecture from high-resolution forward stratigraphic models. Marine and Petroleum Geology, v. 91, p. 576–585. https://doi.org/10.1016/j.marpetgeo.2017.12.033

Hawie, N., Deschamps, R., Granjeon, D., Nader, F. H., Gorini, C., Müller, C., Montadert, L., & Baudin, F. (2017). Multi-scale constraints of sediment source to sink systems in frontier basins: A forward stratigraphic modelling case study of the Levant region. Basin Research, v. 29, p. 418–445. https://doi.org/10.1111/bre.12156

Haywood, A. M., Valdes, P. J., & Markwick, P. J. (2004). Cretaceous (Wealden) climates: a modelling perspective. Cretaceous Research, v. 25, p. 303–311.

Hendriks, M., Jamieson, R. A., Willett, S., & Zentilli, M. (1993). Burial and exhumation of the Long Range Inlier and its surroundings, western Newfoundland: Results of an apatite fission-track study. Canadian Journal of Earth Sciences, v. 30, p. 1594–1606. https://doi.org/10.1139/e93-137

Higgs, K. E., Zwingmann, H., Reyes, A. G., & Funnell, R. H. (2007). Diagenesis, porosity evolution, and petroleum emplacement in tight gas reservoirs, Taranaki Basin, New Zealand. Journal of Sedimentary Research, v. 77, p. 1003–1025.

Huang, X., Griffiths, C., & Liu, J. (2015). Recent development in stratigraphic forward modelling and its application in petroleum exploration. Australian Journal of Earth Sciences, v. 62, p. 903–919. https://doi.org/10.1080/08120099.2015.1125389

IFP Energies nouvelles and BeicipFranlab (2016a). DionisosFlow software. Retrieved from http://www.beicip.com/stratigraphic-modelling-0 accessed 7/13/2019.

IFP Energies nouvelles and BeicipFranlab (2016b). CougarFlow software. Retrieved from http://www.beicip.com/uncertainty-management-assisted-history-matching accessed 7/13/2019.

Ings, S.J., & Shimeld, J.W. (2006). A new conceptual model for the structural evolution of a regional salt detachment on the northeast Scotian margin, offshore eastern Canada. AAPG Bulletin, v. 90, p. 1407–1423.

Issler, D. R. (1984). Calculation of organic maturation levels for offshore eastern Canada—implications for general application of Lopatin's method. Canadian Journal of Earth Sciences, v. 21, p. 477–488.

Jansa, L. F., & Wade, J. A. (1975). Geology of the continental margin off Nova Scotia and Newfoundland. In W. J. M. van der Linden, & J. A. Wade (Eds.), Offshore geology of eastern Canada, Part 2 Regional geology (pp. 51–106). Ottawa, ON: Geological Survey of Canada.

Jansa, L. F., & Pe-Piper, G. (1985). Early Cretaceous volcanism on the northeastern American margin and implications for plate tectonics. Geological Society of America Bulletin, v. 96, p. 83–91. https://doi.org/10.1130/0016-7606(1985)96<83:ECVOTN>2.0.CO;2

Keen, M. J., & Piper, D. J. W. (1990). Geological and historical perspective. In M. J. Keen et al. (Eds.), Geology of the continental margin of eastern Canada. Geological Survey of Canada, Geology of Canada (vol. 2, pp. 5–30). Ottawa, ON: Geological Survey of Canada.

Kendell, K. L. (2012). Variations in salt expulsion style within the Sable canopy complex, central Scotian margin. Canadian Journal of Earth Sciences, v. 49, p. 1504–1522.

Kidston, A. G., Smith, B., Brown, D. E., Makrides, C., & Altheim, B. (2007). Nova Scotia deep water offshore post-drill analysis 1982–2004 (pp. 181). Halifax, NS: Canada-Nova Scotia Offshore Petroleum Board.

Kubo, Y. S., Syvitski, J. P., Hutton, E. W., & Paola, C. (2005). Advance and application of the stratigraphic simulation model 2D-SedFlux: From tank experiment to geological scale simulation. Sedimentary Geology, v. 178, p. 187–195. https://doi.org/10.1016/j.sedgeo.2005.04.005

Lacroix, S., & Albadi, B. S. (2012). Improving the Uncertainty Understanding for the Optimal Development of an Abu Dhabi Offshore Green Field. In Abu Dhabi

International Petroleum Conference and Exhibition, Abu Dhabi, UAE, Society of Petroleum Engineers, 9 pp.

Lanson, B., Beaufort, D., Berger, G., Bauer, A., Cassagnabère, A., & Meunier, A. (2002). Authigenic kaolin and illitic minerals during burial diagenesis of sandstones: A review: Clay Minerals, v. 37, p. 1–22, https://doi:10.1180/0009855023710014

Li, G., Ravenhurst, C., & Zentilli, M. (1995). Implications of apatite fission track analysis for the thermal history of the Scotian Basin, offshore Nova Scotia, Canada. Bulletin of Canadian Petroleum Geology, v. 43, p.127–144.

Louden, K. E., Tucholke, B. E., & Oakey, G. N. (2004). Regional anomalies of sediment thickness, basement depth and isostatic crustal thickness in the North Atlantic Ocean. Earth and Planetary Science Letters, v. 224, p. 193–211. https://doi.org/10.1016/j.epsl.2004.05.002

Lowe, D. G., Sylvester, P. J., & Enachescu, M. E. (2011). Provenance and paleodrainage patterns of Upper Jurassic and Lower Cretaceous synrift sandstones in the Flemish Pass Basin, offshore Newfoundland, east coast of Canada. AAPG Bulletin, v. 95, p. 1295–1320. https://doi.org/10.1306/12081010005

Macgregor, D. S. (2012). The development of the Nile drainage system: Integration of onshore and offshore evidence. Petroleum Geoscience, v. 18, p. 417–431. https://doi.org/10.1144/petgeo2011-074

MacLean, B. C., & Wade, J. A. (1993) East Coast Basin Atlas Series: Seismic Markers and Stratigraphic Picks in Scotian Basin Wells. Atlantic Geoscience Centre, Geological Survey of Canada, 276 pp. Geological Survey of Canada Publication.

Martinsen, O., Sømme, T., Thurmond, J., Helland-Hansen, W., & Lunt, I. (2010). Source-to-sink systems on passive margins: theory and practice with an example from the Norwegian continental margin. In B. A. Vining, et al. (Eds.), Petroleum geology: From mature basins to new frontiers (vol. 7, pp. 913–920), Proceeding of the 7th Petroleum Geology Conference, v. 7, p. 913–920. London, UK: Geological Society of London.

McDonnell, A., Loucks, R. G., & Galloway, W. E. (2008). Paleocene to Eocene deep-water slope canyons, western Gulf of Mexico: Further insights for the provenance of deep-water offshore Wilcox Group plays. AAPG Bulletin, v. 92, p. 1169–1189. https://doi.org/10.1306/05150808014

Meade, R. H. (1972). Sources and sinks of suspended matter on continental shelves. Shelf sediment transport: Process and pattern, p. 249–260.

Meade, R. H. (1982). Sources, sinks, and storage of river sediment in the Atlantic drainage of the United States. The Journal of Geology, v. 90, p. 235–252. https://doi.org/10.1086/628677

Miller, K. G., Kominz, M. A., Browning, J. V., Wright, J. D., Mountain, G. S., Katz, M. E., Sugarman, P. J., Cramer, B. S., Christie-Blick, N., Pekar, S. F. (2005). The Phanerozoic record of global sea-level change. Science, v. 310, p. 1293–1298.

Milliman, J. D., & Syvitski, J. P. (1992). Geomorphic/tectonic control of sediment discharge to the ocean: The importance of small mountainous rivers. The Journal of Geology, v. 100, p. 525–544. https://doi.org/10.1086/629606

Morad, S., Al-Ramadan, K., Ketzer, J. M., De Ros, L. F. (2010). The impact of diagenesis on the heterogeneity of sandstone reservoirs: A review of the role of depositional facies and sequence stratigraphy. AAPG Bulletin, v. 94, p.1267–1309.

Nagle, J. (2018). Diagenesis and Provenance of Marmora and Sable members of the Upper Logan Canyon Formation, in wells near Sable Island. B.Sc. Hon. Thesis, Saint Mary's University, Halifax, Nova Scotia, 463 pp.

NIH (National Institutes of Health) (2019). ImageJ image analysis software. Retrieved from https://imagej.nih.gov/ij/disclaimer.html accessed 7/13/2019.

Natural Resources Canada (2016). Basin database [online]. Retrieved from http://basin.gdr.nrcan.gc.ca/wells/index_e.php

Nesbitt, H. W., & Young, G. M. (1996). Petrogenesis of sediments in the absence of chemical weathering: effects of abrasion and sorting on bulk composition and mineralogy. Sedimentology, v. 43, p. 341–358.

Nesse, W. D. (2013). Introduction to optical mineralogy, 4th ed. New York, NY: Oxford University Press.

Odom, I. E., Doe, T. W., & Dott, R.H. (1976). Nature of feldspar-grain size relations in some quartz-rich sandstones. Journal of Sedimentary Research, v. 46, p. 862-870.

OERA (Offshore Energy Research Association) (2016). Central Scotian Slope atlas [online]. Retrieved from http://www.oera.ca/offshore-energy-research/geoscience/central-scotian-slope-atlas-2016/

OETR (Offshore Energy Technical Research Association) (2011). Play fairway analysis atlas–offshore Nova Scotia. Nova Scotia Department of Energy, 88-11-0004-01, 349 pp. https://energy.novascotia.ca/oil-and-gas/offshore/play-fairway-analysis

Okwese, A. C., Pe-Piper, G., & Piper, D. J. W. (2012). Controls on regional variability in marine pore-water diagenesis below the seafloor in Upper Jurassic–Lower Cretaceous prodeltaic sandstone and shales, Scotian Basin, Eastern Canada. Marine and Petroleum Geology, v. 29, p. 175–191.

Patruno, S., Hampson, G. J., & Jackson, C. A. (2015). Quantitative characterisation of deltaic and subaqueous clinoforms. Earth-Science Reviews, v. 142, p. 79–119. https://doi.org/10.1016/j.earscirev.2015.01.004

Pe-Piper, G. (2016). Reservoir quality and sediment delivery: Mesozoic Scotian Basin. Unpublished report to OERA.

Pe-Piper, G., & Piper, D. J. W. (2010). Volcanic ash in the lower Cretaceous Chaswood Formation of Nova Scotia: Source and implications. Canadian Journal of Earth Sciences, v. 47, p. 1427–1443.

Pe-Piper, G., & Piper, D. J. W. (2012). The impact of early Cretaceous deformation on deposition in the passive-margin Scotian Basin, offshore Eastern Canada. In C. Busby (Ed.), Tectonics of sedimentary basins: recent advances, Chapter 13 (pp. 270–287). Chichester, West Sussex, UK: Blackwell-Wiley.

Pe-Piper, G., & Yang, X. (2014). Albitisation of detrital feldspars in the Scotian Basin: implications for the thermal evolution of the basin; Geological Survey of Canada, Open File 7117, 496 pp. https://doi:10.4095/293609

Pe-Piper, G., Triantafyllidis, S., & Piper, D. J. W. (2008). Geochemical identification of clastic sediment provenance from known sources of similar geology: The Cretaceous

Scotian Basin, Canada. Journal of Sedimentary Research, v. 78, p. 595–607. https://doi.org/10.2110/jsr.2008.067

Pe-Piper, G., Piper, D. J. W., & Triantafyllidis, S. (2014). Detrital monazite geochronology, Upper Jurassic-Lower Cretaceous of the Scotian Basin: Significance for tracking first-cycle sources. Geological Society, London, Special Publications, v. 386, p. 293–311. https://doi.org/10.1144/SP386.13

Pe-Piper, G., Piper, D. J. W., Zhang, Y., & Chavez, I. (2015). Diagenetic barite and sphalerite in middle Mesozoic sandstones, Scotian Basin, as tracers for basin hydrology. AAPG Bulletin, v. 99, p. 1281–1313. https://doi.org/10.1306/02171514097

Pe-Piper, G., Sangster, C., & Zhang, Y. (2017). Diagenetic F-rich ferroan calcite and zircon in the offshore Scotian Basin, eastern Canada: Significance for understanding thermal evolution of the basin. American Mineralogist: Journal of Earth and Planetary Materials, v. 102, p. 1542–55.

Perrier, R., & Quiblier, J. (1974). Thickness changes in sedimentary layers during compaction history; methods for quantitative evaluation. AAPG Bulletin, v. 58, p. 507–520.

Petro-Canada Exploration inc. (1982). Well history report Banquereau C-21.

Piper, D. J. W., Pe-Piper, G., & Ingram, S. C. (2004). Early Cretaceous sediment failure in the southwestern Sable Subbasin, offshore Nova Scotia. AAPG Bulletin, v. 88, p. 991–1006. https://doi.org/10.1306/01290403120

Piper, D. J. W., Noftall, R., & Pe-Piper, G. (2010). Allochthonous prodeltaic sediment facies in the Lower Cretaceous at the Tantallon M-41 well: Implications for the deep-water Scotian Basin. AAPG bulletin, v. 94, p. 87–104.

Piper, D. J. W., Pe-Piper, G., Tubrett, M., Triantafyllidis, S., & Strathdee, G. (2012). Detrital zircon geochronology and polycyclic sediment sources, Upper Jurassic-Lower Cretaceous of the Scotian Basin, southeastern Canada. Canadian Journal of Earth Sciences, v. 49, p. 1540–1557.

Prather, B. E. (2000). Calibration and visualization of depositional process models for above-grade slopes: A case study from the Gulf of Mexico. Marine and Petroleum Geology, v. 17, p. 619–638. https://doi.org/10.1016/S0264-8172(00)00015-5

Prather, B.E., O'Byrne, C., Pirmez, C., & Sylvester, Z. (2017). Sediment partitioning, continental slopes and base-of-slope systems. Basin Research, v. 29, p.394–416.

Purdue Research Foundation (2016). MultiSpec image data analysis system. Retrieved from https://engineering.purdue.edu/~biehl/MultiSpec/ accessed 7/13/2019.

Rabineau, M., Berné, S., Aslanian, D., Olivet, J. L., Joseph, P., Guillocheau, F., Bourillet, J. F., Ledrezen, E., & Granjeon, D. (2005). Sedimentary sequences in the Gulf of Lion: a record of 100,000 years climatic cycles. Marine and Petroleum Geology, v. 22, p. 775–804.

Reynolds, P. H., Pe-Piper, G., Piper, D. J. W., & Grist, A. M. (2009). Single grain detrital-muscovite ages from Lower Cretaceous sandstones, Scotian Basin, and their implications for provenance. Bulletin of Canadian Petroleum Geology, v. 57, p. 63–80.

Reynolds, P. H., Pe-Piper, G., & Piper, D. J. W. (2012). Detrital muscovite geochronology and the Cretaceous tectonics of the inner Scotian Shelf, southeastern Canada. Canadian Journal of Earth Sciences, v. 49, p. 1558–1566.

Robertson Research International ltd. (2004). Nova Scotian Shelf: Biostratigraphic and Sequence Stratigraphic Correlation of the Early Cretaceous Strata in Seven Wells. Robertson Research International Limited Report Number CNSOPB-6620/Ib. (CNSOPB Sample Report No. SR(E) 2004-1).

Rosenfield, J., & Pindall, J. (2003). Early Paleogene isolation of the Gulf of Mexico from the World's Ocean? Implications for hydrocarbon exploration and eustacy. In C. Batolini (Ed.), The circum-Gulf of Mexico and the Caribbean: Hydrocarbon habitats, basin formation, and plate tectonics: American Association of Petroleum Geologists Memoir 79 (pp. 89–103). Tulsa, Oklahoma: United States of America.

Ruffell, A. H., & Batten, D. J. (1990). The Barremian-Aptian arid phase in western Europe. Palaeogeography, Palaeoclimatology, Palaeoecology, v. 80, p. 197–212.

Ruffell, A., & Worden, R. (2000). Paleoclimate analysis using spectral gamma-ray data from the Aptian (Cretaceous) of southern England and southern France. Paleogeography, Paleoclimatology, Paleoecology, v. 155, p. 265–283.

Saigal, G. C., Morad, S., Bjorlykke, K., Egeberg, P. K., & Aagaard, P. (1988). Diagenetic albitization of detrital K-feldspar in Jurassic, Lower Cretaceous, and Tertiary clastic reservoir rocks from offshore Norway; I, Textures and origin. Journal of Sedimentary Research, v. 58, p. 1003–1013.

Sangster, C. (2016). Provenance and Diagenesis of the Lower Cretaceous to Middle Jurassic Sandstones in the Slope Well Newburn H-23, Scotian Slope. B.Sc. Hon. Thesis, Saint Mary's University, Halifax, Nova Scotia, 472 pp.

Sangster, C., Piper, D. J. W., Hawie, N., Pe-Piper, G., & Saint-Ange, F. (2019). Forward stratigraphic modelling of sediment pathways and depocentres in salt-influenced passive-margin basins: Lower Cretaceous, central Scotian Basin. Basin Research, v. 31, p. 728–753. https://doi.org/10.1111/bre.12342

Schmoker, J. W., & Gautier, D. L. (1988). Sandstone porosity as a function of thermal maturity. Geology, v. 16, p. 1007–1010.

Schmoker, J. W., & Schenk, C. J. (1994). Regional porosity trends of the Upper Jurassic Norphlet Formation in southwestern Alabama and vicinity, with comparisons to formations of other basins. AAPG Bulletin, v. 78, p. 166–180.

Shimeld, J. (2004). A comparison of salt tectonic subprovinces beneath the Scotian Slope and Laurentian Fan. In P. J. Post et al. (Eds.), Salt sediment interactions and hydrocarbon prospectivity: Concepts, applications, and case studies for the 21st century: 24th Annual Gulf Coast Section SEPM Foundation Bob F. Perkins Research Conference Proceedings (pp. 502–532). Houston, TX: United States of America.

Smith, B., & Kendell, K. (2011). Sediment transportation, Sable delta to deepwater, 2011 AAPG ICE: Nova Scotia Play Fairway Analysis Seminar Technical Presentations, AAPG Seminar – Brent Smith [online]. Retrieved from https://energy.novascotia.ca/oil-and-gas/offshore/play-fairway-analysis/data-and-presentations

Sømme, T. O., Martinsen, O. J., & Thurmond, J. B. (2009a). Reconstructing morphological and depositional characteristics in subsurface sedimentary systems: An example from the Maastrichtian-Danian Ormen Lange system, More Basin, Norwegian Sea. AAPG Bulletin, v. 93, p. 1347–1377.

Sømme, T. O., Helland-Hansen, W., Martinsen, O. J., & Thurmond, J. B. (2009b). Relationships between morphological and sedimentological parameters in source-to-sink systems: A basis for predicting semi-quantitative characteristics in subsurface systems. Basin Research, v. 21, p. 361–387.

Sweet, M. L., & Blum, M. D. (2011). Paleocene-Eocene Wilcox submarine canyons and thick deepwater sands of the Gulf of Mexico: Very large systems in a greenhouse world, not a Messinian-like crisis. Transactions-Gulf Coast Association of Geological Societies, v. 61, p. 443–450.

Tappe, S., Foley, S. F., Stracke, A., Romer, R. L., Kjarsgaard, B. A., Heaman, L. M., & Joyce, N. (2007). Craton reactivation on the Labrador Sea margins: 40Ar/39Ar age and Sr–Nd–Hf–Pb isotope constraints from alkaline and carbonatite intrusives. Earth and Planetary Science Letters, v. 256, p. 433–454. https://doi.org/10.1016/j.epsl.2007.01.036

Taylor, T. R., (1996). Association of allochthonous waters and reservoir enhancement in deeply buried Miocene sandstones: Picaroon field, Corsair trend, offshore Texas, in L. J. Crossey, R. Loucks, and M. W. Totten, eds., Siliciclastic diagenesis and fluid flow: Concepts and applications: SEPM Special Publication 55, p. 37–48.

Taylor, T. R., Giles, M. R., Hathon, L. A., Diggs, T. N., Braunsdorf, N. R., Birbiglia, G. V, Kittridge, M. G., Macaulay, C. I., & Espejo, I. S. (2010). Sandstone diagenesis and reservoir quality prediction: Models, myths, and reality. AAPG Bulletin, v. 94, p. 1093–1132.

Tovey, N. K., & Krinsley, D. H. (1992). Mapping of the orientation of fine-grained minerals in soils and sediments. Bulletin of the International Association of Engineering Geology-Bulletin de l'Association Internationale de Géologie de l'Ingénieur, v. 46, p. 93–101.

Tsikouras, B., Pe-Piper, G., Piper, D. J. W., & Schaffer, M. (2011). Varietal heavy mineral analysis of sediment provenance, Lower Cretaceous Scotian Basin, eastern Canada. Sedimentary Geology, v. 237, p. 150–165. https://doi.org/10.1016/j.sedgeo.2011.02.011

Tucker, G. E., & Slingerland, R. L. (1994). Erosional dynamics, flexural isostasy, and long-lived escarpments: A numerical modelling study. Journal of Geophysical Research: Solid Earth, v. 99, p. 12229–12243.

Twenhofel, W. H., & MacClintock, P. (1940). Surface of Newfoundland. Bulletin of the Geological Society of America, v. 51, p. 1665–1728. https://doi.org/10.1130/GSAB-51-1665

Tyrrell, S., Pe-Piper, G., Piper, D.J.W. (2014). First cycle supply to the Cretaceous Scotian Basin resolved using Pb-isotopes in detrital Kfeldspar grains. 4th Atlantic Conjugate Margins Conference Abstracts Volume, St. John's Newfoundland Canada August 20–22.

Van der Meer, D. G., van Saparoea, A. V., Van Hinsbergen, D. J., Van de Weg, R. M., Godderis, Y., Le Hir, G., & Donnadieu, Y. (2017). Reconstructing first-order changes in sea level during the Phanerozoic and Neoproterozoic using strontium isotopes. Gondwana Research, v. 44, p. 22–34.

Wade, J., & MacLean, B. (1990). The geology of the southeastern margin of Canada. In M. J. Keen and G. L. Williams (Eds.), Geology of the continental margin of eastern Canada. Geological Survey of Canada, Geology of Canada (vol. 2, pp. 167–238). Ottawa, ON: Geological Survey of Canada.

Walker, T. R. (1984). SEPM presidential address; Diagenetic albitization of potassium feldspar in arkosic sandstones. Journal of Sedimentary Research, v. 54, p. 3–16.

Weston, J. F., MacRae, R. A., Ascoli, P., Cooper, M. K. E., Fensome, R. A., Shaw, D., & Williams, G. L. (2012). A revised biostratigraphic and well-log sequence-stratigraphic framework for the Scotian Margin, offshore eastern Canada. Canadian Journal of Earth Sciences, v. 49, p. 1417–1462.

Whitney, D. L. & Evans, B. W. (2010). Abbreviations for names of rock-forming minerals. American mineralogist., v. 95, p. 185–187.

Wilkinson, M., Darby, D., Haszeldine, R. S., & Couples, G. D. (1997). Secondary porosity generation during deep burial associated with overpressure leak-off: Fulmar Formation, United Kingdom Central Graben. AAPG bulletin, v. 81, p. 803–813.

Wilkinson, M., Milliken, K. L., & Haszeldine, R. S. (2001). Systematic destruction of K-feldspar in deeply buried rift and passive margin sandstones. Journal of the Geological Society, v. 158, p. 675–83.

Williams, H., & Grant, A. (1998). Tectonic assemblages, Atlantic region, Canada. Geological Survey of Canada Open-File, 3657, 1 pp.

Wolman, M. G., & Gerson, R. (1978). Relative scales of time and effectiveness of climate in watershed geomorphology. Earth Surface Processes and Landforms, v. 3, p. 189–208. https://doi.org/10.1002/esp.3290030207

Yuan, G., Cao, Y., Gluyas, J., Li, X., Xi, K., Wang, Y., Jia, Z., Sun, P., & Oxtoby, N. H. (2015). Feldspar dissolution, authigenic clays, and quartz cements in open and closed sandstone geochemical systems during diagenesis: Typical examples from two sags in Bohai Bay Basin, East China. AAPG Bulletin, v. 99, p. 2121–2154.

Zhang, Y., Pe-Piper, G., & Piper, D. J. W. (2014). Sediment geochemistry as a provenance indicator: Unravelling the cryptic signatures of polycyclic sources, climate change, tectonism and volcanism. Sedimentology, v. 61, p. 383–410. https://doi.org/10.1111/sed.12066

Zhang, Y., Pe-Piper, G., & Piper, D. J. W. (2015). How sandstone porosity and permeability vary with diagenetic minerals in the Scotian Basin, offshore eastern Canada: implications for reservoir quality. Marine and Petroleum Geology, v.63 p. 28–45.

Zhu, X. M., Zhong, D. K., Zhang, Q. & Zhang, L. (2004). Sandstone diagenesis and porosity evolution of Paleogene in Huimin depression: Petroleum Science, v. 3, p. 23–29.

Zhu, S., Zhu, X., Wang, X., & Liu, Z. (2012). Zeolite diagenesis and its control on petroleum reservoir quality of Permian in northwestern margin of Junggar Basin, China: Science China Earth Sciences, v. 55, p. 386–396. https://doi:10.1007/s11430-011-4314-y